https://doi.org/10.15388/vu.thesis.657
https://orcid.org/0000-0002-9674-9918

VILNIUS UNIVERSITY
CENTER FOR PHYSICAL SCIENCES AND TECHNOLOGY

Davit Tediashvili

Understanding of Electrochemical Interfaces in Aqueous Sodium-Ion Batteries: From Degradation Mechanisms to Mitigation Strategies

DOCTORAL DISSERTATION

Natural Sciences,
Chemistry (N 003)

VILNIUS 2024

The dissertation was prepared between 2019 and 2023 at the Institute of Chemistry, Faculty of Chemistry and Geosciences, Vilnius University.

Academic supervisor:

Doc. Dr. Linas Vilčiauskas (Vilnius University, Natural Sciences, Chemistry, N 003)

Academic consultant:

Dr. Jurga Juodkazytė (Center for Physical Sciences and Technology, Natural Sciences, Chemistry, N 003)

This doctoral dissertation will be defended in a public/closed meeting of the dissertation defense panel:

Chairman:

Prof. Dr. Simas Šakirzanovas (Vilnius University, Natural Sciences, Chemistry, N 003)

Members:

Prof. Dr. Henrikas Cesiulis (Vilnius University, Natural Sciences, Chemistry, N 003)

Dr. Loreta Tamašauskaitė-Tamašiūnaitė (Center for Physical Sciences and Technology, Natural Sciences, Chemistry, N 003)

Prof. Habil. Dr. Eimutis Juzeliūnas (Center for Physical Sciences and Technology, Natural Sciences, Chemistry, N 003)

Dr. Jędrzej Piątek (Krakow Institute of Technology, Natural Sciences, Chemistry, N 003)

The dissertation shall be defended at a public meeting of the dissertation defense panel at 14:00 on September 20th, 2024 in Room E302 of the Center for Physical Sciences and Technology.

Address: Saulėtekio al. 3, Vilnius, Lithuania
Tel. +370-5-219-3105; e-mail: info@chgf.vu.lt

The text of this dissertation can be accessed at the libraries of Center for Physical Sciences and Technology and Vilnius University, as well as on the website of Vilnius University:

www.vu.lt/lt/naujienos/ivykiu-kalendorius

https://doi.org/10.15388/vu.thesis.657
https://orcid.org/0000-0002-9674-9918

VILNIAUS UNIVERSITETAS
FIZINIŲ IR TECHNOLOGIJOS MOKSLŲ CENTRAS

Davit Tediashvili

Vandeninių natrio jonų baterijų elektrocheminių sandūrų tyrimai: nuo degradacijos mechanizmų iki prevencijos metodų

DAKTARO DISERTACIJA

Gamtos mokslai,
Chemija (N 003)

VILNIUS 2024

Disertacija rengta 2019–2023 metais Vilniaus universiteto Chemijos ir geomokslų fakulteto Chemijos institute.

Mokslinis vadovas:
doc. dr. Linas Vilčiauskas (Vilniaus universitetas, gamtos mokslai, chemija, N 003)
Mokslininė konsultantė:
dr. Jurga Juodkazytė (Fizinių ir technologijos mokslų centras, gamtos mokslai, chemija, N 003)

Gynimo taryba:
Pirmininkas:
prof. dr. Simas Šakirzanovas (Vilniaus universitetas, gamtos mokslai, chemija, N 003).
Nariai:
prof. dr. Henrikas Cesiulis (Vilniaus universitetas, gamtos mokslai, chemija, N 003)
dr. Loreta Tamašauskaitė-Tamašiūnaitė (Fizinių ir technologijos mokslų centras, Natural Sciences, Chemistry, N 003)
prof. habil. dr. Eimutis Juzeliūnas (Fizinių ir technologijos mokslų centras, gamtos mokslai, chemija, N 003)
dr. Jędrzej Piątek (Krokuvos technologijų institutas, gamtos mokslai, chemija, N 003)

Disertacija ginama viešame Gynimo tarybos posėdyje 2024 m. rugsėjo mėn. 20 d. 14:00 val. Valstybinio mokslinių tyrimų instituto Fizinių ir technologijos mokslų centro E302 auditorijoje.
Adresas: Saulėtekio al. 3, Vilnius, Lietuva.
Tel. +370-5-219-3105; e-paštas: info@chgf.vu.lt.

Disertaciją galima peržiūrėti Fizinių ir technologijos mokslų centrao ir Vilniaus universiteto bibliotekose ir VU interneto svetainėje adresu:
https://www.vu.lt/naujienos/ivykiu-kalendorius

TABLE OF CONTENTS

LIST OF ABBREVIATIONS

a.u.	Arbitrary unit
AFM	Atomic Force Microscopy
ALD	Atomic Layer Deposition
ALIB	Aqueous Li-ion Battery
CA	Citric Acid
CE	Coulombic Efficiency
CV	Cyclic Voltammetry
EDX	Energy-dispersive X-Ray Spectroscopy
EIS	Electrochemical Impedance Spectroscopy
EQCM	Electrochemical Quartz-Crystal Microbalance
GCD	Galvanostatic Charge/Discharge
HER	Hydrogen Evolution Reaction
LIB	Lithium-ion Battery
LNMO	$LiNi_{0.5}Mn_{1.5}O_4$
LTO	$Li_4Ti_5O_{12}$
N3TP	$Na_3Ti_2(PO_4)_3$
NASICON	Natrium SuperIonic Conductor
NMC	$LiNi_xMn_yCo_zO_2$
NMP	N-Methyl-2-Pyrrolidone
NMPC	$Na_3MnPO_4CO_3$
NMPP	$Na_4Mn_3(PO_4)_2P_2O_7$
NMTP	$Na_3MnTi(PO_4)_3$
NTP	$NaTi_2(PO_4)_3$
NVP	$Na_3V_2(PO_4)_3$
NVPF	$Na_3V_2(PO_4)_2F_3$
ORR	Oxygen Reduction Reaction
PDA	PolyDopAmine
PEDOT	Poly(3,4-EthyleneDiOxyThiophene)

PSS	PolyStyrene Sulfonate
PVC	PolyVinyl Chloride
PVDF	PolyViniliDene Flouride
RDE	Rotating Disc Electrode
RRDE	Rotating Ring-Disc Electrode
SECM	Scanning ElectroChemical Microscopy
SEI	Solid-Electrolyte Interphase
SEM	Scanning Electron Microscopy
SIB	Sodium-ion Battery
TGA	ThermoGravimetric Analysis
XPS	X-ray Photoelectron Spectroscopy
XRD	X-ray Diffraction

1. INTRODUCTION

As global energy consumption continues to rise, the need for new renewable sources and decarbonization of the energy mix becomes increasingly apparent. The recent growth of wind and solar electricity generation presents a promising option [1–3]. However, the efficient storage of this energy to tackle intermittency remains a key challenge [4]. Rechargeable lithium-ion batteries utilizing organic solvent-based electrolytes have become the preferred storage choice for portable electronic devices due to their attractive energy and power densities [5,6]. But when it comes to their applications for large-scale storage, concerns arise over the scarcity and uneven distribution of natural resources like lithium, cobalt, nickel, natural graphite. Safety due to the flammability of organic solvents is another important issue [7–11]. Both of these concerns are the main drivers for the exploration of alternative or *post* lithium-ion battery technologies [12]. Among them, sodium-ion batteries, and especially their variant using aqueous electrolytes have gained significant attention [13]. This is mainly due to the availability and cost of the electrode materials as well as improved safety and environmental friendliness. Nevertheless, the introduction of alternative charge carrier and aqueous electrolyte systems causes other challenges [14–16]. These include the need for alternative electrode materials since traditional choices such as transition metal oxides and graphite fall short for sodium-ion batteries [17–19]. Additionally, aqueous acid-base chemistry and water solvating properties add to the electrode/electrolyte stability challenges. Among the different classes of materials suitable for aqueous sodium-ion batteries, framework phosphates such as NASICON-structured materials have emerged as one of the promising alternatives [20–23]. This is mainly due to their high structural diversity, stability, and low cost. However, a number of issues related to their compatibility with aqueous electrolyte systems still remain and need to be understood to fully unlock the potential of these materials [24,25].

The **main goal** of this work is to investigate the electrochemical interfaces relevant to aqueous sodium-ion batteries in order to understand their degradation processes and to develop relevant mitigation strategies to prevent them.

The **specific objectives** of this work are as follows:

1. Investigate and understand the details of electrochemical degradation processes of phosphate framework materials as aqueous Na-ion battery electrodes, utilizing various structural, morphological, spectroscopic, and electrochemical techniques. The materials under investigation in this work are NASICON-structured **$NaTi_2(PO_4)_3$** as a negative electrode material, and NASICON or structurally related mixed-phosphate manganese- **$Na_3MnTi(PO_4)_3$**, **$Na_3MnPO_4CO_3$**, and **$Na_4Mn_3(PO_4)_2P_2O_7$** and vanadium-based **$Na_3V_2(PO_4)_3$** and **$Na_3V_2(PO_4)_2F_3$** as positive electrode materials.
2. Explore and apply **$NaTi_2(PO_4)_3$** degradation mitigation techniques in aqueous electrolytes based on conformal electrode protective coatings using atomic layer deposition of **Al_2O_3, TiO_2** and **HfO_2** metal oxides and conductive **PEDOT:PSS** and **Nafion** polymers.

The **novelty** of this work stems from the first attempt to provide a detailed mechanistic understanding of various degradation processes taking place in NASICON and several structurally related phosphate framework electrode materials using a combination of *ex situ* and *in situ* experimental techniques. The new results and insights are summarized below as statements for the defense.

The **statements** for the defense are as follows:

1. Chemical oxygen reduction reaction catalyzed by $Ti^{(III)}$ which is generated during charging of **$NaTi_2(PO_4)_3$** is identified as the main parasitic process leading to self-discharge, and local alkalization of the electrolyte. Local pH increase, and the duration the material spends in this medium are identified as the main reasons behind the degradation and capacity loss of **$NaTi_2(PO_4)_3$** as a negative electrode in aqueous Na-ion batteries.

2. Electrochemically-induced manganese dissolution and the stability of dissolved $Mn^{(II)}$(aq.) in near-neutral aqueous medium are identified as the main causes of the capacity loss of **$Na_3MnTi(PO_4)_3$, $Na_3MnPO_4CO_3$,** and **$Na_4Mn_3(PO_4)_2P_2O_7$** in low concentration aqueous electrolytes. *In situ* degradation studies show that Jahn-Teller distortion caused by the

formation of $Mn^{(III)}$ in the charged state of these frameworks is the most likely reason leading to their structural destabilization and subsequent dissolution of $Mn^{(II)}$. However, most of the $Mn^{(II)}$ dissolution only takes place on the particle surface making the bulk of material intact but electrochemically inaccessible.

3. Chemical vanadium dissolution and stability of $V^{(V)}$ in low concentration near-neutral aqueous electrolytes is identified as the main degradation causes in NASICON-structured **$Na_3V_2(PO_4)_3$**. This process is only accelerated by the electrochemical charge-discharge cycling. The introduction of fluoride ions into the structure of **$Na_3V_2(PO_4)_2F_3$** is found to significantly increase the framework stability towards chemical dissolution. However, the electrochemically-induced degradation is still prevalent with almost all vanadium being leached out during extended charge-discharge cycling.

4. The application of protective ceramic or polymeric coatings is shown to be an effective and scalable strategy for protecting the degradation of **$NaTi_2(PO_4)_3$** in low-concentration aqueous electrolytes during electrochemical operation. The widely applied atomically deposited **Al_2O_3** and **TiO_2** are shown to be either insuffuficiently stable or a source of parasitic reaction themselves. Therefore not able to provide sufficient degradation protection. Only **HfO_2** layers are shown to be sufficiently chemically stable and inert. An *in situ* formed **poly(3,4-ethylenedioxythiophene)** polymeric coating is shown to provide alternative sites for electrochemical oxygen reduction reaction. However, it is insufficiently robust to protect the material from degradation in a locally alkaline environment. On the other hand, conformal **Nafion** electrode coatings are found to provide relatively good protection. This is most likely due to its better mechanical robustness and acidic nature which acts as a local buffer.

1.1 Background and Motivation.

The energy demand, closely linked to economic growth, has been exponentially increasing over time [26]. Fossil-based sources currently dominate the primary energy landscape. The main advantage of these sources is their high energy density and relatively low cost. However, due to their finiteness and significant contribution to greenhouse gas emissions, there is a growing social and political pressure to replace them. Renewable energy sources, such as wind and solar power, have emerged as potential alternatives [1–3]. In the past decade, the cost of solar and wind energy generation technologies has substantially decreased making them increasingly more competitive with traditional generation. However, the main issue with these sources is their intermittency. In order to address their intermittent nature and fully harness their potential, efficient energy storage systems are essential. Among various technologies, electrochemical devices, particularly batteries, have emerged as one of the leading alternatives [4]. This is primarily due to their wide energy/power range, scalability from micro to large scale systems, and constantly decreasing cost due to the emergence of economies of scale.

The operating principle of an electrochemical energy conversion system encompasses three main steps: charge separation, transport, and recombination [27]. This is shared among various types of systems, although specific details may vary depending on the type of device. The purpose of a battery cell is to interconvert electrical and chemical energies through redox reactions. This process can be either irreversible/unidirectional (in primary or non-rechargeable batteries) or reversible/bidirectional (in secondary or rechargeable batteries) [27]. In this work, the man focus is placed on materials and processes relevant for secondary batteries. Currently, secondary batteries with different electrode and electrolyte chemistries are utilized as energy storage devices depending on the application. These include lead-acid [28], nickel-iron [29], nickel-metal hydride [30], or lithium-ion batteries [31], etc.. Each type possesses distinct advantages and limitations.

Originally, rechargeable batteries were developed almost two centuries ago with the invention of a lead-acid battery [28]. Energy storage systems based on batteries are characterized by high efficiency, wide energy/power range, easy scalability and maintenance, and constantly improving costs due to manufacturing scale-up. The key performance characteristics of a secondary battery cell include the amount of energy stored per unit weight (specific energy) or volume (energy density), the rate at which this energy can be extracted per unit weight (specific power), operating temperature range, calendar, and cycle lifetime, self-discharge rate, etc. In simpler terms, capacity measures the quantity of charge stored in the electrode, while the equilibrium voltage can be understood as the energy of the charge separation/recombination during the charge/discharge.

Typically, a battery cell comprises three key structural components: a positive electrode (positrode), a negative electrode (negatrode), and an electrolyte that selectively conducts ions and blocks electrons. These components might have different chemical nature, composition, aggregate state. A typical battery electrode of a modern commercial cell is a thick composite film consisting of three main components. The primary component is the active material, responsible for the redox reactions that take place during operation, and typically makes up most of the electrode (e.g. 95 wt%). Additionally, an electronically conductive material or filler such as some carbonaceous phase is incorporated to enhance the electronic conductivity. Finally, a polymeric binder is included to ensure the mechanical integrity of the composite mass and often its adhesion to the metallic current collector [32]. The latter serves as the pathway for electrons to reach the external circuit.

During a battery discharge process, the active material in the negative electrode is oxidized, therefore electrons will travel through the external circuit toward the positive electrode, where the active material reduction will take place. For example, the two reactions in lead-acid batteries are:

$$\mathrm{Pb} + \mathrm{HSO_4^-} \rightarrow \mathrm{PbSO_4} + \mathrm{H^+} + 2\mathrm{e^-} \qquad \mathrm{E^0} = -0.36\ \mathrm{V} \qquad (1)$$

$$\mathrm{PbO_2} + \mathrm{HSO_4^-} + 3\mathrm{H^+} + 2\mathrm{e^-} \rightarrow \mathrm{PbSO_4} + 2\mathrm{H_2O} \qquad \mathrm{E^0} = \ \ 1.68\ \mathrm{V} \qquad (2)$$

One can easily notice that an electrolyte also actively participates in the redox reactions, so the true voltage depends on the concentration of the sulfuric acid. The operating voltage in commercial devices is typically ca. 2 V [33]. Although it seemingly exceeds the standard thermodynamic stability window of water (1.23 V), the Nernstian and kinetic factors significantly expand it. These factors are a recurring theme in aqueous batteries and will be discussed in more detail later.

Li-ion is one of the smallest and lightest charge carriers (3861 mAh g^{-1}). Therefore, it might be reversibly inserted/extracted in/from multiple electrode materials with minimal structural changes and at fast rates. The original Li-ion battery technology was mostly developed in the 1980s and still relies on the use of either transition metal oxides (e.g., Li_xMO_2, M = Co, Ni, Mn) or phosphates (e.g., $LiFePO_4$) as positive electrode materials [34]. The simultaneous development of low-potential carbon-based materials led to the commercialization of the first $Li_xC_6/Li_{1-x}CoO_2$ devices in 1991 by Sony [35]. The electrolytes typically comprise salts such as $LiPF_6$ dissolved in organic solvents such as a mixture of organic aliphatic and cyclic carbonates [36,37]. The schematic representation of a Li-ion battery cell can be found in Figure.

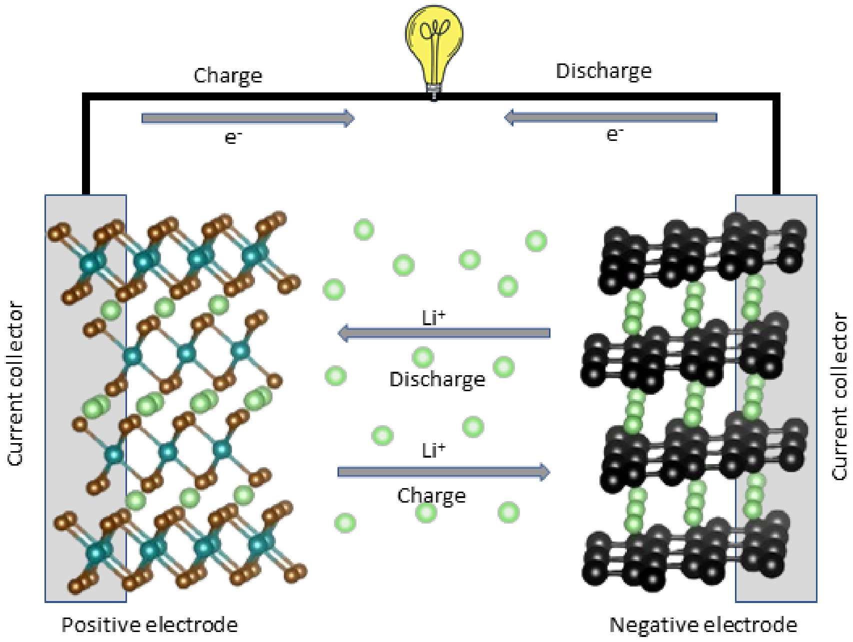

Figure 1. Schematic representation of Li-ion battery cell.

During the battery operation, in the charging process, the metal redox center in the positive electrode undergoes oxidation, and lithium ions are extracted from the lattice, migrating towards the graphite, where they are recombined with electrons [7,32,38]. During the discharge, the whole process is reversed. As a result, the active materials in the electrodes, in principle, remain intact while Li-ions are shuttled back and forth between the electrodes, earning the name of a *rocking-chair* concept. The two redox reactions in electrodes are:

$$\mathrm{Li_{1-x}CoO_2 + xLi^+ + xe^- \rightarrow LiCoO_2} \qquad \sim 3.9\mathrm{V\ vs\ Li/Li^+} \qquad (3)$$

$$\mathrm{Li_xC_6 \rightarrow xLi^+ + xe^- + C_6} \qquad \sim 0.1\mathrm{V\ vs\ Li/Li^+} \qquad (4)$$

1.2. Aqueous ion-insertion batteries

When it comes to large-scale stationary energy storage, LIBs face a significant challenge because of their safety, reliability, and the cost of materials. The usage of organic solvents in LIBs contributes to increased production costs and raises safety concerns [7–11,39]. All of these features have spurred a growing interest in aqueous systems as a safe and sustainable alternative. Aqueous systems offer several advantages such as enhanced safety by avoiding the use of potentially flammable organic electrolytes. They also have higher ionic conductivity (typically 2-3 orders of magnitude higher) than their organic counterparts [40]. Higher conductivity typically enables the use of thicker electrodes, thereby increasing the cell energy density at the same power [14,41,42]. The salts used in aqueous electrolyte systems are also more affordable, contributing to reduced manufacturing costs. Additionally, aqueous batteries are considered environmentally friendlier and safer to handle [43].

Traditionally, the use of aqueous electrolytes in energy storage systems has been limited by their electrochemical stability window [40,44,45]. The narrow electrochemical stability window in turn severely limits the available energy density of such systems. On top of the narrow potential window, strong solvation properties of the water also pose challenges for inorganic materials, when employed as electrodes in aqueous energy storage systems. However, for stationary storage applications, safety, cost, and sustainability are more important and can be traded off for the reduced energy density. As a result, there is a growing interest in developing and utilizing aqueous-based electrochemical energy systems [14,46].

One of the first „rocking chair“ aqueous rechargeable Li-ion batteries (ALIB) was introduced by Dahn’s group back in 1995 [47]. The cell employed 5 M $LiNO_3$ aqueous electrolyte, and VO_2 and $LiMn_2O_4$ as negative and positive electrodes, respectively. The cell achieved 1.5 V operating voltage and ~75 Wh kg^{-1} at cell level. Despite successfully replicating the mechanism of Li-ion intercalation in aqueous media, the materials suffered severe degradation through dissolution, resulting in rapid capacity fade. Conventional transition metal oxide electrode materials used in organic electrolyte-based batteries may dissolve and leach metals in aqueous environments [14–16]. This calls for the development of not only more stable electrode materials but also novel electrolytes and degradation mitigation strategies that can withstand these conditions.

1.3. Active electrode materials for aqueous ion-insertion batteries

One of the concerns related to the rising demand for LIBs is the volatile price of limited and unevenly distributed lithium resources [48,49]. Therefore, there is an urgent need to explore alternative battery chemistries and materials to ensure sustainable and cost-effective energy storage solutions. Alternative charge-carrying ions, such as potassium and sodium present viable more abundant alternatives [12,13,50]. In contrast to lithium, sodium is ~1000 more abundant and geographically evenly distributed in the Earth's crust and oceans [51]. This, together with similar chemical properties, makes sodium a promising alternative to be employed as a charge-carrying ion in ion insertion batteries [52].

The operating potentials of aqueous Na-ion battery (ASIB) electrodes need to be within the stability of the aqueous electrolyte and they need to withstand the aggressive nature of the water as a solvent. Although layered- and spinel-type transition metal oxides proved to be suitable cathode materials for reversible, high-potential Li-ion intercalation, the electrochemical performance of Na-ion analogs seems to be much different. One of the reasons is the larger ionic size of Na-ion (1.02 vs 0.76 Å) [17]. In addition, even if Na_xMO_2 (M – transition metal) oxides were sufficiently stable, they still suffer from undesirable voltage profiles and overall lower average operating potential than Li-ion counterparts [18,19,53]. Polyanion compounds offer another alternative [54], and advantages such as higher operating potential, non-sloping potential plateau, and better electrochemical stability. These advantages led to the emergence of $LiFePO_4$-based batteries [55,56]. The increase in operating potential in polyanion compounds can be explained by the inductive effect, according to which, the reduction of covalency in M-O bonds can lead to higher intercalation potential. This can be achieved by introducing an electronegative X atom in the M-O-X chain [54,57,58].

NASICON-structured phosphate materials are of great interest [20–22,25,59,60]. With general formula $Na_xM_2(PO_4)_3$ (x = 1 - 4, M – transition metal), they offer high structural diversity and stability, a wide selection of electrode potentials by choosing different transition metals, and an open framework with fast ionic transport [46,54,61–63]. However, like most phosphate materials, they suffer from low intrinsic electronic conductivity. This issue can be solved by optimizing the synthesis conditions to achieve smaller particle sizes and by coating these particles with carbonaceous phase or adding additional conducting carbon filler into the composite electrode [23]. NASICON-structured electrode materials owe their electrochemical activity to the transition metal redox accompanied by the (de)insertion of sodium ions. Typically, the two-phase sodiation mechanism provides a very stable and flat potential plateau, making NASICONs excellent electrode materials [21,23].

For example, NASICON-structured $LiTi_2(PO_4)_3$ operates at approximately -0.5 V vs SHE [64,65], rendering it a compatible choice for aqueous electrolytes. The sodium variant, $NaTi_2(PO_4)_3$ (NTP) is also one of the most attractive options for aqueous Na-ion batteries negative electrodes. The material operates by reversibly (de)inserting two Na-ions at ca. 2.1 V vs Na^+/Na (ca. -0.6 V vs SHE) and delivers a theoretical capacity of 133 mAh g^{-1} [20,60,66]. However, the material is prone to degradation at elevated pH, which can occur due to HER as well as oxygen reduction reactions.

Despite the relative success in identifying appropriate negative electrode materials for ASIBs, the development of suitable cathode materials remains a challenge. While cobalt and nickel-based materials have proven effective in their lithium-ion counterparts, their translation to sodium-ion systems has encountered certain limitations. For example, $NaCoPO_4$ offers a relatively high operating potential range of ca. 4.1 - 4.4 V vs Na^+/Na, however, it has shown poor ion insertion, with the capacity of only ca. 30 mAh g^{-1} [67]. Improvements have been observed for pyrophosphate-based materials, such as $Na_2CoP_2O_7$, which offer an operating potential of ca. 4 V vs Na^+/Na and delivers a capacity of 80 mAh g^{-1} [68,69].

Since the main applications of ASIBs are limited to stationary energy storage, materials employing more abundant metals are ultimately desirable when designing electrodes. Hence, transition metals with relatively large abundance in the Earth's crust, offering multiple redox states are of special interest. $LiFePO_4$ is a well-established cathode material for LIBs, which has been widely employed due to the availability of materials and relatively high capacity. Unfortunately, the Na-ion analog $NaFePO_4$ which exhibits a promisingly high capacity of ca. 150 mAh g^{-1}, cannot be obtained via chemical route [70]. NASICON-structured $Na_3Fe_2(PO_4)_3$ material presents another viable option, but its potential of 2.5 V vs. Na^+/Na, is not suitable for positive electrodes [71]. $Na_2FeP_2O_7$ offers only a slightly better voltage of ca. 3 V vs Na^+/Na [72].

Mn-based materials offer some of the highest operating potentials and could be suitable for ASIBs. They have been used as positive electrode materials for over a century, initially in primary, and later in secondary batteries [32,73,74]. Various polyanionic systems such as Prussian Blue analogs (PBA) or NASICON-structured phosphates containing manganese at the transition metal site tend to be even more robust frameworks than oxides

[75–77]. For example, $NaMnPO_4$ has been successfully synthesized, but its electrochemical performance remains unsatisfactory [78]. A promising alternative is a Ti-substituted NASICON-structured $Na_3MnTi(PO_4)_3$, which can employ both Mn^{2+}/Mn^{3+} and Mn^{3+}/Mn^{4+} redox transitions at ca. 3.6 V and ca. 4.1 V vs. Na/Na^+, respectively [79]. The substitution of transition metals with Ti is known to have a stabilizing effect due to the deemed suppression of Jahn-Teller distortions in Mn^{+3}-containing materials [80,81]. However, the understanding of the operation of Mn-based phosphate framework materials in aqueous media is still missing.

Vanadium-based materials represent another interesting group [46]. Vanadium is relatively abundant and shows multiple redox transitions with high electrode potentials. NASICON-structured $Na_3V_2(PO_4)_3$ (NVP) [82,83] or structurally related fluoride-substituted alternative $Na_3V_2(PO_4)_2F_3$ (NVPF) [84] seem to be the most promising candidates. They exhibit relatively high specific capacities (117.6 mAh g^{-1} for NVP and 128.3 mAh g^{-1} for NVPF), high operating potentials (3.4 V vs. Na^+/Na for NVP and 3.7/4.2 V vs. Na^+/Na for NVPF), structural stability, and fast and reversible Na-ion extraction/insertion. As a result, they have already found successful applications as positive electrode materials in non-aqueous Na-ion batteries and have even entered commercial use [85].

1.4. Capacity loss in aqueous ion-insertion batteries

In order to practically implement these materials in ASIBs, it is important to understand their capacity loss during operation. For most of the electrode materials, mechanically induced stress and fracturing is one of the reasons for the electrochemical degradation and capacity fade [32]. The operation of an active material involves the extraction/insertion of charge carrying ions within its structure, causing a change in volume. In scenarios featuring two-phase reactions an increase of mechanical stress at the boundary between sodiated and desodiated states is expected. The change in stress depends upon the rate at which ions (de)intercalate, meaning that a faster charge/discharge rate tends to amplify the likelihood of fractures. NASICON materials, typically show relatively minor volume changes associated with ion (de)intercalation [54,79,86] and are sometimes designated as zero-strain materials.

The most obvious difference, when moving from organic electrolytes to aqueous ones is the limited electrochemical stability window. Thermodynamically, the electrolytic stability window of water at standard conditions is 1.23 V. Beyond this, water decomposes, producing H_2 and O_2 at the negative and positive electrodes respectively. In order, to achieve the optimal energy density in ASIBs the operating potentials of electrode materials need to be as close to the edges of the electrolyte stability window as possible. Aqueous degradation can lead to (i) the generation of OH^-/H^+ ions, which can be a problem if the electrode materials are unstable in alkaline/acidic media; (ii) the build-up of internal pressure within a sealed system; (iii) the formation of bubbles, which can potentially restrict electrolyte access to the electrode surface; (iv) electrolyte starvation of the system.

The dissolution of the active material is a common problem in ion-insertion batteries. In this work, the focus is on vanadium and manganese-based materials, as their solubility in aqueous media is heavily influenced by the metal oxidation states, which change during the battery operation. It is well known that Mn-based materials are prone to degradation during the electrochemical cycling in both, aqueous and non-aqueous electrolytes leading to a pronounced capacity fade [87–89]. The most widely used explanation is based on the disproportionation of $Mn^{(III)}$ and the subsequent dissolution of $Mn^{(II)}$ [90]:

$$2\mathrm{Mn}_{\mathrm{solid}}^{(\mathrm{III})} \rightarrow \mathrm{Mn}_{\mathrm{solid}}^{(\mathrm{IV})} + \mathrm{Mn}_{\mathrm{solution}}^{(\mathrm{II})} \qquad (5)$$

This reaction is much more pronounced in aqueous media due to the stability of $Mn_{aq.}^{(II)}$ and the presence of protons which tend to catalyze charge disproportionation [91]. In addition to the initial capacity loss, $Mn^{(II)}$ (aq.) could itself be electrochemically oxidized on the surface of the electrode at high potentials [92]:

$$\mathrm{Mn}_{\mathrm{aq.}}^{(\mathrm{II})} + 2\mathrm{H_2O} \rightarrow \mathrm{MnO_2} + 4\mathrm{H}_{\mathrm{aq.}}^{+} + 2\mathrm{e}^{-} \qquad (6)$$

This process leads to the formation of electrochemically active MnO_{2-x} species, which can itself show some electrochemical activity or precipitate into solid, electrochemically inactive Mn_3O_4, leading to capacity loss. Various experimental techniques have been employed to investigate the degradation of battery materials both *in situ/operando* and through *ex situ*/*post mortem* analyses, encompassing a range of diffraction and spectroscopic methods [93,94]. In particular, the electrochemical dissolution of electrode materials has been analyzed extensively. Different studies have been carried out through sophisticated methodologies like specialized electroanalytical flow cells coupled with ICP-MS/OES, offering comprehensive insights into the intricacies of metal dissolution from battery electrode materials. A number of different cell setups and sophisticated experiments have been designed to investigate and monitor the behavior of Mn-based battery materials *in situ* and *operando* in recent years. Hanf et.al. employed capillary electrophoresis with UV/Vis detector to evaluate the stability of $LiNi_{0.5}Mn_{1.5}O_4$ (LNMO), different electrolytes with different pH values to analyze the degradation products. The results showed the soluble Mn species to be either $Mn^{(II)}$ or $Mn^{(III)}$, depending on the electrolyte used [95]. Nikman et. al. and Wang. et. al provided the improvement over these experiments by *operando* analysis through online ICP-OES and cell-embedded Pt sensor, respectively, to analyze not only the degradation products but also relate it to the state of charge of the material, at which the degradation occurred [96,97]. Both of them found $Mn^{(II)}$ to be the main soluble product, being produced at overcharged or over-discharged states of active material. Unfortunately, no similar experiments have been conducted for ASIBs.

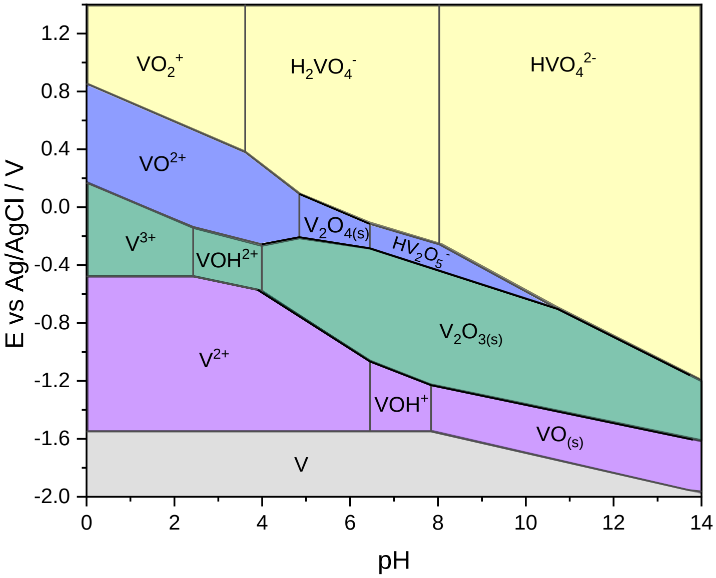

Figure 2. Pourbaix diagram for vanadium in diluted (10^{-5} M) aqueous solutions.

In the case of vanadium-based electrode materials, the dissolution of vanadium into the electrolyte is widely recognized as a primary degradation mechanism [98–106]. This phenomenon, which is especially notable in aqueous media, has implications for the long-term performance and durability of these materials. The dissolution products can contain vanadium in different redox states, depending on pH of the media and electrode potentials (Fig. 2).

Unfortunately, most of the research concerning V-based electrodes focused on Zn-ion batteries, employing vanadium oxides as positive electrodes. In this work, *in situ* degradation studies of selected materials were carried out. Overall chemical and electrochemical stability was also assessed through *post mortem* analysis using XRD and EDX.

1.5. Degradation mitigation techniques

The simplest solution to mitigate electrode degradation is based on electrolyte modification [107]. This has been widely employed in the field of organic electrolytes. Wang et al. identified that adjustments in dielectric constants can significantly reduce the solubility of species in the electrolyte, thereby improving the lifespan of Li-ion batteries [36]. Furthermore, the introduction of fluoride anion-containing salts further enhanced the stability by forming a protective fluoride-containing layer on the surface of the electrodes [37]. This solid electrolyte interphase (SEI) consisted of an ion-conducting layer formed by the products of the electrode in combination with the electrolyte decomposition products.

In aqueous systems, a similar concept has been explored by reducing the solubility in the electrolyte through the use of highly or super-concentrated electrolyte solutions [102,108,109], also known as "water-in-salt" systems. They basically expand the operating window of the aqueous electrolyte by decreasing water activity, which also suppresses the dissolution of active materials or metal leaching. This approach holds promise for enhancing the performance and lifespan of aqueous battery systems, however, they remain far from practical applications due to associated cost [110].

In the context of diluted aqueous electrolytes, some approaches have been proposed to address the issue associated with the leaching of Mn from the electrodes. The simplest one was to use $Mn^{(II)}$ additive to the electrolyte, which would shift the reaction equilibrium, favoring the stability of the initial material according to the Le Châtelier principle [111]. However, some studies reported a shift in the operating potentials, suggesting that improvement of the performance is not due to the preservation of initial active material, but rather due to the deposition/stripping of manganese oxides (MnO_{2-x}) on the electrode surface [112,113].

Another approach to mitigate the degradation of the electrode/electrolyte interface in aqueous media involves the introduction of protective coatings.

These coatings can have different chemical nature and composition. For the sake of simplicity, we can categorize them into three groups: (i) inorganic coatings, (ii) polymeric coatings, and (iii) carbonaceous coatings. Among these, carbon coatings are the most widely used. This is typically achieved by blending the material with an organic precursor and pyrolyzing it in an inert atmosphere. Additionally, carbon serves as an electronic conductor, thus lowering the overall charge transfer resistance of the electrode [114].

Ceramic inorganic coatings include a wide range of inert materials to mechanically protect the surface from chemical attack and suppress the dissolution. For example, coating the particles with $AlPO_4$ using chemical deposition has been successfully employed to increase the capacity and capacity retention of $Li[Li_{0.2}Fe_{0.1}Ni_{0.15}Mn_{0.55}]O_2$ electrodes in Li-ion batteries [115]. In the presence of water, phosphate coatings might also provide the benefit of creating a local buffer on the electrode surface, effectively mitigating pH fluctuations, and preventing proton co-insertion or proton-induced disproportionation. Another approach involves the application of conformal inorganic coatings directly on the electrode surface. Techniques like atomic layer deposition (ALD) provide a controlled method for coating particles or surfaces [116–119]. The precise control of coating thickness is crucial due to the typically low conductivity of the coating materials which can significantly increase charge-transfer resistance. The method also has the advantage of being carried out at lower temperatures than typical carbon pyrolysis and, therefore, can be applied to thermally unstable materials. Nano-scale coatings of Al_2O_3, TiO_2, or HfO_2 have already been implemented in organic SIBs, resulting in improved capacity retention [120].

Another type of coating that has been relatively underexplored is based on conducting polymers. These materials are very interesting since they combine the advantageous properties of polymers, such as chemical durability, with ionic and/or electronic conductivity [121]. These properties can be further enhanced through appropriate doping. Since their discovery in the 1970s, conducting polymers have shown promise in various applications, including solar cells [122], sensors [123], and other electrochemical devices [124–126]. Conducting polymers can indeed offer decent specific capacities, reaching up to 80 mAh g^{-1} in Li^{-}ion cells, thanks to their ability to incorporate small ions. Therefore, in battery applications, composites of inorganic active materials and polymers appear to hold a more significant promise. In 2019, Lepage et al. successfully employed a poly(3,4-ethylenedioxythiophene) (PEDOT) polymeric layer to suppress the corrosion of aluminum current collectors in high-voltage Li-ion batteries [127]. Subsequently, Zeng et al. and Kamenskii et al. enhanced the performance of Zn/MnO_2 batteries with PEDOT and polystyrene sulfonate-doped PEDOT(PSS) coatings, respectively [128,129]. In Na-ion batteries, Lee et al. also utilized PEDOT to enhance the performance of NVP electrodes in $LiPF_6$ organic electrolytes [130]. However, research in ASIBs using conducting polymers remains relatively limited. Conducting polymers, such as PEDOT could be electrochemically deposited on conductive substrates to deposit uniform layers. However, on electrochemically active substrates, such as battery electrodes, the process might be challenging because PEDOT deposition from aqueous solution occurs at ca. 0.8 V vs Ag/AgCl. This overlaps with the redox potential of most of the positive electrode materials. It is, therefore, difficult to deposit the polymeric layer without driving the electrochemical reaction in an active material. Thus, typically, chemically polymerized PEDOT is used [127,130], which gives arise to another challenge associated with the quality of films and the presence of excess oxidizing agent (typically Fe^{3+}). Another interesting potential coating material is Nafion. Originally developed as a proton-conductive membrane for low-temperature fuel cells, Nafion's ionic conductivity has led to its use as a separator membrane [131] and electrolyte [132] in organic Na-ion batteries. However, research, exploring its protective properties in aqueous media is lacking.

In this work, specific mitigation techniques were tailored to materials based on identified degradation mechanisms. ALD-deposited Al_2O_3, TiO_2, and HfO_2 were employed as conformal electrode coatings to prevent the parasitic reactions and degradation occurring during the electrochemical cycling of NTP. PEDOT and Nafion coatings were also successfully applied on NTP.

2. EXPERIMENTAL METHODS

2.1. Material synthesis

$NaTi_2(PO_4)_3$ (NTP) used in this work was synthesized via hydrothermal method. In a typical synthesis, CH_3COONa (0.246 g, Chempur, 99.0%) was dissolved in H_3PO_4 (10 mL, Reachem, 85 wt%), and then CH_3COOH (10 mL, Lach-ner, 99.8%) together with CH_3CH_2OH (40 mL, Honeywell, 99.8%) were added to the mixture. Afterward, a separate mixture of $C_{16}H_{36}O_4Ti$ (1.4 mL, Acros Organics, 98%) and H_3CH_2OH (10 mL) was prepared and added dropwise into the previous solution under magnetic stirring. The transparent final solution obtained after continuous stirring for 30 min at room temperature was transferred into a 100 mL Tefon-lined stainless-steel autoclave heated to 140 °C and kept for 12 h. Eventually, the obtained white precipitate was collected, washed several times by centrifugation with distilled water and ethanol, and subsequently dried at 80 °C overnight. The resulting particles were coated with a layer of carbon by homogeneously mixing 0.8 g of additionally ball-milled (1 h at 900 rpm) NTP powder and glucose (0.2 g) in distilled water (~50 mL). The resulting mixture was heated at 60 °C under magnetic stirring, and subsequently dried at 80 °C for water elimination. The obtained white powder was reground and annealed at 700 °C for 2 h in an N_2 atmosphere.

$Na_3V_2(PO_4)_3$ (NVP) samples were synthesized using the conventional solid-state method. In a typical synthesis, stoichiometric amounts of V_2O_5 (Thermo Fisher, 99.2%), Na_2CO_3 (Chempur, 99.8%), and $NH_4H_2PO_4$ (Honeywell, 99%) were mixed using wet (2-propanol) ball-milling (Retsch, PM 400) at 350 rpm for 2 h. The resulting mixture was dried at 70 °C and the powder was annealed in a tube furnace under a flowing forming gas (5% H_2 + 95% N_2) atmosphere for 4 h at 400 °C and 8 h at 800 °C with intermediate regrinding. The obtained powder was milled in a planetary ball-mill at 350 rpm for 2 h. In order to enhance electronic conductivity, the powder was additionally coated with carbon by pyrolysis of citric acid (CA). For this purpose, NVP and CA were first dispersed in distilled water at 8:2 weight ratio, then dried at 70 °C, and annealed at 700 °C for 2 h in a flowing N_2 atmosphere.

$Na_3V_2(PO_4)_2F_3$ (NVPF) samples were prepared using aqueous sol-gel synthesis to avoid any undesired interactions between fluoride precursor and ball-mill components during solid-state synthesis. In a typical process, stoichiometric amounts of NaF (Chempur, 99%) and NH_4VO_3 (Reachem, 99.5%) were dissolved in deionized water. Next, $NH_4H_2PO_4$ (Honeywell, 99%) and citric acid (CA) (Lach-Ner, 100%) (molar ratio of V:CA = 1:0.8) were added into the same solution. The obtained solution was left on a hot plate overnight in order to evaporate water. The resulting powder was annealed at 300 °C for 4 h and then at 700 °C for 8 h in the flowing N_2 atmosphere with intermediate regrinding. The obtained NVPF powder had ~5 wt% of carbon due to pyrolysis of CA as determined by thermogravimetric analysis (TGA).

$Na_3MnTi(PO_4)_3$ (NMTP) was synthesized by a conventional solid-state method. In a typical synthesis, stoichiometric amounts of Na_2CO_3 (Chempur, 99+%), $MnCO_3$ (Chempur, 99+%), TiO_2 (Alfa-Aesar, 99+%), and $NH_4H_2PO_4$ (Chempur, 99+%) were mixed using wet (2-propanol) ball milling (Retsch PM400) at 350 rpm for 2 h. The dried powder was calcined under a flowing nitrogen atmosphere for 8 h at 600 °C and then for 8 h at 650 °C with intermediate regrinding. The obtained material was additionally processed at 350 rpm for 2 h using high-energy ball milling. Then it was coated with a layer of carbon by homogeneously mixing $Na_3MnTi(PO_4)_3$ (0.8 g) and glucose (0.2 g, Glentham, 99.5+%) in deionized water, drying the resulting mixture at 80 °C for water elimination, and heating it at 650 °C for 8 h in a flowing nitrogen atmosphere.

$Na_4Mn_3(PO_4)_2P_2O_7$ (NMPP) was also synthesized by a conventional solid-state method. In a typical synthesis, stoichiometric amounts of $Na_4P_2O_7$ (ChemPur, p.a.), MnC_2O_4 (ChemPur, p.a.), and $NH_4H_2PO_4$ (Honeywell, 99+%) were mixed using wet (2-propanol) ball milling at 350 rpm for 2 h. The dried mixture was calcined at 300 °C for 6 h and subsequently at 600 °C for 6 h, all in an ambient air atmosphere. The obtained material was additionally processed at 350 rpm for 2 h using high-energy ball milling. Then it was coated with a layer of carbon by homogeneously mixing the material (0.8 g) and glucose (0.2 g, Glentham, 99.5+%) in deionized water, drying the resulting mixture at 80°C for water elimination, and heating it at 650 °C for 8 h in a flowing nitrogen atmosphere.

$Na_3MnPO_4CO_3$ (NMPC) was synthesized by a hydrothermal method. In a typical synthesis, Na_2CO_3 (10 g, ChemPur, 99.8%) together with $(NH_4)_2HPO_4$ (2.6412 g, ThermoFisher, 98%) were dissolved in 50 ml of water to form a clear solution. Simultaneously, $Mn(NO_3)_2$ (10 mL, ChemPur 1 M solution) was dissolved in 25 mL of water and then quickly transferred to the first solution under vigorous magnetic stirring. The white suspension obtained after continuous stirring for 30 min at room temperature was transferred into a 100 mL Teflon-lined stainless-steel autoclave and heated at 180 °C for 15 h. The obtained light brown precipitate was collected and washed several times by centrifugation with distilled water and acetone, and subsequently dried at 80 °C overnight.

After coating by carbon, all the materials were additionally ball-milled for 2 hours to ensure particle size uniformity.

2.2. Electrode preparation

Electrodes were prepared by casting the slurry as 300 μm thick wet film on the aluminum foil. The slurry was prepared by mixing 70 wt% of active material with 20 wt% carbon black (Super-P, TIMCAL) and 10 wt% polyvinylidene fluoride (PVDF, HSV1800, Kynar) in N-methyl-2-pyrrolidone (NMP) (Sigma Aldrich, 99.5%). The amount of NMP was varied to achieve the desired viscosity of the slurry and was dependent on the active material used, typically with a ratio of 1:3. The slurry was homogenized for 1 h in a planetary ball-mill at 350 rpm. After casting, materials were dried for at least 3 h at 120°C in a vacuum oven (VO29, Memmert GmbH). For the electrode preparation, dried films were cut into 13 mm diameter discs and pressed to 316 L stainless steel mesh using a laboratory hydraulic press. For EDX/XRD measurements during degradation studies of the electrodes, part of the active material was replaced by 20wt% HfO_2, serving as an internal standard. The summary of different electrode preparations, with corresponding material synthesis routes, carbon coating precursors, and active material loadings is presented in Table 1.

For rotating ring-disc electrode (RRDE) measurements, the slurry preparation procedure was identical to the one employed for conventional electrodes. After mixing, the slurry was drop-casted on the surface of the carbon disc electrode and dried overnight. Vacuum could also be used to accelerate the drying process, however, in some cases, visible cracks appeared on the surface of materials due to the rapid evaporation of the solvent. Therefore, ambient drying conditions were preferred.

Table 1. Summary of prepared electrodes for all materials

Electrode	Synthesis route	Carbon precursor	Active material loading / mg cm^{-2}
NTP	Hydrothermal	Glucose	2.1 ± 0.3
NVP	Solid-state	CA	2.2 ± 0.7
NVPF	Sol-gel	CA	2.6 ± 0.4
NMTP	Solid-state	Glucose	2.3 ± 0.7
NMPP	Solid-state	Glucose	2.6 ± 0.3
NMCP	Hydrothermal	-	1.8 ± 0.2

Active material loadings were dependent on the material used. For RRDE measurements, the active material mass (~0.3 mg) was much lower than the mass of the RRDE tip (~35 g). Therefore, the active material loading was estimated indirectly from the capacity. For this purpose, a galvanostatic charge capacity measurement of NTP was carried out on RRDE set-up and mass was recalculated based on the recorded capacity.

Electrochemical deposition of PEDOT on the surface of NTP electrodes was conducted using a simple bottom-mounted cell with a solution containing 0.01 M 3,4-ethylenedioxythiophene (EDOT, Acros organics, 99%) and 0.1 M poly(sodium 4-styrene sulfonate) (NaPSS, Acros organics). The galvanostatic deposition was chosen due to its simplicity and ease of charge control, with a current density of 0.2 mA cm^{-2} applied. These conditions have been proven to produce uniform polymer coatings in previous studies [133,134]. Coating thickness was controlled by varying the deposition time from 0 to 10 min.

Nafion was deposited from the 5% solution in 1:1 water:1-propanol (Ion power Inc. D521). Initially, 25 and 50 µL of the solution was drop-cast on the surface of the electrodes and dried overnight. For thinner coatings, a spin coater was employed. To minimize the effects of the uneven surface of the SS mesh on the coatings, the mesh-transferred electrodes were further pressed onto conductive carbon paper (XVCF-3.5S200, Caplinq).

For the ALD deposition, exposure mode was selected which is based on the prolonged substrate exposure to the precursors, allowing the coating of the porous structures, such as carbon composites [135]. The procedure was carried out in Fiji F200 ALD deposition system (CambridgeNanotech) at 170 °C. Trimethylaluminum ($Al_2(CH_3)_6$), tetrakis(dimethylamino) titanium ($Ti(N(CH_3)_2)_4$), and tetrakis(dimethylamino)hafnium ($Hf(N(CH_3)_2)_4$) (>98% purity, Strem) were used as metal precursors. Deionized water was employed as an oxygen precursor. A constant flow of 140 sccm of Ar as a carrier gas was maintained during the process, resulting in 0.3 mbar of base pressure in the reaction chamber. The deposition cycle consisted of a sequence of 0.2 s precursor pulse, 20 s exposure time, 20 s purge time, 0.2 s deionized water pulse, 20 s exposure time, and 20 s purge time. The coating thickness was determined by analyzing the simultaneously coated Si wafer. The ALD layer thickness on the Si wafer was measured using a dual rotating compensator ellipsometer (RC2, J.A. Woollam, Co., Inc.) in the 300 nm - 900 nm spectral range. This result was used as a way to estimate the thickness of the coating layer on the surface of electrodes. Different amounts of ALD cycles were necessary to achieve similar coating thicknesses for different precursors.

2.3. Electrochemical measurements

In this work, cyclic voltammetry (CV) measurements were used to initially characterize and observe the changes in the electrochemical response of the materials. The measurements were performed in a custom-built bottom-mount beaker-type three-electrode cell specifically designed for flat samples. Ag/AgCl/KCl sat. (Redoxme AB, Sweden) and graphite rod (Redoxme AB, Sweden) were used as reference and counter electrodes, respectively. 1 M Na_2SO_4 (aq.) (Na_2SO_4 anhydrous, ChemPur, p.a) was used as an electrolyte solution for all electrochemical measurements unless specified otherwise. Electrolyte volume was typically 15 mL. Scan rate and potential ranges were individually selected for each studied material and experiment.

Galvanostatic charge/discharge (GCD) cycling was employed to study the initial capacity, as well as the long-term stability of materials. The same custom-made cells were employed as for CV measurements and the reference electrode was replaced with $Hg/HgSO_4/K_2SO_4$ to avoid chloride ion contamination during prolonged measurements. All GCD cycling experiments were performed on a Neware CT-4008-5V10mA battery cycler.

The GCD rate can be expressed as current density (A g^{-1} or A cm^{-2}), however, for most practical applications, as well as in this work, it is more common to use a C-rate. 1 C refers to the current, that is required to theoretically charge the electrode in 1 h. For this, the specific capacity of material (most commonly expressed in mAh g^{-1}) is required and can be calculated as:

$$Q_{theor} = \frac{nF}{3.6 * M_w}, \text{mAh g}^{-1} \quad (7)$$

where F is Faraday's constant (96485.3 As mol^{-1}), n is the number of electrons transferred per mole of active material and M_w is the molar mass of the material (g mol^{-1}). 3.6 is a conversion coefficient between coulomb (A s^{-1}) to more commonly used unit for battery capacity, mAh. 1C rate can be calculated by multiplying Q_{theor} by the active material mass in the electrode.

Electrochemical impedance spectroscopy (EIS) was employed to study the degradation, as well as the effects of different coatings on NTP. The measurements were carried out in custom-made cells, employing 1 M Na_2SO_4, Ag/AgCl/ KCl std., and graphite rod as electrolyte, reference, and counter electrodes, respectively. The measurements were performed in the 1 Hz – 10 kHz range in a potentiostatic mode with 5 mV potential amplitude during the discharge phase at -0.8 V vs. Ag/AgCl (discharge plateau of NTP).

The obtained data were fitted to equivalent circuits with the open source *impedance.py* package [136].

To study the degradation process *in-situ*, the RRDE method was employed. The RRDE tip (Metrohm Autolab) was fitted with a 5 mm diameter glassy carbon disc and a thin concentric platinum ring, with an insulating gap of 375 µm in width. The measurements were carried out in a 3-electrode cell, employing Ag/AgCl (Metrohm Autolab) and Pt sheet (Metrohm Autolab) as reference and counter electrodes, respectively. The electrolyte used was standard 1 M Na_2SO_4, unless specified otherwise. The measurements were recorded on a potentiostat-galvanostat (PGSTAT302N, Metrohm Autolab) equipped with a dual-mode bipotentiostat module for working with two working electrodes sharing the same reference and counter electrodes simultaneously. Typical electrolyte volume was ~100 mL.

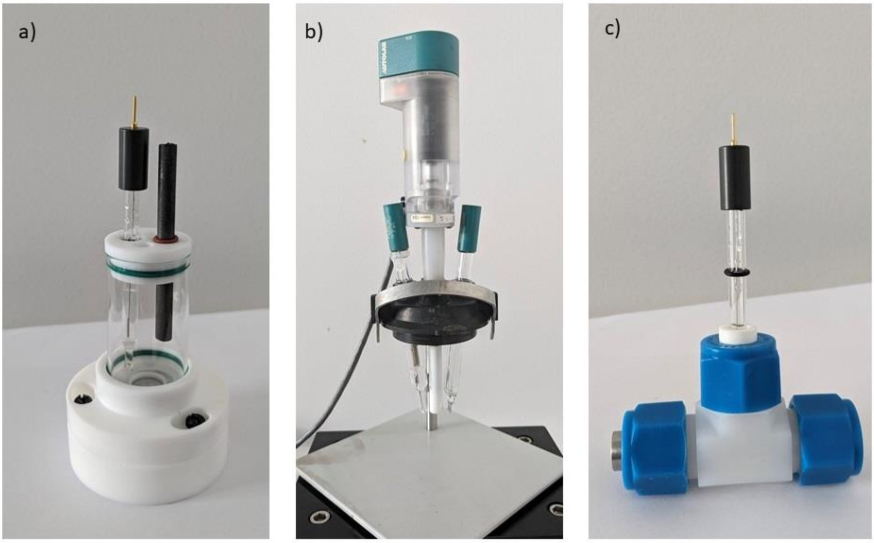

Figure 3. Set-ups used for electrochemical characterization. a) bottom-mounted beaker cell, b) rotating ring-disc electrode, and c) Swagelok-type (T-type) cell.

For quantitative characterization, one of the key parameters of interest in RRDE measurements is the collection efficiency, which refers to the ratio of the analyte collected on the ring electrode compared to the reaction products generated on the disc electrode. This parameter provides important quantitative information about the efficiency of the electrochemical reaction and the transfer of species between the disc and ring electrodes. In the case of equal-electron reactions for both disc and ring, efficiency will be the ratio of current magnitudes:

$$\eta = -\frac{I_{\mathrm{ring}}}{I_{\mathrm{disc}}} \tag{8}$$

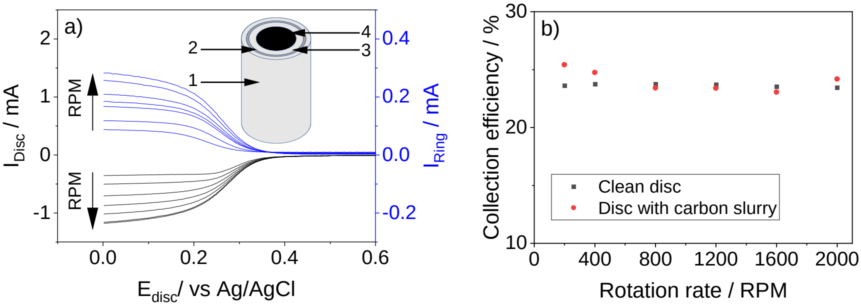

Figure 4. a) Schematic representation of RRDE and b) calibration of collection efficiency using $[Fe(CN)_6]^{4-}$/$[Fe(CN)_6]^{3-}$ couple. a) 1 – polyvinyl chloride body of the electrode, 2 – Pt ring electrode, 3 – insulating layer, 4 – glassy carbon disc electrode.

The parameter is independent of the reactions involved or rotation rate and solely depends on the geometry of the RRDE tip. The manufacturer reported theoretical collection efficiency was 24.9%, however, occasional re-calibration is preferred to account for surface changes during the usage. To account for the non-hydrodynamic nature of a material deposited on the disc electrode, additional in-house calibration was carried out using a carbon paste-modified disc and ferrocyanide redox pair. During the calibration process, the oxidation of $[Fe(CN)_6]^{4-}$ is induced on the disc electrode, while the ring electrode is maintained at negative potentials to detect the current resulting from the reduction of the $[Fe(CN)_6]^{3-}$. The resulting currents are recorded, and this measurement is repeated at different rotation rates. In theory, the collection efficiency, which represents the ratio of detected and produced species (or ratio of recorded currents, adjusted for electron number in the reactions) is expected to be independent of the rotation rate. However, in practice, there can be some dependency on the rotation rate, particularly when uneven or non-uniform surfaces are utilized. The observed collection efficiency was slightly rotation rate dependent and some turbulence was observed above 1600 rpm. The rotation rate of 1200 rpm and the corresponding re-calibrated collection efficiency of 23.4% were used throughout this work. This difference is assumed to be insignificant as most of the analysis is of qualitative nature.

To mimic and study the deposition of MnO_x on Pt surface, an electrochemical quartz crystal microbalance (EQCM) was employed. The measurements were performed using a QCM922 (Seiko) EQCM connected to a PGSTAT-302 (Metrohm Autolab) potentiostat/galvanostat through a signal splitter with a low-pass filter. Platinum-plated 6 MHz quartz crystals (Intellemetrics) were used as sensors in a 50 mL three-electrode electrochemical cell. The electrode active area was 0.5 cm^2. The frequency measurement resolution was 1 Hz. EQCM sensitivity calculated from the Sauerbrey equation was 12.27 ng Hz^{-1} cm^{-2}. MnO_x was deposited potentiostatically at 1.2 V vs. Ag/AgCl from the solution containing 0.1 M $MnSO_4$ and 0.9 M Na_2SO_4 as a background electrolyte.

2.2. Physiochemical characterization

Powder X-ray diffraction patterns of the materials and electrodes were recorded on Bruker D2 Phaser X-ray diffractometer within the range $5° < 2\theta < 70°$ using Ni-filtered Cu K_α radiation. The scanning speed and step width were 3° min^{-1} and 0.02°, respectively.

High-resolution Scanning Electron Microscope (SEM) micrographs of electrodes were recorded on Hitachi SU-70 microscope using 5.0 kV acceleration voltage. Images were captured near the center of an electrode. Low-resolution imaging and energy dispersive X-ray spectroscopy (EDX) analysis was performed on a table-top SEM (Hitachi TM-6000) equipped with an EDX detector.

Thermogravimetric analysis (TGA) for the determination of carbon content in active material was carried out on PerkinElmer STA6000 analyzer in the temperature range of 30 to 700 °C at a heating rate of 10 °C min^{-1} in an air atmosphere (20 mL min^{-1}).

XPS analyses were performed on the Kratos Axis Supra spectrometer using monochromatic Al-K_α radiation ($h\nu = 1486.7$ eV) with X-ray gun power of 225 W at 10^{-8} torr pressure and room temperature. The analyzed area at the sample center was approximately 0.16 mm^2 in size and high-resolution selected area scans were acquired using pass energy of 20 eV. A built-in charge neutralizer was employed to compensate for sample charging during the measurement. The samples were also electrically isolated from the sample holder bar to avoid preferential charging effects. The binding energy scale of recorded spectra was corrected by referencing to C 1s peak at 284.8 eV. The peak fitting of recorded spectra was performed using Kratos Escape software.

Shirley background function was applied for fitting the Ti $2p_{3/2}$ and C 1s spectra whereas a linear background function was used for Ti $2p_{1/2}$.

The chemical stability of the vanadium-based materials was evaluated by a simple immersion test. Mesh-transferred electrodes were immersed in the electrolyte solution (1 M Na_2SO_4) for a variable time under ambient conditions. In order to evaluate the extent of chemical or electrochemical degradation of the electrodes, double redox titrimetry was employed. For this purpose, the collected electrolyte (~12 mL) was transferred into a 25 mL measurement flask and filled with 4 M H_2SO_4 (aq.) (Lach-Ner). After that, to ensure the experiment's repeatability, it was split into three identical samples (8.33 ml each) and titrated with $2.5 \cdot 10^{-3}$ M $KMnO_4$ (aq.) (Chempur, 99.5%) until the color of the solution changed from colorless to purple, corresponding to full oxidation of all vanadium species to $V^{(V)}$. Subsequently, $V^{(V)}$ was reduced back to $V^{(IV)}$ by adding an excess of $(NH_4)_2Fe(SO_4)_2$ (Chempur, 99.5%). The remaining iron was oxidized to $Fe^{(III)}$ by adding $(NH_4)_2S_2O_8$ (Chempur, 98%) to avoid any undesired interference between $Fe^{(II)}$ and MnO_4^- during final titration. The final titration, corresponding to the oxidation of $V^{(IV)}$ into $V^{(V)}$ was performed with the same $KMnO_4$ (aq.) solution. This procedure provides information not only on the total vanadium concentration but also on its average oxidation state in solution [137].

In order to determine the amount of vanadium remaining in the cycled electrodes, they were transferred into a 2 M HNO_3 (aq.) (Lach-Ner) solution and dissolved in an ultrasonic bath. Insoluble solid particles, mainly containing carbon and PVDF binder were separated in a centrifuge, and the solution was analyzed with Perkin Elmer Optima 7000DV inductively coupled plasma optical emission spectrometer (ICP-OES) in order to determine the vanadium elemental concentration. Calibration was performed by preparing appropriately diluted stock standard solutions (single-element ICP standards 1000 mg L^{-1}, Roth).

3. RESULTS AND DISCUSSION

3.1. Investigation of degradation mechanisms of $NaTi_2(PO_4)_3$ in aqueous electrolytes

In this study, the common parasitic reactions that can take place during the operation of $NaTi_2(PO_4)_3$ as a negative electrode in an aqueous Na_2SO_4 solution are explored. Their impact on the material electrochemical performance and stability is assessed. For this, standard electrochemical techniques such as cyclic voltammetry and galvanostatic charge/discharge cycling were employed. Additionally, the results were supplemented by scanning electrochemical microscopy of the electrode surface. The results show significant irreversible side reactions with chemical oxygen reduction reaction (ORR) being the dominant one. These reactions lead to a rise in pH and eventual dissolution of the active material. pH buffering and ALD coating as strategies to mitigate this degradation are explored. The results of this work have been summarized and published as a part of an article [138].

$NaTi_2(PO_4)_3$ is one of the most studied negative electrode materials for Na-ion batteries. It owes its performance to the reversible redox reaction of $Ti^{(III)}/Ti^{(IV)}$, accompanied by simultaneous (de)insertion of Na-ions:

$$\mathrm{NaTi_2(PO_4)_3 + 2e^- + 2Na^+ \leftrightarrow Na_3Ti_2(PO_4)_3} \qquad (9)$$

One of the factors that makes this material appealing is its relatively low operating potential of -0.6 V vs. SHE. However, in pH neutral electrolytes, this potential falls below the equilibrium HER potential (-0.41 V vs. SHE):

$$\mathrm{2H_2O + 2e^- = 2OH^- + H_2} \qquad (10)$$

This reaction may pose multiple challenges such as (i) H_2 gas production on the surface and the accumulation of bubbles within pores, lowering electrolyte access and causing capacity loss without active material degradation [139,140], (ii) gas release might elevate internal cell pressure, (iii) generation of OH^- ions, and elevation of the system pH. This increase in pH could potentially compromise the stability of the active material. The pH dependence of the potential of reaction (10) can be expressed as:

$$E = -0.059\mathrm{pH\,V} \qquad (11)$$

Assuming a lower potential limit of -0.7 V vs SHE for charging up the $NaTi_2(PO_4)_3$, one would need an electrolyte with a pH of ~12 to suppress the HER. The fact that in electrolytes with close to neutral pH the redox potential of $Ti^{(III)}/Ti^{(IV)}$ lies below that of HER, implies that $Ti^{(III)}$ should get oxidized by water [40]:

$$\mathrm{Na_3Ti_2(PO_4)_3 + 2H_2O \leftrightarrow NaTi_2(PO_4)_3 + 2Na^+ + 2OH^- + H_2} \quad (12)$$

The process should self-discharge the material and result in lower cycling CE.

Another possible side reaction, also leading to self-discharge, is the chemical ORR which is catalyzed by $Ti^{(III)}$ present in the reduced (sodiated) form of NTP (N3TP):

$$\mathrm{Na_3Ti_2(PO_4)_3 + O_2 + 2H_2O \leftrightarrow NaTi_2(PO_4)_3 + 4Na^+ + 4OH^-} \quad (13)$$

It is crucial to highlight the similarities and consequences of these processes on the material performance. Both the HER and the water-mediated self-discharge (Reaction 10 and 12) of the material generate hydrogen gas, potentially limiting the electrolyte access to the electrode, which can lead to some capacity loss. However, despite being undesirable, both self-discharge (Reactions 12 and 13) produce discharged NTP as the primary product and are not likely to be responsible for the observed capacity fade.

On the other hand, three parasitic reactions mentioned earlier share a common outcome: the production of OH^- ions and an increase in pH (at least locally). Previous research has demonstrated that NTP starts to degrade at pH > 11, and this process accelerates significantly at pH > 13 [24]. An important parameter that is affected by parasitic reactions and needs to be considered is the CE of the system. It can be expressed as:

$$\mathrm{CE} = \frac{Q_{\mathrm{discharge}}}{Q_{\mathrm{charge}}} \times 100\% \quad (14)$$

It is important to note that on top of the active material operation, these charges include parasitic reactions that may occur within the potential cutoffs. Hence, $Q_{discharge}$ and Q_{charge} are the sums of all anodic and cathodic reactions taking place on the surface of the electrode, respectively. In our case, there are no parasitic electrochemical anodic reaction to be expected at given potentials, however, self-discharge reactions (Reaction 12 and 13) may commence in pararel to electrochemical discharging (Reaction 9), leading to reduced recorded $Q_{discharge}$. The picture is different for Q_{charge}, which will potentially include the HER described above (Reaction 10). In addiiton, self-discharge reactions will have opposite effect, e.i. they will inflate the recorded capacity during the charging process and reduce the capacity during discharging. Therefore, the recorded CE can be used as a proxy parameter to assess the extent of the parasitic reactions.

One of the possible solutions to mitigate pH fluctuations is based on the use of buffered electrolytes. In this study, five different buffers with various pH values were evaluated. The buffers used were either phosphate (for pH 6, 7, and 8) or borate (for pH 9 and 10). The pH of the final solution was adjusted by adding H_2SO_4 and NaOH respectively. Through the measurements, Na^+ concentration was maintained constant, at 2 M, by matching appropriate amount of Na_2SO_4 to 0.1 M buffer. The capacities recorded under ambient conditions at 1C rate are depicted in the Fig. 5.

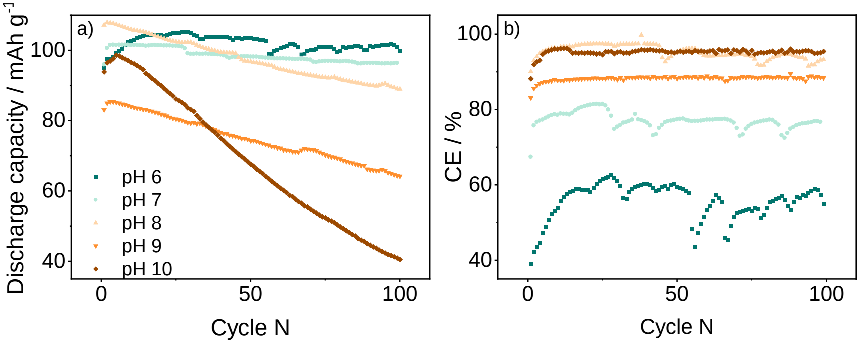

Figure 5. Variation of a) discharge capacity and b) Coulombic efficiency during GCD cycling of NTP electrodes in buffered electrolytes of different pH at 1C rate.

The results show that lower electrolyte pH yields better capacity retention of NTP. On the other hand, pH > 7 leads to faster capacity fade, particularly for pH 10, where it exceeds 60% after 100 cycles. The recorded CE show an opposite pattern. Lower pH values, appear to dramatically reduce the CE to as low as 50% after 100 cycles at pH 6. Another interesting observation is the fluctuating behavior of recorded capacities and efficiencies. This fluctuation is more pronounced at lower pH, suggesting that HER might cause it. In unbuffered electrolytes, the increase in electrolyte pH pushes the HER onset potential towards more negative values, making this process self-limiting. With buffer, however, this is not the case and this is further supported by the recorded CE. In summary, while electrolyte buffering and pH adjustments may seem advantageous, the CE data indicates that they may not offer a viable long-term solution for mitigating electrode degradation, particularly in real-world devices where processes occuring on the opposite electrode must also be considered.

Another challenge to address is the self-discharge of the material. N3TP is generated as a reduced form of NTP. N3TP then undergoes oxidation through Reactions 12 and 13, reverting to the initial form of the material. Both self-discharge reactions are thermodynamically possible under the conditions employed here but their contribution to overall lowered CE can be different. In order to estimate the contribution of Reaction 13 to self-discharge, NTP was charged at 1C under different conditions: (i) electrolyte in the ambient atmosphere; (ii) electrolyte pre-purged with oxygen; (iii) electrolyte under constant oxygen purging. The results presented in Fig. 6 a) show that under ambient conditions initial charging capacity is ~110 mAh g^{-1}, which is typical for NTP electrodes in diluted aqueous electrolytes. However, in pre-oxygenated electrolyte, the Q_{charge} exceeds 200 mAh g^{-1}, which is higher than the theoretical (133 mAh g^{-1}). This clearly indicates additional parasitic reactions. The constant flow of oxygen exaggerates this effect elevating the Q_{charg} to 500 mAh g^{-1}. In another experiment NTP electrode was initially charged at a 1C rate under ambient conditions and then the variation of the open circuit potential (OCP) of the electrode was monitored under (i) ambient atmosphere, (ii) under O_2 purging and (iii) under N_2 purging. In the absence of the self-discharge reactions, the potential is expected to stabilize around -0.8 V vs Ag/AgCl. However, as these reactions progress and the material becomes oxidized, the OCP should then gradually return to its initial value of ca. 0 V vs. Ag/AgCl. Initially, self-discharge was evaluated under ambient conditions. The results, shown in Fig. 6 b), demonstrate that under these conditions, self-discharge takes ca. 10 h. In order to mitigate Reaction 13, the electrolyte was purged with N_2, effectively removing dissolved O_2. This extended the stability of the charged state of NTP, maintaining its OCP at -0.8 V vs. Ag/AgCl for up to 35 h. More interesting are the results from the oxygenated media. In order to promote Reaction 13, the electrolyte was purged with oxygen. Under these conditions, the self-discharge becomes extremely fast and it only takes about 1 h for the electrode to be fully self-discharged.

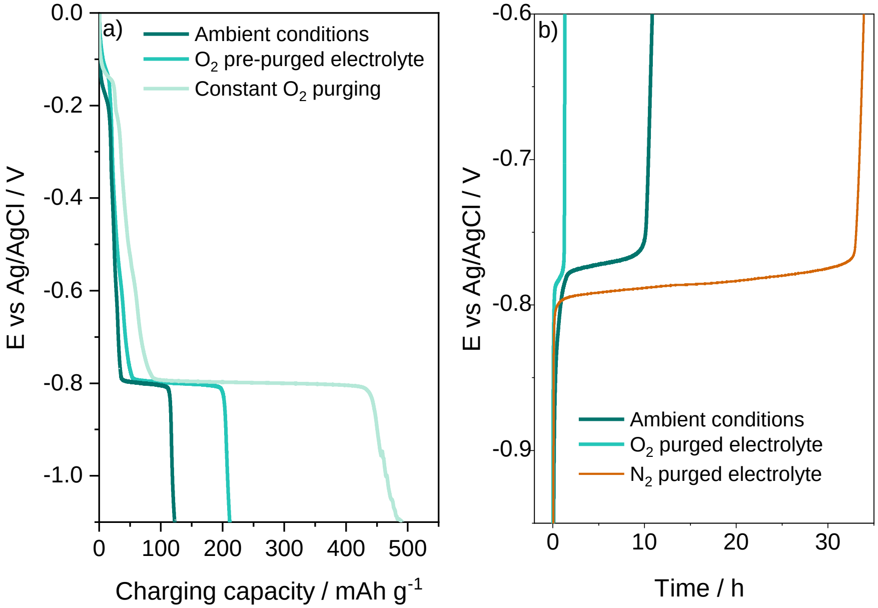

Figure 6. a) Potential *vs* capacity profiles recorded during charging of NTP electrode at 1C rate and b) variation of the open-circuit potential of precharged NTP electrode; measurements were performed in 1 M Na_2SO_4(aq.) electrolyte under conditions specified.

As demonstrated, self-discharge reactions lead to an increase in charging capacity, resulting in a reduced CE for the system. The entire self-discharge process lasting ca. 10 h under ambient conditions highlights its considerable contribution to the overall cycling process, even at a relatively fast charging rate of 1C. Therefore, increasing the speed of the cycling can mitigate the influence, but does not fundamentally address the issue; rather, it just masks it. However, the results also indicate that the majority of the NTP produced from the oxidation of N3TP through either pathway remains electrochemically active and capable of engaging in electrochemical reaction. Therefore, lower CE cannot be responsible for the capacity fade observed in NTP. However, incrase in pH during the self-discharge of NTP has been experimentally demonstrated [141].

Reaction 13 during self-discharge of NTP electrode was investigated *in situ* with the help of scanning electron microscope (SECM) operating in competition mode (Fig. 7). Competition mode means that the same redox process (e.g. ORR in this case) is possible on both: the surface of working NTP electrode, and the surface of Pt ultramicroelectrode (UME). The UME potential is set to (-0.5 V vs Ag/AgCl) corresponding to the ORR region. In the course of the experiment, NTP was fully charged and then left under open-circuit conditions in naturally aerated electrolyte while its surface was scanned with Pt UME simultaneously measuring its current. In Fig. 7, one can see that after about 12 h, which corresponds to the full self-discharge time of NTP under ambient conditions, the current on UME started increasing, which means that ORR on NTP stopped and was occurring on the UME.

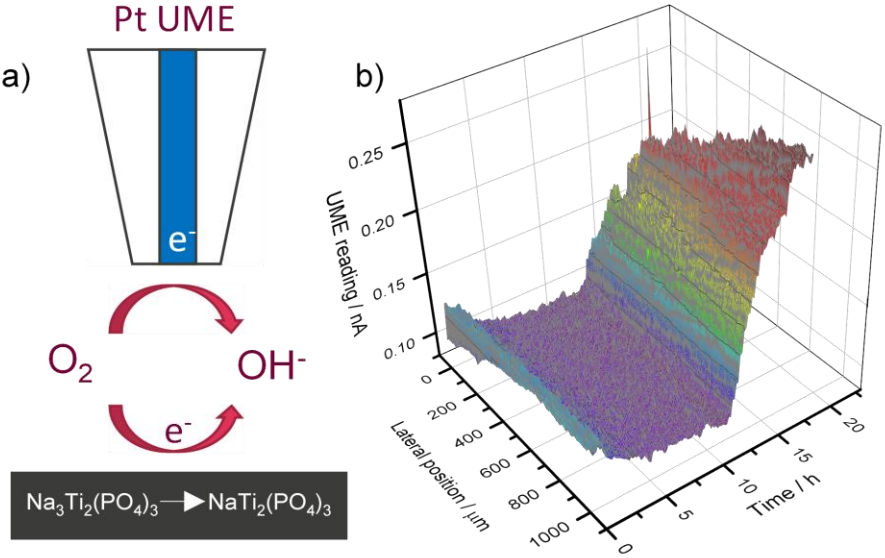

Figure 7. a) schematic representation of SECM operating in redox competition mode during self-discharge of N3TP and b) Pt ultramicroelectrode current recorded during the self-discharge of NTP under ambient conditions in 1M Na_2SO_4.

In conclusion, the findings underscore the significance of addressing parasitic reactions when utilizing NTP as a negative electrode material. The mechanism of the degradation for studied processes is similar, being the dissolution of the active material through elevated pH. Selecting pH-buffered electrolytes does not seem to be a viable choice, especially in real systems, with electrolyte-starved environments. Polymeric or inorganic surface coatings could present a more viable alternative, as they can both suppress the ORR, as well as protect the material from OH^-.

3.2. Aqueous stability of manganese-based framework phosphates as positive electrodes

Mn-based materials are attractive due to their properties such as multiple redox states, high operating potential, and abundance. However, they show active material leakage in both, organic and aqueous systems leading to capacity loss. Multiple techniques, such as electrolyte additives, have been employed in the past to suppress the dissolution of Mn oxide-based materials in different battery systems [111,142]. An alternative approach involves incorporating polyanions into the crystalline lattice, enhancing the stability of the structure against charge carrier ion (de)intercalation and pH fluctuations. In this study, three distinct compounds featuring mixed phosphate frameworks containing $Mn^{(II)}$ are investigated. Since purely Mn-based NASICON-structured phosphate materials have not been successfully synthesized yet, $Na_3MnTi(PO_4)_3$ was chosen as a representative system to examine the electrochemical properties of $Mn^{(II)}$ phosphate materials. Furthermore, the substitution of transition metals with Ti is known to have a stabilizing effect and can suppress Jahn-Teller distortions in certain Mn-based materials [80,81]. On the other hand, since some purely Mn-based mixed phosphates have been reported, they were selected for detailed investigation as well. The effects of the framework's anionic composition of $Na_4Mn_3(PO_4)_2P_2O_7$ and $Na_3MnPO_4CO_3$ as $Mn^{(II)}$-based mixed-phosphate materials were studied.

This work extensively examines the degradation of $Mn^{(II)}$ mixed phosphate framework materials in a simple dilute aqueous electrolyte (1 M Na_2SO_4) solution. The process was studied in real-time during the electrochemical operation of the electrode using the RRDE technique. These results are complemented by X-ray Photoelectron Spectroscopy (XPS), EQCM, and EDX. Despite its primary use in studying redox reactions under hydrodynamic control, the RRDE technique is also useful for *in situ* monitoring dissolution and deposition reactions [92]. It effectively allows the isolation of the electrochemical processes taking place in/on the working electrode (disc) from those on the auxiliary electrode (ring). In the case of Mn-based materials, the degradation products are swept away from the working electrode by forced convection and can be electrochemically detected using the concentric Pt ring [143–145]. The results clearly show that the capacity fade of $Mn^{(II)}$-based framework compounds in aqueous electrolytes is due to electrochemically-induced degradation. Some of the Mn dissolves chemically and electrochemically. *Post mortem* analysis revealed that a significant amount of Mn remains in the electrode, but becomes electrochemically inactive or inaccessible. These processes limit the performance of these materials as positive electrodes in aqueous Na-ion batteries unless effective strategies are developed to address these issues. The results of this study have been summarized and published [146].

Active materials were synthesized as described in the Experimental section. After coating, the carbon content was determined by thermogravimetric (TG) analysis, and was 4.1 and 4.9 wt% for NMTP and NMPP, respectively (Fig. 8). Differences in carbon content in coated materials can be attributed to particle size and are deemed to be insignificant. Due to the thermally unstable nature of NMCP as shown in Fig. 8 c), the typical carbon coating procedure (pyrolysis) was inapplicable. Therefore, AN uncoated material which was ONLY mixed with conductive carbon filler was studied.

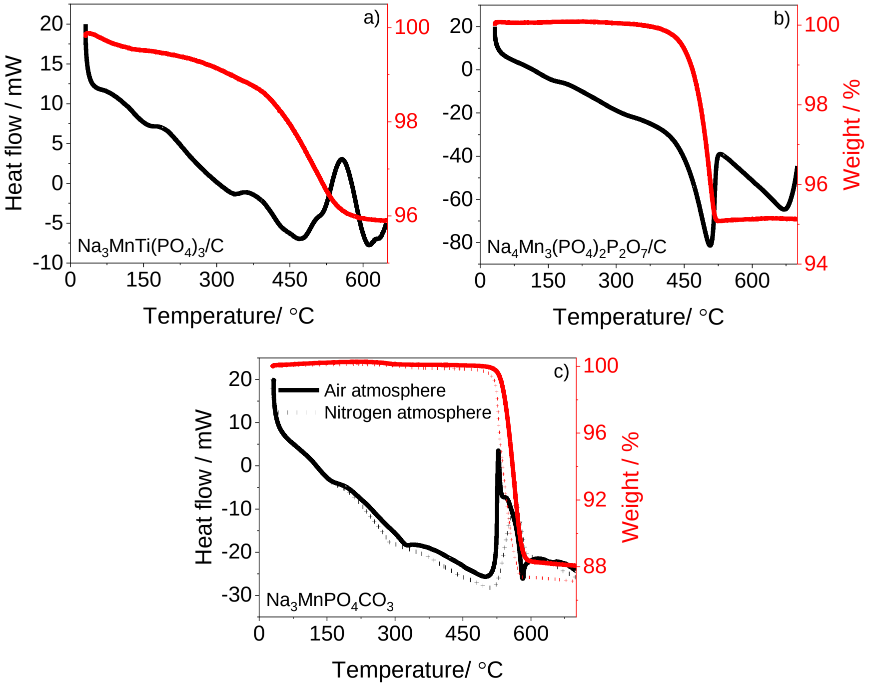

Figure 8. Thermogravimetric analysis of Mn-based phosphate materials: a) $Na_3MnTi(PO_4)_3$, b) $Na_4Mn_3(PO_4)_2P_2O_7$ and c) $Na_3MnPO_4CO_3$ recorded in air (solid red line) or N_2 (dashed red line) atmosphere.

Initially, it is assumed that the electrochemical activity in the studied potential range of all studied materials is due to Mn redox processes:

$$\mathrm{Mn^{(II)}} \leftrightarrow \mathrm{Mn^{(III)}} \text{ and } \mathrm{Mn^{(III)}} \leftrightarrow \mathrm{Mn^{(IV)}}$$

Therefore, two Na ions can be theoretically extracted/inserted from/to NMTP as well as NMPC:

$$\mathrm{Na_3Mn^{(II)}Ti(PO_4)_3} \leftrightarrow \mathrm{Na_2Mn^{(III)}Ti(PO_4)_3} + \mathrm{Na^+} + \mathrm{e^-} \quad 3.6\ \mathrm{V\ vs\ Na^+/Na} \quad (15)$$
$$\mathrm{Na_2Mn^{(II)}Ti(PO_4)_3} \leftrightarrow \mathrm{NaMn^{(IV)}Ti(PO_4)_3} + \mathrm{Na^+} + \mathrm{e^-} \quad 4.1\ \mathrm{V\ vs\ Na^+/Na} \quad (16)$$

$$\mathrm{Na_3Mn^{(II)}PO_4CO_3} \leftrightarrow \mathrm{Na_2Mn^{(III)}PO_4CO_3} + \mathrm{Na^+} + \mathrm{e^-} \quad 3.6\ \mathrm{V\ vs\ Na^+/Na} \quad (17)$$
$$\mathrm{Na_2Mn^{(III)}PO_4CO_3} \leftrightarrow \mathrm{NaMn^{(IV)}PO_4CO_3} + \mathrm{Na^+} + \mathrm{e^-} \quad 4.1\ \mathrm{V\ vs\ Na^+/Na} \quad (18)$$

In the case of NMPP, potentially three Na ions could be extracted with a maximum oxidation state of $\mathrm{Mn^{(III)}}$:

$$\mathrm{Na_4Mn_3^{(II)}(PO_4)_2P_2O_7} \leftrightarrow \mathrm{NaMn_3^{(II)}(PO_4)_2P_2O_7} + 3\mathrm{Na^+} + 3\mathrm{e^-}\ 3.8 - 4\mathrm{V\ vs\ Na^+/Na}\ (19)$$

Although NMTP also contains an electrochemically active $\mathrm{Ti^{(IV)}}/\mathrm{Ti^{(III)}}$ redox pair, its low potential (~2.1 V vs. Na+/Na) renders it irrelevant when the material is used as a positive electrode. Consequently, it will not be considered further in this discussion. The theoretical capacities calculated based on the above reactions are 117 mAh $\mathrm{g^{-1}}$, 129 mAh $\mathrm{g^{-1}}$, and 192 mAh $\mathrm{g^{-1}}$ for NMTP, NMPP, and NMCP, respectively.

The preliminary electrochemical characterization through CV was conducted using conventionally fabricated mesh-pressed disc-shaped electrodes within a standard bottom-mount beaker-type cell. The resulting CV curves for NMTP, NMPP, and NMCP are presented in Fig. 9. In the initial cycle, a common feature across all CVs is a pair of reversible redox peaks located approximately within the range of 0.8 - 0.9 V vs. Ag/AgCl in the anodic sweep and around 0.5 - 0.8 V vs. Ag/AgCl in the cathodic sweep. This distinctive pair of peaks can be attributed to a one-electron redox reaction involving $\mathrm{Mn^{(II)}}/\mathrm{Mn^{(III)}}$ transition alongside the insertion and extraction of $\mathrm{Na^+}$ ions. Notably, the peaks are more pronounced and exhibit greater reversibility in NMTP compared to the other materials. The second redox reaction, namely $\mathrm{Mn^{(III)}}$ to $\mathrm{Mn^{(IV)}}$ oxidation, seemed inaccessible in 1 M $\mathrm{Na_2SO_4}$(aq.) electrolyte due to the onset of the oxygen evolution reaction (OER) around 1.3 V vs. Ag/AgCl. Interestingly, despite the absence of an intrinsic carbon coating and the anticipated lower electronic conductivity, NMCP exhibits a notable electrochemical response that remains relatively consistent throughout the cycling process. All three systems exhibit an initial rapid electrochemical activity fade within the first ten cycles, indicative of fast active material degradation.

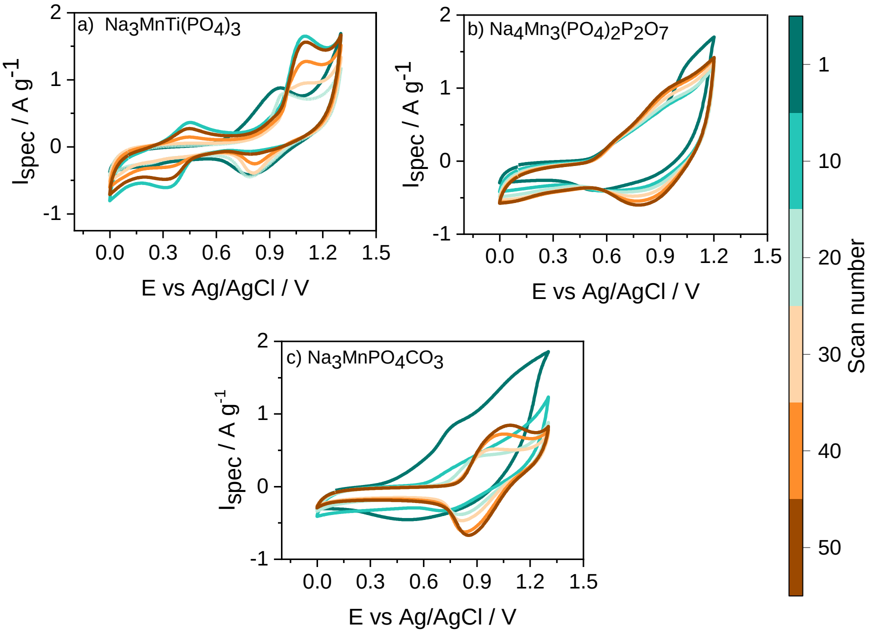

Figure 9. Variation of voltammetric response of a) NMTP, b) NMPP and c) NMCP electrodes during cycling in 1 M Na_2SO_4 in a bottom-mounted beaker cell at 10 mV s^{-1}.

The Mn dissolution from Mn-based electrode materials is a well-known phenomenon. In past studies, most of the degradation was attributed to this process [90]. Different approaches have been proposed to suppress the dissolution, such as electrode coatings or electrolyte additives [115,129,147]. The simplest approach is based on the introduction of soluble Mn$^{(II)}$ species as an additive in the electrolyte (such as $MnSO_4$) with the idea of shifting the dissolution equilibrium away from the formation of additional Mn$^{(II)}$(aq). This approach seemed promising, as initial results showed improved capacity retention for MnO_2 electrodes in aqueous Zn ion batteries [111]. However, upon further investigations, it was noticed that the operating potential of the electrode tended to shift with prolonged cycling, suggesting the formation of new electrochemically active Mn species, through the oxidation of the Mn$^{(II)}$ additive.

In this work, the formation of other electrochemically active Mn species is notable even in the absence of the additive. The diminished electrochemical activity of $Mn^{(II)}/Mn^{(III)}$ (0.8-0.9 V vs Ag/AgCl) and the appearance of the new peaks (ca. 0.3 V vs Ag/AgCl) are observed between cycles 10 and 50 (Fig. 9 a)). The whole process may include various (electro)chemical reactions, such as dissolution of the initial material and subsequent deposition of electrochemically active manganese oxides/phosphates, which may undergo Na^+/H^+ (de)insertion at different potentials. The formation of the dark brown precipitate was also observed on the surfaces of the working electrodes during cycling, confirming the idea.

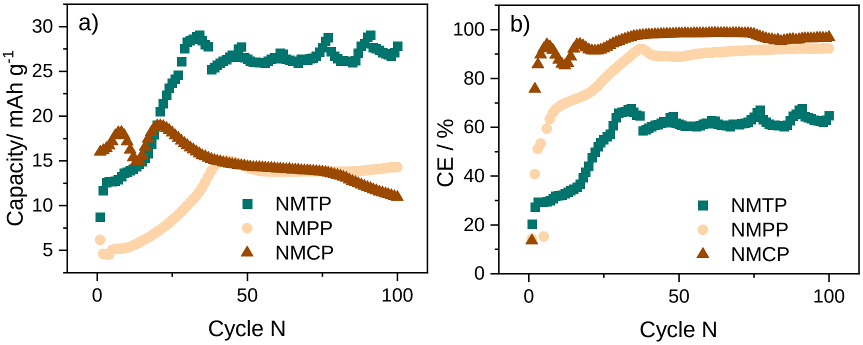

Figure 10. a) specific discharge capacities and b) CE recorded during GCD cycling at 1C rate or 117, 129, and 192 mA g^{-1} for NMTP, NMPP, and NMCP in 1 M Na_2SO_4,(aq.) respectively.

Galvanostatic charge/discharge measurements show very similar results to CV. As shown in Fig. 10, at 1C rate, the initial discharge capacity is very low ca. 5-10 mAh g^{-1} for all studied materials. In all three cases, this capacity starts to increase and reaches a maximum value after a certain number of cycles (ca. 40 cycles for NMTP and NMPP, and 20 cycles for NMCP). Again, this capacity could be attributed to the deposition and charge storage capacity of electrochemically active Mn oxides as was also observed in the CV experiments. Indeed, from the charge/discharge potential curves (Fig. 11), one can see that this increased capacity comes from a different cathodic process, taking place at a potential of 0.3-0.4 V vs. Ag/AgCl. The process is the most pronounced for NMTP.

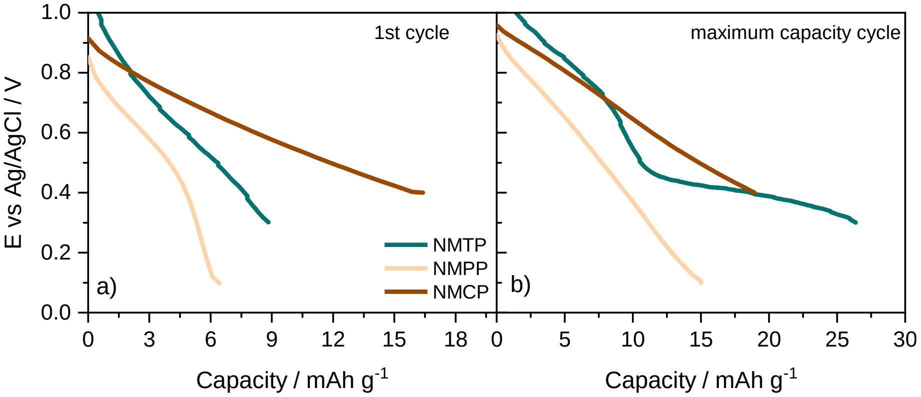

Figure 11. Potential *vs* capacity profiles corresponding to the a) first and b) maximum capacity cycles for for NMTP, NMPP, and NMCP recorded in 1 M Na_2SO_4(aq.) at 1C rate.

In order to better understand the processes in Mn-based phosphate electrode materials, another experiment was conducted in a Swagelok-type cell (Fig. 3 c)). In this case, an identical NMTP working electrode as in the beaker-type cell was used, whereas a 316L stainless steel disc was employed as a counter electrode. 20 GCD cycles were performed at a rate of 1C (117 mAh g^{-1}) to degrade the active material and produce similar soluble Mn-based degradation products as in the galvanostatic/potentiodynamic measurements described previously. Afterward, the polarity of the cell was reversed by polarizing the stainless-steel disc to ~1.2 V vs. Ag/AgCl (right below the OER potential) with NMTP serving as a counter electrode during this process. The conditions were maintained for 2 min in order to electrodeposit the dissolved $Mn^{(II)}$ species resulting from NMTP degradation on a stainless steel disc. After disassembly, two distinct-colored precipitates were observed on the stainless-steel disk. They were analyzed by XPS to estimate the composition of these precipitates. The light-colored part is composed of a P-rich phase (Mn/P ratio of ~0.7), while darker areas contain much less phosphorus (Mn/P ratio ~ 3.2) and much more oxygen. Overall, XPS measurements suggest that the degradation products of NMTP during electrochemical operation can be electrooxidized to Mn oxides/phosphates and deposited on the electrode. The electrochemical activity of these new species is responsible for the new peaks in CV, as well as apparent capacity retention during GCD, that was recorded in beaker-type cells. The results are in good agreement with previously reported results in the Swagelok-type set-up [97]. However, in typical battery-type full-cell setups with a limited amount of electrolyte, proximity of electrodes, and potential cross-talk there could be other reactions taking place such as the formation of insoluble $Mn^{(II)}$ phosphates which might themselves show some electrochemical activity [148].

It is generally difficult to assess the degradation process and mechanisms involved in electrochemically active materials. The main reason is that most of the characterization is done *post mortem*, such as structural characterization of used electrodes or elemental analysis of components. Few *in situ* methods have been successfully employed in the past. However, most of them are complicated and rely on in-house set-ups, making the results relatively hard to reproduce [95,96].

In this work, the electrochemical origin of capacity decay in NMTP, NMPP, and NMCP materials was studied by the RRDE technique. Besides the simplicity of the RRDE method, it has three major advantages: (i) the soluble degradation products are quickly swept away from the working electrode by forced convection, hence preventing any further interactions, such as re-deposition; (ii) these products can be oxidized/reduced on a polarized ring acting as a detector, which may yield soluble or solid species with insignificant time delay; (iii) the measured ring current could be used for quantitative coulometric analysis and provide important insights into the reaction mechanism. However, when using quantitative data, care must be taken, as surface changes for both, disc and ring, are inevitable in the process, which may lead to a shift in collection efficiency. RRDE technique allows us to detect aqueous Mn species on an appropriately polarized ring where they can be oxidized to yield solid Mn oxide deposits. MnO_2 deposition from $Mn^{(II)}$ solutions on Pt substrate is a relatively well-studied process and can be used to detect aqueous Mn species resulting from the electrochemical degradation of Mn-based phosphate framework electrode materials.

In RRDE setup 20 CV scans were performed on the working electrodes. The obtained voltammograms presented in Fig. 12 are very different from those obtained in beaker-type bottom-mount cells. First of all, the current peaks seem to decrease even faster than in Fig. 9. This is likely due to the differences in electrode preparation used in the two setups. The RRDE working electrodes were drop-cast on a glassy carbon disc resulting in a much higher porosity and weaker adhesion, whereas conventional electrodes were pressed on a mesh, yielding less porous material. Nevertheless, an even more important feature observed in the RRDE cyclic voltammograms is a clear absence of new peaks after prolonged cycling. This further confirms that the electrochemical activity of NMTP and probably many other Mn-based phosphate materials observed is due to the electrochemical activity of decomposition products formed during cycling. Whereas in forced convection experiments these products are washed away from the working electrode into a large volume of electrolyte solution. In this study, an initial assumption is made that the primary cause of degradation in these materials is Mn dissolution from the electrode active material.

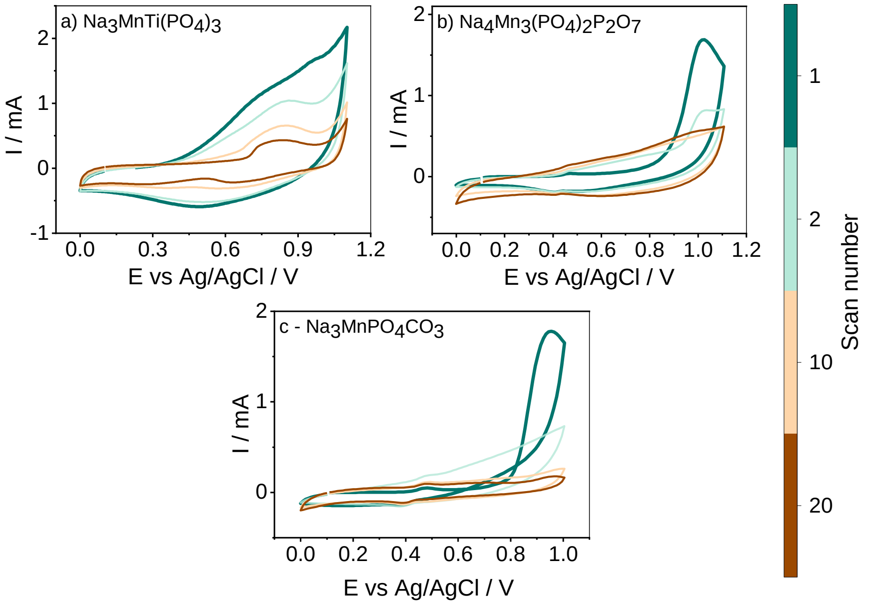

Figure 12. Cyclic voltammograms of a) NMTP, b) NMPP and c) NMPC electrodes recorded in RRDE setup in 1 M Na_2SO_4 at 10 mV s^{-1} and 1200 RPM

To get a better idea about the oxidation reaction and its products, a few additional experiments were carried out. Initially, to study the deposition of MnO_x on the Pt ring during typical RRDE experiments, EQCM was employed. Pt-covered quartz crystal was used as a working electrode. The MnO_x deposition was carried out from the solution containing 0.1 M $MnSO_4$ (0.9 M Na_2SO_4 was used as a background electrolyte to mimic the ionic composition of standard electrolyte) under potentiostatic mode, at 1.2 V vs Ag/AgCl (same as ring potential in RRDE experiments). The mass of the formed oxides was monitored by EQCM and the deposits were analyzed by XPS. The results, presented in Fig. 13 show the variation of electrode mass during the deposition process, as well as the theoretically calculated dependencies for the cases of formation of either pure MnO_2 or MnOOH.

Interestingly, the initially deposited material was closer to MnO_2 and as the experiment persisted, drifted away from $Mn^{(IV)}$. This suggests that on the clean Pt surface, at 1.2 V, MnO_2 deposition is favorable. However, as the oxide accumulates, further deposited products have Mn in lower oxidation state. XPS, which is mostly a surface analysis technique, showed the composition of $MnO_{1.7}$, confirming this idea (Fig. 13 b)). These results suggest that in a typical RRDE experiment, with limited $Mn^{(II)}$ in the electrolyte, the deposited oxide is indeed MnO_2.

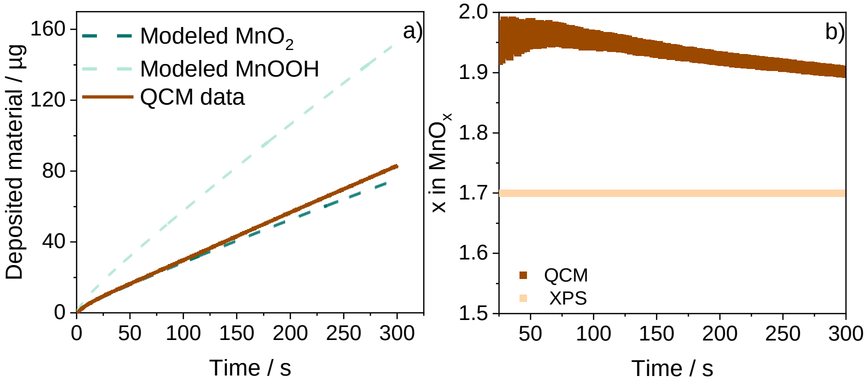

Figure 13. a) Variation of the EQCM sensor mass during deposition of MnO_x from the electrolyte containing 0.1 M $MnSO_4$ and 1 M Na_2SO_4 at 1.2 V vs Ag/AgCl; b) Mn oxidation state estimated from the EQCM data and *post-mortem* XPS analysis

In order to gain an initial understanding of the processes taking place on both, ring and disc, during the RRDE experiment with the phosphate materials, another supplementary experiment was carried out. MnO_2 was potentiostatically electrodeposited on the glassy carbon disc of the RRDE, from the $MnSO_4$ + Na_2SO_4(aq.) solution. Afterward, CV scans were performed across the full electrochemical stability window of the electrolyte (-1 V to 1 V vs Ag/AgCl). The aim of the experiment was to study the relationship between disc and ring reactions by electrochemically dissolving MnO_2 from the disc and subsequently depositing (detecting) it on the ring. The results are presented on Fig. 14.

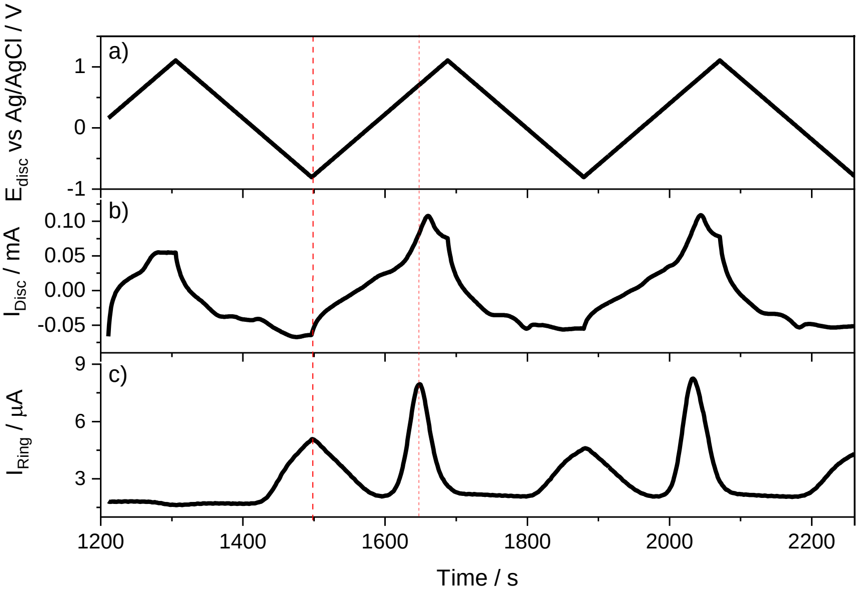

Figure 14. Cyclic votammetry of MnO_2 in RRDE set-up, recorded at 10 mV s^{-1} in 1M Na_2SO_4.The figure shows: a) applied disc potential (E_{disc}), b) disc current (I_{disc}) and c) ring current (I_{ring}). E_{ring} = 1.2V vs Ag/AgCl, rotation rate 1200 |RPM. Dashed vertical lines are guidelines for an eye, marking ring current peaks.

In Fig 14, two distinct ring peaks during the cycling in the whole potential range are visible. The first peak, occurring during the cathodic scan, coincides with the cathodic peak on the disc. It is most likely due to the chemical dissolution of generated $Mn^{(II)}$ during the reduction of the material. The second, higher, and sharper peak is detected on the ring during the oxidation, right before the offset of anodic peak on the disc. Interestingly, it is absent during the first cycle and only appears afterward. Due to this feature, the peak can be attributed to the disproportionation of $Mn^{(III)}$ which is not present in the starting material and is only generated after a first cathodic scan. The process can be accelerated at high potential due to additional proton insertion in the material. Therefore, the dissolution of MnO_2 during electrochemical cycling is a two-step process: (i) during the negative scan water-soluble $Mn^{(II)}$ is generated, which can dissolve and be detected on the ring, and (ii) during the oxidation, proton insertion can accelerate the disproportionation of Mn^{3+}. The second step is absent in the first cycle making the explanation more plausible.

After studying the relationship between disc and ring reactions with MnO_2 as active material, as well as examining dissolution product deposition on the polarized Pt with EQCM, manganese phosphates were analyzed by RRDE method. The complete set of results for the three studied materials is presented in Fig. 15. It is important to note here that no Mn dissolution or other degradation processes were observed in these materials by elemental analysis or RRDE i.e. no current was detected on the polarized ring without applying a current/potential on the disc. Similarly, no Mn dissolution was observed when the electrode was exposed to the electrolyte by immersion for up to a week, confirming to the chemical stability of initial materials in aqueous electrolytes.

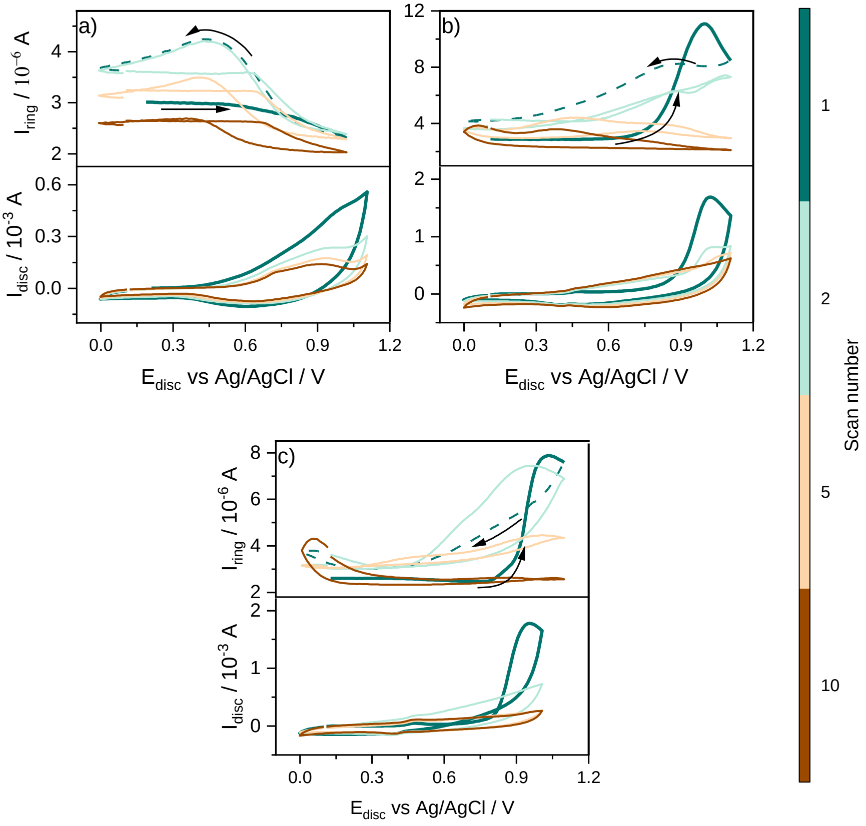

Figure 15. RRDE results for a) NMPP, b) NMCP and c) NMTP. The measurements were carried out at 5mV s^{-1} in 1M Na_2SO_4 electrolyte. E_{ring} = 1.2V vs Ag/AgCl, rotation rate 1200 RPM. Arrows on the ring current curves indicate scan direction.

The current peaks for NMPP and NMCP exhibit a rapid decrease, implying irreversible electrochemical degradation of these materials within the initial cycles. The drop is substantial after just one scan. For NMPP, the disc and ring currents appear to be interconnected: a high positive current on the disc corresponds to a current surge on the ring (Fig. 15 b)). This implies the electrochemically-driven nature of the degradation, more specifically, oxidation of $Mn^{(II)}$ to $Mn^{(III)}$ and the desodiation during charging leading to the loss of Mn and rapid decline in capacity. This might be attributed to the formation of $Mn^{(III)}$, which triggers Jahn-Teller distortion and structural instability. This could lead to the dissolution of structural $Mn^{(II)}$ or the disproportionation of $Mn^{(III)}$ to form highly soluble $Mn^{(II)}$. In the case of NMCP, most of the ring current was observed during charging, when $Mn^{(II)}$ was oxidized to $Mn^{(III)}$ (Fig. 15 c)). Interestingly, in this scenario, two current peaks were evident. The first peak occurred at the initial potential vertex, suggesting a mechanism akin to that observed in NMPP. These ring current peaks are reminiscent of one observed for MnO_2 and can be attributed to the formation of $Mn^{(III)}$, and further disproportionation at high potentials due to H^+/Na^+ extraction. However, for NMCP, a second ring current peak appeared at the reverse potential vertex. The origin of this phenomenon is uncertain, but it could be linked to the potential chemical dissolution of formed $Mn^{(II)}$ due to morphological changes. NMCP powder lacked an intentional carbon coating, and the electrode slurry was prepared through mechanical mixing of the active material with conductive carbon additives, yielding morphologically distinct electrode composites, potentially more prone to chemical active material leaching.

The results for the NMTP electrode exhibit notable differences right from an initial observation (Fig. 15 a)). Firstly, there is an absence of observable Mn dissolution during the charging phase of the electrode, evidenced by a decline in ring current at the first potential vertex. In fact, the ring current reaches its lowest point (background level) at the peak of the charging process. Yet, as the potential is reversed and manganese is reduced back to the more water-soluble $Mn^{(II)}$, an increase in current emerges on the ring simultaneously with the cathodic peak on the disc. This current gradually diminishes towards the beginning of the subsequent anodic scan. Furthermore, the absolute disc and ring current peaks in NMTP are notably lower than those in NMPP or NMCP. This implies that both electrochemical activity and manganese dissolution are inferior in NMTP compared to NMPP and NMCP. This difference could be linked to the suppression of Jahn-Teller distortion owing to Mn substitution by Ti, an intervention that stabilizes

$Mn^{(III)}$ and inhibits the disproportionation reaction to some extent. Unfortunately, this stabilization also seems to impede the overall electrochemical accessibility of manganese in the material.

Even though the investigated processes lack strict hydrodynamic control due to uneven surfaces and their alterations, a certain level of quantitative analysis was performed based on capacity loss and detected manganese. This approach can provide valuable insights into the active material operation and degradation mechanisms in these systems. The working electrode electrochemical degradation was estimated by the charge capacity difference (loss) (ΔQ_{disk}) between two consecutive CV cycles. The cathodic reaction was selected in all cases in order to avoid potential interference due to the onset of OER, which could be a variable contributor to the anodic sweep total charge. The amount of electrodeposited Mn was estimated by integrating the peaks of ring current over time (Q_{ring}).

By examining the integral charges consumed on both disc and ring electrodes, one can derive significant information. Specifically, the cumulative charge on the ring can be directly employed to quantify dissolved manganese throughout electrochemical cycling, while the capacity loss on the disc can act as an indicator for the overall electrochemical degradation of manganese-based phosphates.

For NMCP and NMPP, most of the manganese dissolution occurs during the initial cycles and potentially accompanies swift surface changes on both the disc and the ring. This situation might introduce more uncertainty and potential inconsistencies in the quantitative estimations. On the other hand, the Mn dissolution in NMTP appears to be more gradual. Through quantitative analysis of the ring charge, adjusted for collection efficiency and based on the assumption of a two-electron oxidation process, it appears that only a small fraction of the initial total manganese in the active material (5.46% for NMTP, 4.98% for NMCP, and 4.29% for NMPP) was electrodeposited on the ring after 20 RRDE CV scans. This strongly suggests that only a small fraction of manganese dissolves in the electrolyte during electrochemical operation, while the majority likely becomes either electrochemically inactive or inaccessible.

This interpretation is further supported by the SEM/EDX mapping of NMTP on the disk electrode before and after the RRDE experiment. The results presented in Fig. 16 illustrate this. The images reveal a smooth and uniform working electrode disc and a clean Pt ring prior to the experiment (Fig. 16 a)). However, after the electrochemical cycling, visible cracks appear on the disc, and dark deposits form on the Pt ring. The EDX elemental mapping demonstrates that only Na and Mn were additionally detected on the ring post-cycling, which reinforces the notion that manganese oxides are the most probable electrooxidation products in aqueous electrolytes. Nonetheless, the initial Mn/Ti ratio on the disc electrode, which is nearly 1 before cycling, diminishes to roughly 0.7 after the RRDE experiment. This implies that while some manganese leaching does occur, a substantial amount of it remains in the electrode, yet in an electrochemically inactive or inaccessible state.

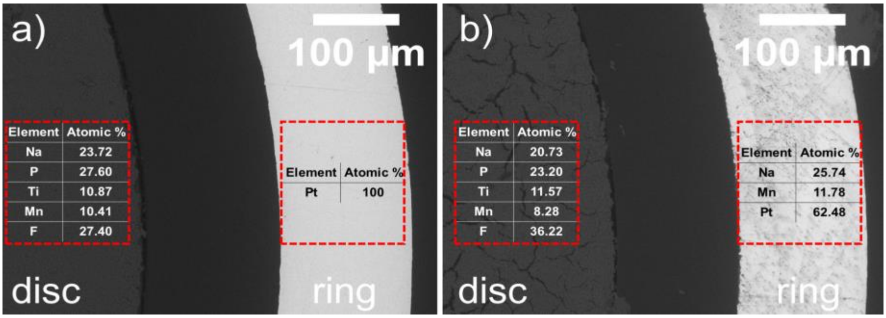

Figure 16. SEM micrographs of RRDE setup with NMTP (a) before and (b) after cyclic voltammetry experiment. The results of elemental analysis are shown as red-bordered areas with areal elemental composition summarized in inset tables.

In principle, the analysis of charge ratios, specifically the relationship between the charges consumed on the ring and lost on the disc ($Q_{ring}/\Delta Q_{disk}$), could offer insightful information regarding the nature of electrochemical degradation in these materials. This analysis holds the potential to address several key aspects: (i) correlation between capacity loss on the disc and ring currents may provide a direct link between capacity loss and active material leaching, (ii) provide insights into the chemical/electrochemical nature of the dissolution, and (iii) provide the information about electrochemically inactive/inaccessible manganese.

The interpretation of $Q_{ring}/\Delta Q_{disk}$ ratios leads to different scenarios of electrochemical degradation. At first, for the simplest case, one can assume that disc material reaches $Mn^{(IV)}$ at a fully charged state, all the degradation is electrochemical in nature, leading to the dissolution of $Mn^{(II)}$, which then gets electrodeposited as MnO_2 on the ring. Among the studied materials, this can occur for NMTP and NMPP ($Mn^{(IV)}$ in a fully charged state), but not for NMCP ($Mn^{(III)}$ in a fully charged state). In this case, $Q_{ring}/\Delta Q_{disk}$ would be equal to 1. Disproportionation-related dissolution was observed for NMPP, which makes this case inapplicable for the material. When $Q_{ring}/\Delta Q_{disk} > 2$, i.e. when more manganese gets electrodeposited on the ring than the charge lost on the disc, it suggests the existence of chemical dissolution of manganese from the working electrode.

For $Q_{ring}/\Delta Q_{disk} < 2$, several explanations are possible, yet they are difficult to distinguish. Firstly, it could imply that either the disc or ring reactions are one-electron processes. This might mean that either soluble $Mn^{(III)}$ species are being oxidized to $Mn^{(IV)}$ on the ring, or the ring reaction proceeds from $Mn^{(II)}$ to $Mn^{(III)}$ only (i.e. instead of MnO_2, MnOOH gets deposited). Second, a more likely explanation is that some portion of manganese is neither soluble nor electrochemically active or accessible, hence eluding detection on the ring. SEM/EDX results support this idea, as the bulk of the Mn seems to be present on the disc after measurements. Another scenario could involve kinetic limitations in Mn electrooxidation on the Pt ring. While this might play a small role by effectively reducing the collection efficiency, it is unlikely to fully account for the observed data.

The results of the aforementioned calculation, the $Q_{ring}/\Delta Q_{disk}$ ratio, for all studied materials, are presented in Fig. 17. The findings show different trends among the studied materials. Initially, as one can see from the ratios, it is difficult to conduct quantitative analysis for NMPP and NMCP, as the bulk of their degradation occurs rapidly during the few initial cycles, probably due to the disproportionation of $Mn^{(III)}$ during the charging state. In the case of NMPP, the charge ratio consistently remains below one across the entire experiment. This suggests that a substantial amount of manganese becomes electrochemically inactive or inaccessible, rather than being dissolved and detected on the ring. NMCP, exhibits less uniform behavior, with ratios displaying scattered values. This behavior may be attributed to morphological characteristics, as well as vulnerability to rapid degradation within the initial few cycles, rendering the material challenging to be quantitatively characterized with the RRDE technique.

The other two studied materials are more interesting. Firstly, the results for MnO_2 are quite important, as its performance is better understood and the degradation patterns may aid in interpreting the other results. As we can see from the Fig. 17, during the first cycle, $Q_{ring}/\Delta Q_{disk}$ ratio is much lower than the rest of the cycles, as it does not contain dissolution due to disproportionation (since no $Mn^{(III)}$ is present on the disc in the first cycle). Afterward, since the reduced forms of manganese are generated in the material, the ratio more than doubles, suggesting that the bulk of the dissolution is due to the new disproportionation reaction. Initial $Q_{ring}/\Delta Q_{disk} \approx 2$, is also interesting, indicating that the MnO_2 redox on the disc is a one-electron process, and in the absence of disproportionation, all the dissolution is electrochemically driven.

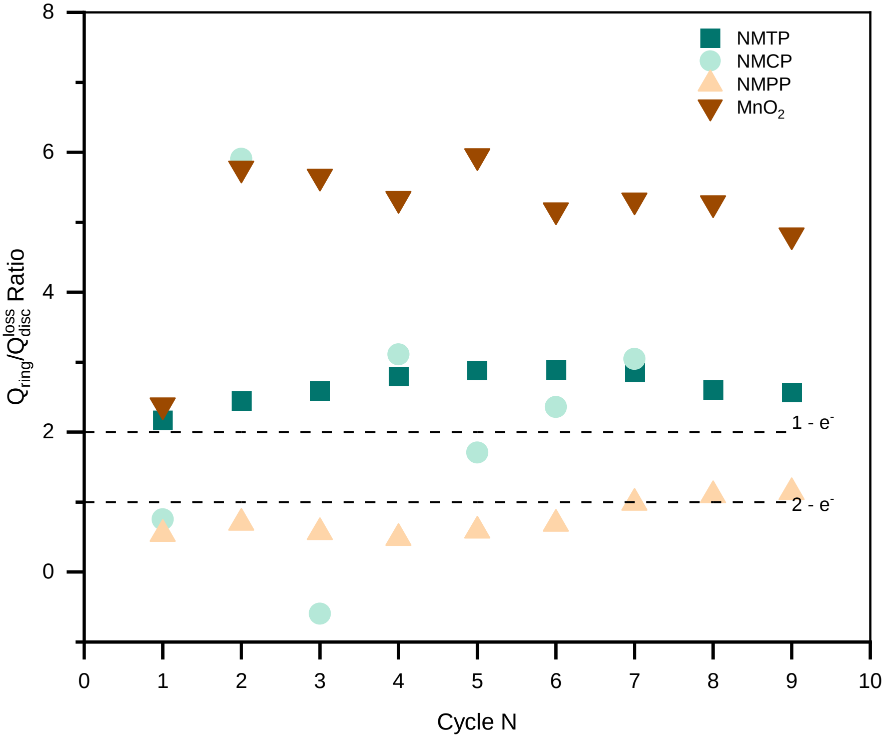

Figure 27. The ratio between integral ring charge and cathodic charge loss for all studied materials. The horizontal guidelines represent the limiting theoretical ratio for one- and two-electron ring oxidation processes, respectively.

NMTP presents another interesting case. It was shown from the prior analysis that the presence of titanium stabilized the lattice by hindering the disproportionation reaction during the charging. As a result, NMTP portrays a consistent charge ratio of around 2 over the span of 10 cycles. This result suggests a dual process: while a significant portion of manganese dissolution is electrochemical, some of it is driven by chemical factors. This chemical dissolution subsequently leads to the inactivity or inaccessibility of portions of the electrode's active material, contributing to the observed capacity degradation.

Overall, the RRDE technique provides unique insights that might be challenging to acquire using standard experimental setups, requiring advanced equipment and cell designs. In agreement with findings from other techniques, the results highlight a commonality across the various Mn-phosphate materials examined: while a significant amount of Mn is leached from the electrodes and is detected on the ring, the bulk of the manganese remains inside the electrode, becoming electrochemically inactive or inaccessible in aqueous electrolytes. This process seems to be the main culprit of the capacity fade. Most of the studied materials leach a significant amount of $Mn^{(II)}$ due to a disproportionation reaction, but the presence of Ti in NMTP seems to suppress this reaction. Despite this, capacity fade is still rapid.

The results here indicate the incompatibility of the studied materials with aqueous media. As a result, the actions, such as protective coatings and electrolyte additives, which are primarily directed to the suppression of the dissolution, are unlikely to be advantageous.

3.3. Aqueous stability of V-based phosphate frameworks as positive electrodes

In this study, the performance and capacity fade of vanadium-based materials were studied. The viability of $Na_3V_2(PO_4)_3$ (NVP) and $Na_3V_2(PO_4)_2F_3$ (NVPF) as aqueous Na-ion battery electrodes were evaluated in standard, 1 M Na_2SO_4(aq.) electrolyte solutions. The preliminary assessment of their electrochemical behavior was done through CV experiments in both unbuffered and citrate-buffered (pH = 4) 1 M Na_2SO_4 (aq.) solutions. This set of experiments provided insights into general conditions such as the appropriate operating potential windows for further analysis. The chemical stability of the material in the aqueous electrolyte was also investigated by a simple immersion test. To qualitatively understand the degree of degradation of the NVP and NVPF electrodes, a double redox titration of the spent electrolytes was carried out. The investigation into electrode degradation is further supplemented by electrode *post mortem* characterization. This involves techniques such as XRD to examine the structural changes, SEM combined with EDX to obtain information about the elemental composition, and inductively coupled plasma optical emission spectrometer (ICP-OES) to assess the extent of active material leaching.

To assess the stability of the materials, the (electro)chemical degradation of NVP and NVPF electrodes was investigated under varying conditions. This included (i) the evaluation of chemical dissolution by electrolyte immersion, (ii) the use of standard electrochemical techniques, such as CV and GCD in a 1 M Na_2SO_4 (aq) electrolyte solution. Due to the substantial quantitative similarity in degradation observed under potentiodynamic and galvanostatic cycling conditions, the latter was excluded from further discussion, mainly due to clarity. Additionally, the RRDE technique is employed for *in situ/operando* analysis of vanadium dissolution during the electrochemical operation of NVP and NVPF. This is carried out in both unbuffered and citrate-buffered (pH = 4) 1 M Na_2SO_4 (aq.) electrolytes, offering a dynamic understanding of the dissolution processes.

To quantitatively assess the extent of vanadium dissolution under various conditions, double redox titrimetry was employed. Additionally, the quantity of undissolved V remaining in the electrode after complete loss of electrochemical activity was evaluated. This analysis was conducted through *post mortem* powder XRD and ICP-OES to analyze solutions obtained after complete dissolution of the remaining active material in 2 M HNO_3. SEM/EDX was also employed as a method to quantify the elements inside the electrode during *post mortem* analysis.

In general, NVP and NVPF owe their electrochemical activity to the reversible $V^{(III)}/V^{(IV)}$ redox accompanied by (de)insertion of sodium (out)/into the phosphate framework structure:

$$\mathrm{Na_3V_2^{(III)}(PO_4)_3 \leftrightarrow NaV_2^{(IV)}(PO_4)_3 + 2Na^+ + 2e^-} \tag{20}$$

$$\mathrm{Na_3V_2^{(III)}(PO_4)_2F_3 \leftrightarrow NaV_2^{(IV)}(PO_4)_2F_3 + 2Na^+ + 2e^-} \tag{21}$$

Earlier research has shown the possibility of an additional insertion of sodium into the crystal structure of NVP/NVPF, resulting in the further reduction of $V^{(III)}$ to $V^{(II)}$. This process is typically observed at relatively low potentials (ca. 1.7 V vs. Na^+/Na or -1.0 V vs. SHE). Furthermore, this operating potential exceeds the stability window of most low-concentration aqueous electrolyte systems, therefore, it will be excluded from further discussion.

Figure 18. Electrolyte immersion test results: from left to right - electrolyte after 120 h immersion of NVPF and after 24, 48 and 120 h immersion of NVP

The extent of both chemical and electrochemically-induced vanadium dissolution within NVP and NVPF electrodes was rigorously examined. To address the degree of vanadium chemical dissolution, electrodes were immersed in 1 M Na_2SO_4 (aq.) solution for 24, 48, and 120 h. After just 24 h, some characteristic yellow coloration appeared in the soaking solution, indicating vanadium dissolution from the NVP electrode (Fig. 18).

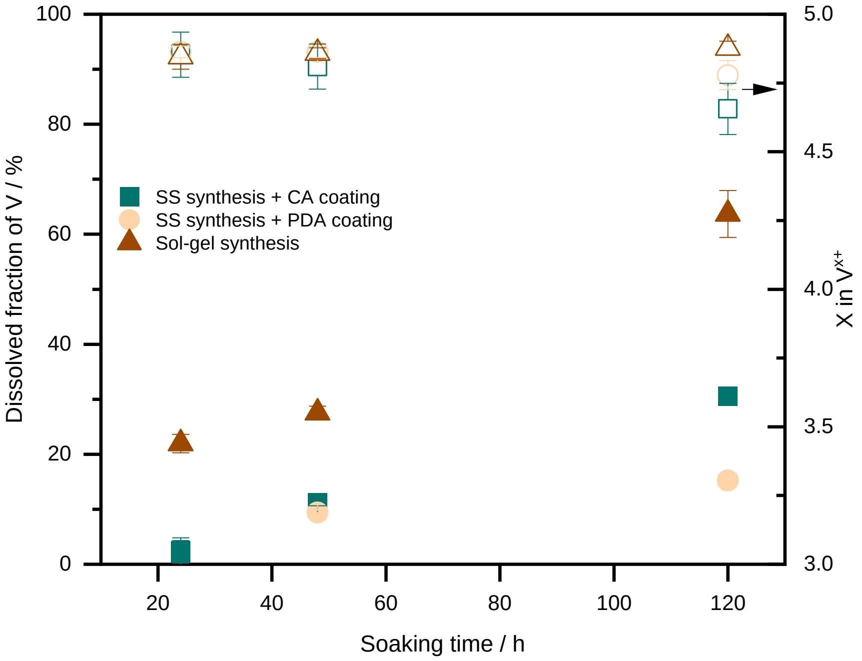

Figure 3. Fraction of dissolved vanadium (solid symbols) and average oxidation state (hollow symbols) measured after an immersion test of NVP electrodes with different synthesis/carbon coatings.

This process was repeated for materials synthesized using different methods. Specifically, solid-state (SS) and sol-gel syntheses were compared. The primary difference between these materials lies in the origin of their carbon coatings. The carbon in the sol-gel product is formed through the pyrolysis of citric acid, utilized during the synthesis process, and formed simultaneously with the crystalline structure of NVP. In the case of solid-state synthesis, carbon is introduced later as an additional step through the pyrolysis of citric acid (CA) after the initial synthesis step. To account for the potential impacts of acidity on the structure, an alternate carbon coating method was explored, utilizing pyrolysis of polydopamine (PDA) which is introduced by the initial processing in slightly basic conditions (pH = 8.5). The results, presented on Fig. 19, show that regardless of the synthesis route or the origin of carbon coating, chemical degradation is an important factor for NVP electrodes. However, carbon coating seems to play some role. PDA-coated materials show more resistance towards active material leaching in aqueous media. However, their instability becomes apparent during longer immersion times. The average oxidation state of dissolved vanadium was also estimated, showing that practically all of the species are in the $V^{(V)}$ state. Interestingly, sol-gel synthesized particles exhibited slightly less stability, potentially attributed to smaller particle size.

Due to the simplicity and reproducibility of the method, the citric acid-coated solid-state synthesized materials were chosen for further investigations. For this material, approximately 2.5%, 12%, and 30% of V is dissolved after 24 h, 48 h, and 120 h, respectively (Fig. 19). This experiment emphasizes the significance of chemical vanadium dissolution as a contributing factor to the overall NVP degradation in low-concentration aqueous electrolytes. The same experiment was conducted for NVPF electrodes. Interestingly, minimal vanadium dissolution was observed even after immersing the NVPF electrode in 1 M Na_2SO_4 (aq.) solution for 120 h (Fig. 18). This result implies that, in contrast to NVP, chemical vanadium dissolution is not an important contributor to NVPF degradation in aqueous electrolytes.

The preliminary characterization involved potentiodynamic cycling in beaker-type bottom-mount cells containing 1 M Na_2SO_4 (aq.) solution. The measurements were carried out under ambient conditions, resulting in a pH ~ 6 in unbuffered electrolytes. Additional experiments were conducted using citrate-buffered (pH = 4) and borate-buffered (pH = 9) electrolytes. The borate-buffered experiments were almost identical to the unbuffered case; therefore, no further characterization was performed in this electrolyte. The results obtained at a potential sweep rate of 5 mV s^{-1} are presented in Fig. 20. In the first CV scan, NVP exhibited a reversible anodic/cathodic peak pair at 0.6/0.4 V vs Ag/AgCl, respectively (Fig. 20 a)). This electrochemical activity rapidly diminished in subsequent cycles. After only 20 CV cycles, a substantial reduction in electrochemical activity is observed. The influence of an acidic environment on aqueous vanadium species stability was assessed through CVs recorded at pH = 4 (Fig. 20 b)). NVP electrochemical activity faded even faster in an acidic electrolyte, implying accelerated vanadium dissolution under such conditions. A similar trend was observed for NVPF. A reversible anodic/cathodic peak pair at 0.85/0.65 V vs Ag/AgCl was noted in the CV (Fig. 20 c)), followed by a gradual decline in recorded currents during subsequent scans. This indicated significant capacity loss for NVPF when cycled in 1 M Na_2SO_4 (aq.). Similar behavior was observed in pH = 4 electrolyte, where NVPF's capacity declined more rapidly than in near-neutral conditions. Notably, additional peaks emerged in the voltammogram during later cycles and at lower potential values, possibly linked to the electrochemical activity of certain dissolved vanadium species on the electrode surface. Electrolyte color in both cases was changed to yellow, characteristic of $V^{(V)}$, suggesting that degradation is dissolution-driven.

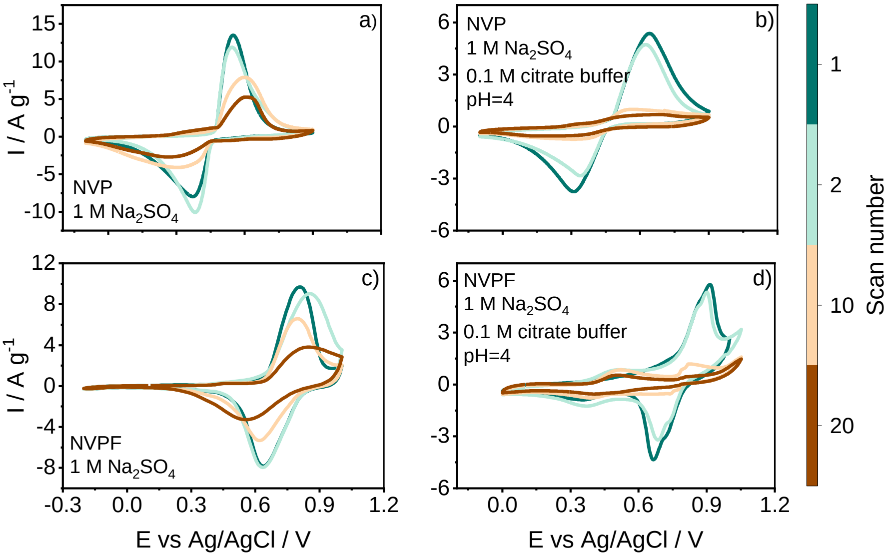

Figure 4. CVs on NVP (a, b) and NVPF (c, d) in unbuffered (a, c) and pH 4 buffered (b, d) 1 M Na_2SO_4 (aq.) electrolytes, 5 mV s^{-1}.

Prior research on other NASICON-structured materials, such as $NaTi_2(PO_4)_3$ or $Na_3MnTi(PO_4)_3$, indicated that the bulk of the capacity fade was driven not by material dissolution, but rather primarily resulted from the loss of contact between active material particles [138]. In line with these findings, this study aims to understand the detailed mechanisms of NVP and NVPF capacity fade in aqueous electrolytes. Thus, vanadium dissolution was quantitatively analyzed using various methods (Fig. 21). Initially, NVP electrodes underwent 200 CV cycles at 5 mV s^{-1} until no obvious vanadium redox-related electrochemical response was detectable. Subsequently, the electrolytes were collected and analyzed by double redox titrimetry, enabling both total vanadium content and average oxidation state determination [137]. The results in Fig. 21 show that a minimum of 66% of the initial vanadium content dissolves from the electrode into the electrolyte during cycling. Vanadium species in the electrolyte showed an average oxidation state of 4.9±0.03, supporting the idea of $V^{(V)}$ as the dominant species in the aqueous medium. Furthermore, *post mortem* electrode dissolution in 2 M HNO_3 (aq.)

was employed to analyze the residual vanadium. ICP-OES analysis indicated that only 7% of the initial vanadium content remained in the electrodes after 200 CV cycles. These results confirm that the main factor contributing to capacity loss in NVP is the dissolution of vanadium from the NASICON structure into the aqueous electrolyte rather than the processes observed in Mn-based materials.

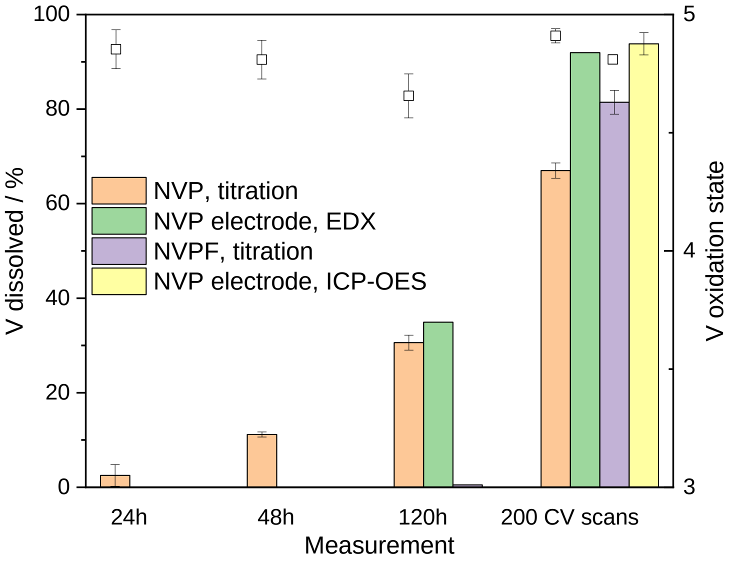

Figure 5. Vanadium loss from the electrodes evaluated by various methods after different (electro)chemical degradation.

An additional experiment was carried out on the NVP electrode to investigate the impact of chemical dissolution on its electrochemical performance. As depicted in Fig. 22, the electrode electrochemical response, as assessed by peak current on the CV, was diminished by over 50% following 24 h of immersion in 1 M Na_2SO_4 (aq.) despite the fact that no color change of the electrolyte was observed.

To assess the extent of degradation in the NASICON phase, NVP electrodes were analyzed using XRD and EDX analyses. To observe the peak changes and quantify the active material, 20 wt% of HfO_2 was blended into the electrode slurry during preparation as an inert internal standard. The XRD patterns and quantitative EDX elemental analyses were conducted on fresh electrodes, electrodes after 200 CV scans, and electrodes immersed in 1 M

Na_2SO_4 (aq.) for 120 hours. The findings in Fig. 23 confirm previous observations. The deterioration of the NVP phase is pronounced even in the absence of electrochemical cycling. A significant reduction in distinctive NVP peaks in the XRD pattern (Fig. 23) and a decrease in the Hf:V ratio from 2.52 to 1.67 in the EDX elemental analysis, after 120h electrolyte immersion is also observed. After 200 CV cycles, the NVP phase becomes virtually undetectable, with no discernible NASICON peaks in the XRD pattern and only an insignificant quantity of vanadium detectable via EDX.

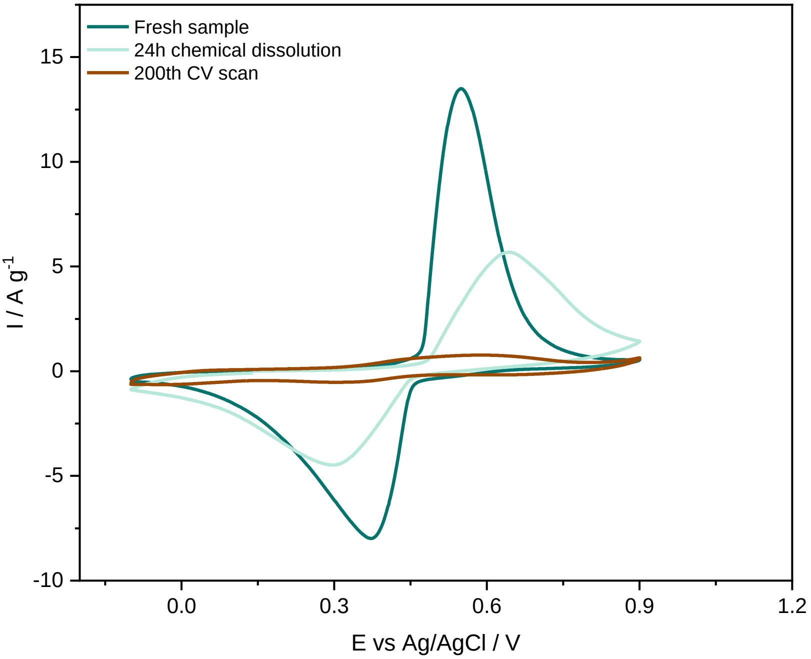

Figure 6. Cyclic voltammograms of of fresh NVP electrode and after chemical and electrochemical treatements recorded in 1M Na_2SO_4 electrolyte at 10 mV s^{-1} .

NVPF material seems to be more resilient. XRD measurements of the electrodes, as well as electrolyte titrations, show that the material is practically intact after 120 h of electrolyte immersion. Even after 200 CV scans, XRD peaks, corresponding to the NASICON structure are preserved (Fig. 23).

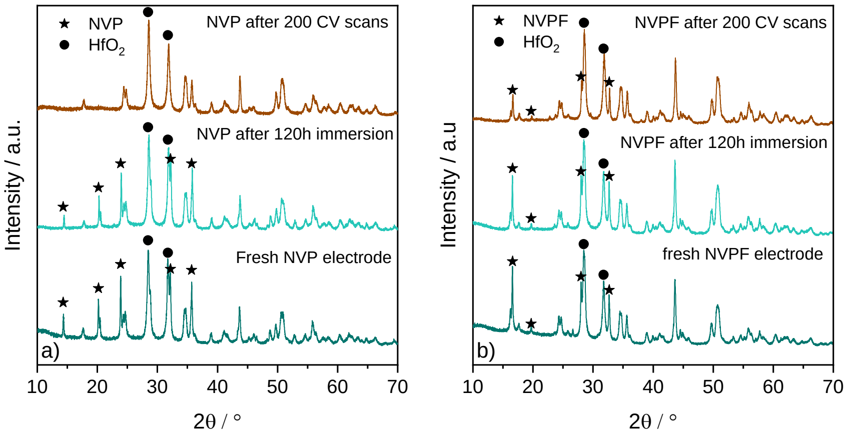

Figure 7. Evaluation of the degradation of the crystalline phase of a) NVP and b) NVPF with XRD after chemical and electrochemical treatments.

For the RRDE experiments, one important parameter is the working potential window, which was estimated by CV, carried out in conventional beaker-type cells. Another consideration is the selection of the appropriate ring potentials, which could impact the detection of dissolved V species. At first, it might sound convenient to choose the highest or lowest potential possible. However, the background current on the ring must be kept in mind, which typically increases as the applied potential approaches the edges of the electrolyte stability window interfering with the measurement. The background noise becomes even more apparent when varying the electrolyte composition and pH.

To address this, a series of CVs were initially conducted using a Pt ring electrode as a working electrode. This was performed in three types of electrolytes: (i) fresh unbuffered (1 M Na_2SO_4, pH~6), (ii) citrate buffered (pH = 4), and (iii) unbuffered, spent 1 M Na_2SO_4 (aq.) electrolyte, collected after the full degradation of NVPF in beaker-type cell. The results are presented in Fig. 24, indicating that in the standard electrolyte (fresh, unbuffered), minimal background interference occurs between -0.7 V and 1.2 V vs Ag/AgCl. Beyond these values, hydrogen and oxygen evolution reactions become pronounced, respectively. It is anticipated that manipulating pH, should impact these potentials, especially at the lower end (for hydrogen evolution reaction), since the reaction is more prominent on Pt surface. Indeed, when the pH is lowered to 4, the onset potential of HER shifts to -0.4 V vs Ag/AgCl, while the OER potential remains relatively stable. This considerably narrows the operational electrochemical window in the pH 4 buffered electrolytes.

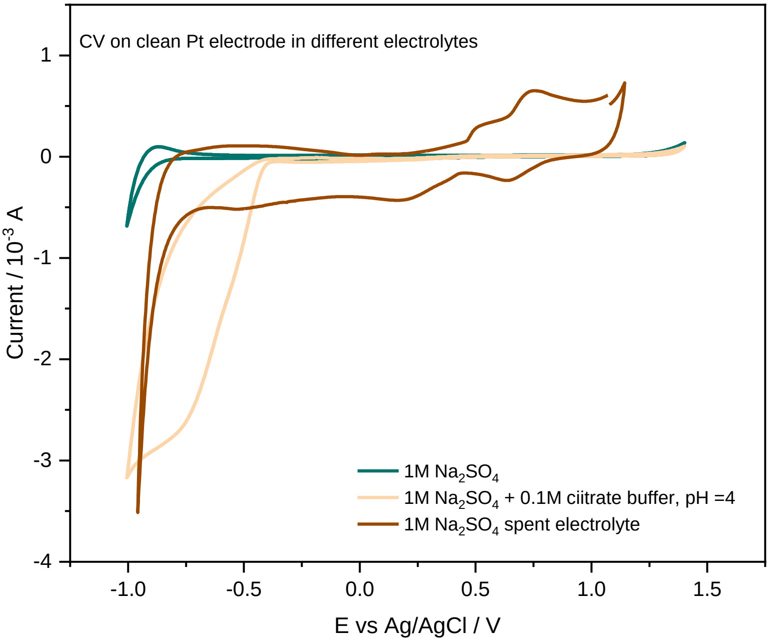

Figure 8. Cyclic voltammograms of Pt ring electrode recorded in fresh unbuffered, citrate buffered (pH = 4) and spent vanadium containing electrolyte at 5 mV s^{-1}.

In the case of the already spent, V-containing electrolyte, certain electrochemical activity is evident. Multiple discernible peaks emerge in the entire potential range from -0.7 V to 1.1 V vs Ag/AgCl. Notably, the region between 0.5 V and 1 V is particularly interesting, as it is anticipated to involve distinct redox reactions involving V$^{(III)}$, V$^{(IV)}$, and V$^{(V)}$ species. The presence of these multiple peaks suggests the likelihood of different vanadium species participating in various redox reactions within such a system. Throughout this study, the assumption is made that in neutral pH and the selected potentials, V$^{(V)}$ is dominant. This assumption is based on the Pourbaix diagram displayed in Fig. 3, as well as double redox titration results.

It is also worth noting, that during the normal operation of materials (Reaction 20 and 21), no V$^{(V)}$ generation is expected, however, it can either be generated intrinsically in the active material during charging due to possible disproportionation in the fully charged state:

$$\mathrm{NaV^{(IV)}V^{(IV)}(PO_4)_3 \leftrightarrow NaV^{(III)}V^{(V)}(PO_4)_3} \qquad (22)$$

$$\mathrm{NaV^{(IV)}V^{(IV)}(PO_4)_2\,F_3 \leftrightarrow NaV^{(III)}V^{(V)}(PO_4)_2\,F_3} \quad (23)$$

or extrinsically out of the electrode active material due to oxidation of lower oxidation species in an aqueous environment through oxygen exposure or on the surface of a working electrode at high potential.

$V^{(V)}$ can be detected on the sufficiently negatively polarized ring of RRDE and, the following reduction reaction to $V^{(III)}$ might be expected according to the Pourbaix diagram:

$$\mathrm{H_2VO_4^- + 2e^- + 5H^+ \rightarrow VOH^{2+} + 3H_2O} \qquad (24)$$

If some $V^{(IV)}$ is also present in the electrolyte, as suggested by our double redox titration results, another reduction reaction might also take place on a ring:

$$\mathrm{VO^{2+} + e^- + H^+ \rightarrow VOH^{2+}} \qquad (25)$$

In the case of a positively polarized ring, $V^{(V)}$ will yield no signal, and it is either $V^{(IV)}$ species which can be oxidized to $V^{(V)}$:

$$\mathrm{VO^{2+} + 3H_2O \rightarrow H_2VO_4^- + 4H^+ + e^-} \qquad (26)$$

or some $V^{(III)}$ species which might be oxidized to $V^{(V)}$ in a two-electron process:

$$\mathrm{VOH^{2+} + 3H_2O \rightarrow H_2VO_4^- + 5H^+ + 2e^-} \qquad (27)$$

To gain deeper insights into the degradation process, including its mechanisms and pH dependence, *in situ/operando* studies were conducted using RRDE. Two sets of experiments were carried out, employing both, potentiodynamic and galvanostatic methods, both in unbuffered and pH 4 buffered 1 M Na_2SO_4 (aq.) electrolytes. The experimental parameters, such as active materials, sweep rate for CV, and current density for GCD, were kept identical for both sets. Additionally, two Pt ring electrode polarization modes were chosen to examine the reduction and oxidation of dissolved vanadium species. The ring was maintained at -0.7 V (or -0.4 V in pH 4) vs Ag/AgCl to investigate the former process and at 1.2 V vs Ag/AgCl to explore the latter. In all experiments, the ring current was stabilized for 30 minutes by polarizing it to the desired potential before disc reactions. The background ring current ranged between 1 and 5 µA for most samples, depending on polarization, with higher background currents observed for negatively polarized conditions. The results in Fig. 25 display disc voltammograms and ring chronoamperograms. The information gathered from the CVs is in agreement with results obtained from conventional cell setups. Both materials show a substantial drop in peak currents with cycling. Notably, the degradation of NVP appears to be faster in the RRDE experiment compared to the conventional setup. This could be attributed to the greater porosity of the drop-casted electrode due to the absence of prior pressing. This leads to an increased surface area and enhanced electrolyte accessibility. Additionally, the forced convection in the RRDE setup might accelerate the removal of dissolved vanadium species, thereby potentially accelerating the dissolution rate as well.

In the case of negative ring polarization, the current dramatically increases at the onset of the initial anodic disc CV wave. While the anodic peak potential on the disc reaches 0.6 V vs Ag/AgCl, the current peak on the ring emerges slightly later, around 0.75 V vs Ag/AgCl. This is followed by a declining current, although it remains elevated compared to the background throughout the scan. A minor increase is observed near the upper potential vertex (1 V vs Ag/AgCl), however, this can possibly be attributed to the overall rise in an oxidative environment close to the OER, rather than additional dissolution products. As the potential is reversed, the current values drop and continue to decrease throughout the entire scan, essentially reaching zero (compared to the background) at the end of the cathodic sweep (0 V vs Ag/AgCl). The second scan exhibits similar features but with a significantly lower current magnitude. This behavior definitively indicates the generation of oxidized vanadium species ($V^{(IV)}$ or $V^{(V)}$) as soon as a sufficiently high potential is applied to the disc, driving the typical NVP charging reaction, and persisting throughout the whole charging process. The generation of oxidized species does not require very high potential values, indicating that they form even during normal charging and not just during overcharging. In contrast, negligible electrochemical activity is detected on the ring during discharging.

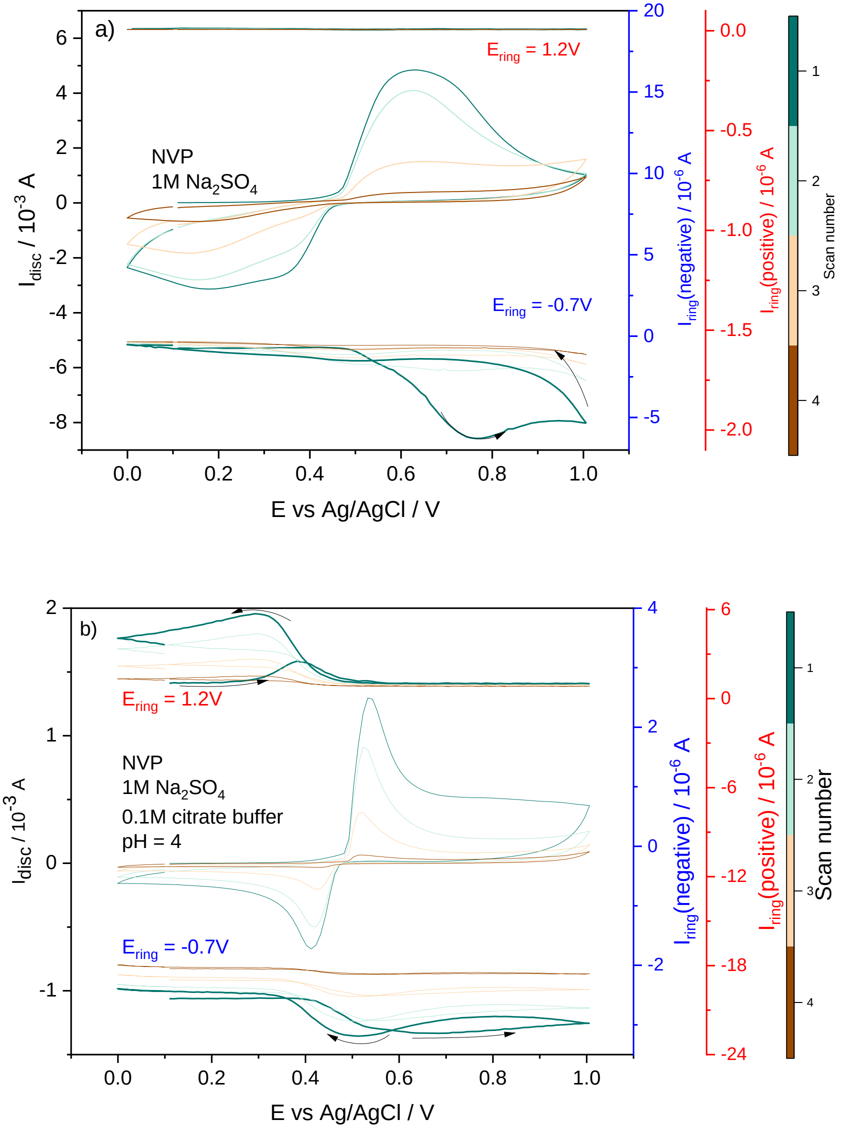

Figure 9. CV measurements with RRDE set-up for NVP, recorded in a) unbuffered and b) buffered (pH =4) 1M Na_2SO_4 (aq.) electrolytes at 5 mV s^{-1}. The curves in the middle are cyclic voltammograms (disc currents, or I_{disc}, left y-axis), together with chronoamperograms of both, negatively (bottom) and positively (top) polarized Pt rings (I_{ring}, right y-axes).

Identical experiments with a positively polarized ring were also conducted to detect the presence of $V^{(IV)}$ and $V^{(III)}$ species. The results in Fig. 25 illustrate that the recorded current values on the positive ring are almost two orders of magnitude lower compared to those on a negatively polarized ring. This suggests a minimal presence of lower oxidation state vanadium species, as the detected current is nearly negligible compared to the negative ring. This implies that there is practically no $V^{(IV)}$ and all the electrochemical activity observed on the negatively charged ring can be attributed to $V^{(V)}$. This observation aligns well with double redox titration results of the spent electrolyte, indicating the average oxidation state of vanadium to be primarily $V^{(V)}$ in most cases.

The same materials were also studied in a pH 4 buffered electrolyte to assess material stability and gather insights into the behavior of dissolved species in the media. In this measurement, similar trends in disc CV and negatively polarized ring current are observed as in the unbuffered case (Fig. 25 b)). Notably, the recorded disc currents are reduced by about 50% compared to neutral electrolytes. This drop, which is consistent with conventional CV experiments, can be attributed to accelerated chemical dissolution in an acidic electrolyte, leading to diminished overall electrochemical activity. The decline in activity after the first scan is more pronounced as well, and both samples exhibit negligible activity after 10 scans. Elevated background currents of the ring electrode also appear (-25 μA vs -5 μA for pH 4 and neutral electrolytes respectively), however, this is likely due to the presence of a low pH buffer, rather than continuous chemical dissolution of the material. Although peak potentials remain the same, peaks are sharper with lower currents. The shape of the material CVs, ring currents, and their relationship differ from those in the neutral electrolyte.

A noteworthy observation is an increase in negative ring current at ca. 0.4 V vs Ag/AgCl (about 0.1 V earlier than in neutral electrolyte), which occurs just before the onset of the anodic peak on the disk at 0.5 V (Fig 25 b)). This suggests the reduction of chemically dissolved V species. Simultaneously, a peak (~3 μA) also appears on the positively polarized ring. This implies that chemically dissolved V undergoes oxidation on the Pt ring electrode as well. Since only $V^{(IV)}$ can be both reduced and oxidized on negatively and positively polarized ring electrodes respectively, it suggests that the chemical dissolution of NVP at pH 4 generates aqueous $V^{(IV)}$ species. This aligns well with the Pourbaix diagram. While the process is not entirely chemical in nature, as no ring activity is observed without applying any potential (or before the disc reaches 0.4V), it is worth noting that the generation of $V^{(IV)}$ occurs prior to the oxidation process on the disc electrode.

The shape of the negatively polarized ring amperogram in a pH 4 buffered electrolyte significantly differs from the unbuffered case as well. During the anodic scan, the current initially increases, similar to the neutral medium. However, instead of returning to zero after scan direction reversal, it slightly decreases within the range of 1 V – 0.7 V vs Ag/AgCl, then starts to increase again, reaching the peak value around the onset of the disc cathodic wave. This suggests the generation of either new $V^{(V)}$ species or the production of $V^{(IV)}$ during the cathodic scan.

The possibility of $V^{(V)}$ generation during the cathodic sweep seems improbable, despite the potential being suitable for these species (as seen in the Pourbaix diagram). This can be confirmed by observing the behavior of the positively polarized ring current. Unlike the negative currents, the positive currents remain close to the baseline during the anodic sweep (i.e. no products are being oxidized), except for the first cycle where a small peak around 0.4 V is observed, likely due to synthesis impurities. However, these positive currents start systematically increasing at the onset of the cathodic disc CV wave. Positive I_{ring} reaches its peak around the cathodic peak potential (0.45 V vs Ag/AgCl), remains elevated afterward, and then gradually decreases towards the end of the cathodic sweep (0 V vs Ag/AgCl). Altogether, these results strongly suggest that in a pH 4 environment, there is a notable electrochemically-induced generation of soluble $V^{(IV)}$ species, which are subsequently oxidized according to Reaction 25 on the ring electrode.

The results of RRDE experiments for NVPF (Fig. 26) exhibit similar trends to those discussed in the case of NVP. Peak currents in cyclic voltammograms fade at a slower rate, and the ring current for these measurements is considerably smaller. In the unbuffered electrolyte (Fig 26 a)), the negatively polarized ring currents are about half as in the case of NVP. This suggests that NVPF is generally more stable in aqueous electrolytes compared to NVP. The negative I_{ring} shows an exponential increase at the onset of an anodic disc wave and starts decreasing once the potential sweep direction is reversed. Positively polarized ring currents are about an order of magnitude lower than negative ones, implying that in a near-neutral electrolyte, only $V^{(V)}$ is generated during the electrochemical cycling of NVPF. However, the shape of this negative ring current differs from that observed for NVP (exponential increase but no peak is evident). It seems more likely that the bulk of this increase is due to an overall heightened oxidative environment on the disc, rather than the generation of electrochemically active vanadium species.

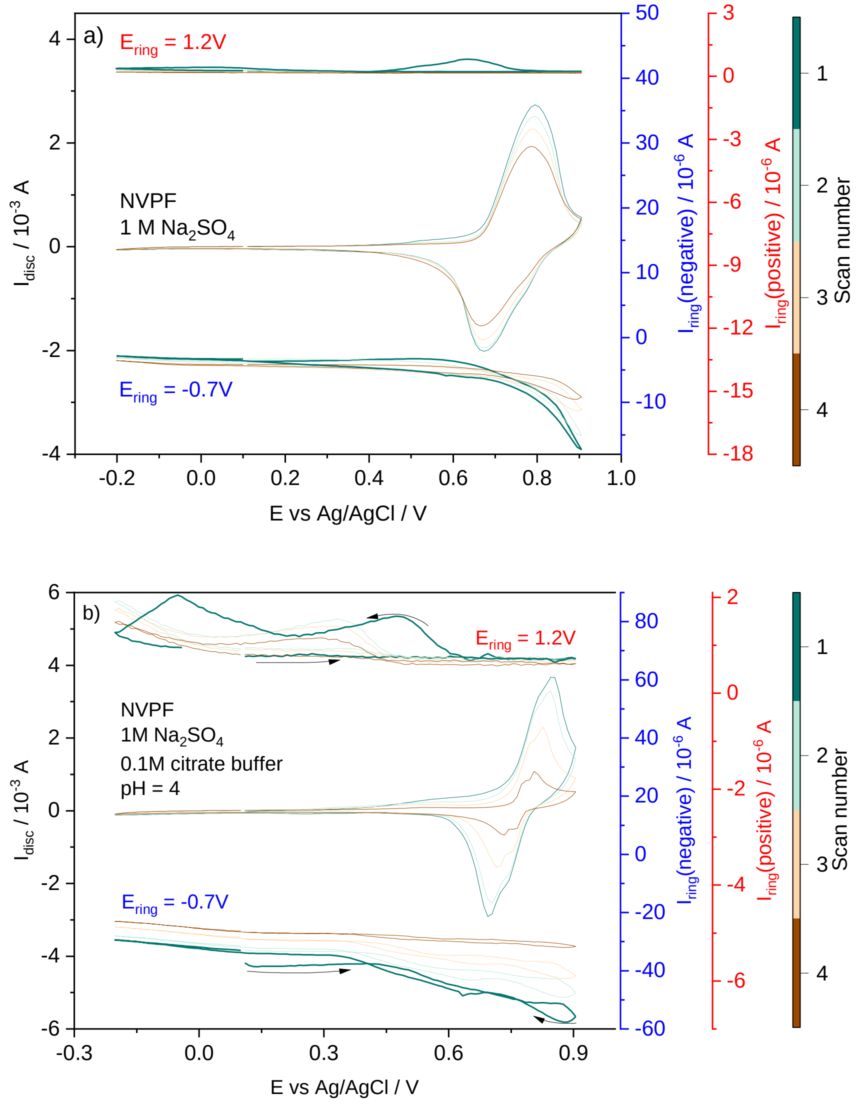

Figure 10. CV measurements with RRDE set-up for NVPF recorded in a) unbuffered and b) buffered electrolytes at 5 mV s^{-1}. The curves in the middle are cyclic voltammograms (disc currents, or I_{disc}, left y-axis), together with chronoamperograms of both, negatively (bottom) and positively (top) polarized Pt rings (I_{ring}, right y-axes)

In the pH 4 buffered electrolyte (Fig. 26 b)), the initial background current on the negatively polarized ring is nearly ten times larger than that in the unbuffered 1 M Na_2SO_4 (aq.), i.e. -37 µA compared to -4 µA . This difference, again, can be attributed to the same factors discussed earlier for the NVP sample, as there is no influence from the disc or the materials applied to it yet. The negative I_{ring} starts to increase well the onset of anodic current on the disk before (around 0.3 V, while the oxidation peak onset is at ~0.7 V), and it tends to stabilize slightly at E_{disk} ~ 0.7 V vs Ag/AgCl. As observed in previous samples, this could be due to the reduction of chemically dissolved vanadium.

In the E_{disk} range of NVPF's anodic peak (above 0.7 V vs Ag/AgCl), the negative I_{ring} starts increasing again and remains elevated even after the reversal of the potential scan. This suggests the electrochemically-induced generation of soluble V species, which persists after the scan direction is reversed. The current starts decreasing, however remains relatively elevated after the reversal of the scan. On the positively polarized ring, the current values are again about five times higher compared to those in the neutral unbuffered electrolyte (Fig. 26). The behavior of the current is also drastically different from that in the unbuffered neutral media, as two peaks can be observed during the cathodic sweep. Interestingly, in the pH 4 buffered 1 M Na_2SO_4 (aq.), positive I_{ring} peak positions are outside the range of NVPF redox processes, i.e. they are shifted to more negative disc potentials, where no electrochemical activity of NVPF is observed (Fig. 25). One possible explanation could be the destabilization of the lattice during the charge and slightly stronger chemical dissolution during NVPF discharge, resulting in the leaching of more soluble $V^{(III)}$ and $V^{(IV)}$ species.

To avoid any kinetic limitations that could arise due to relatively faster redox processes caused by a fixed potential sweep rate, a set of identical RRDE experiments were conducted in a galvanostatic mode on both NVP and NVPF materials cast on the disc electrode. Specific currents of 0.59 A g^{-1} and 0.640 A g^{-1}, corresponding to a rate of 5C, were utilized for NVP and NVPF, respectively. This high charge/discharge rate was selected due to the time-limited nature of the experiment and was found to be optimal for this case. Apart from the potential chemical instability of the materials during prolonged experiments, the high charge/discharge current also aimed to potentially amplify the current detected on the ring, leading to a better signal-to-noise ratio.

Operating potentials of 0.3 - 0.8 V and 0.1 - 0.8 V vs Ag/AgCl were individually chosen based on prior experiments (GCD measurements in conventional setup) for NVP and NVPF, respectively. The upper potential cut-off was carefully controlled due to the possible onset of oxygen evolution that could interfere with the measurement and therefore the current detected on the ring. However, the lower cutoff potential is less significant since there are minimal electrochemically active processes overlapping with our experiments in aqueous electrolytes.

The data presented in Fig. 27 and Fig. 28 in the form of dQ/dE vs E plot reveal two reversible potential peaks, approximately around 0.5 V and 0.7 V vs Ag/AgCl for NVP and NVPF, respectively. The potential plateau in NVP charge/discharge profile is relatively flat, leading to a sharper dQ/dE peak, while for NVPF, the plateau is slightly tilted, yielding a broader peak. Overall, the results demonstrate similar trends as the RRDE experiments in potentiodynamic mode. However, there is higher noise in the ring currents observed in the galvanostatic mode. The ring current waves also appear broader, and although they correspond with the processes occurring on the disc, they seem to lag behind. The currents on the negatively polarized ring increase during the entire charging process but reverse once the discharging starts. However, the decrease during discharging is not as rapid as when CV is performed on the disc electrode.

Nevertheless, the recorded positive ring currents for both NVP (Fig. 26 b)) and NVPF (Fig. 27 d)) exhibit an increase of more than an order of magnitude at pH 4, supporting the earlier finding that lower oxidation state vanadium species are generated only in acidic electrolytes. The observation that negative currents during discharging are high but do not surpass those during charging further confirms the likely presence of $V^{(IV)}$ species during degradation in low pH conditions.

Even though the overall picture is similar, these findings may suggest that the galvanostatic mode might not be as suitable for this type of experiment as the potentiodynamic mode. In the potentiodynamic mode, the primary redox processes within the electrode material are accelerated during the potential scan, leading to significantly higher currents on the disc electrode containing the active material. This faster degradation mainly occurs within a potential range of interest, i.e. in the range where redox reactions occur. However, in the galvanostatic mode, the currents are constant, and the degradation processes proceed at a more consistent rate across the entire potential range of operation.

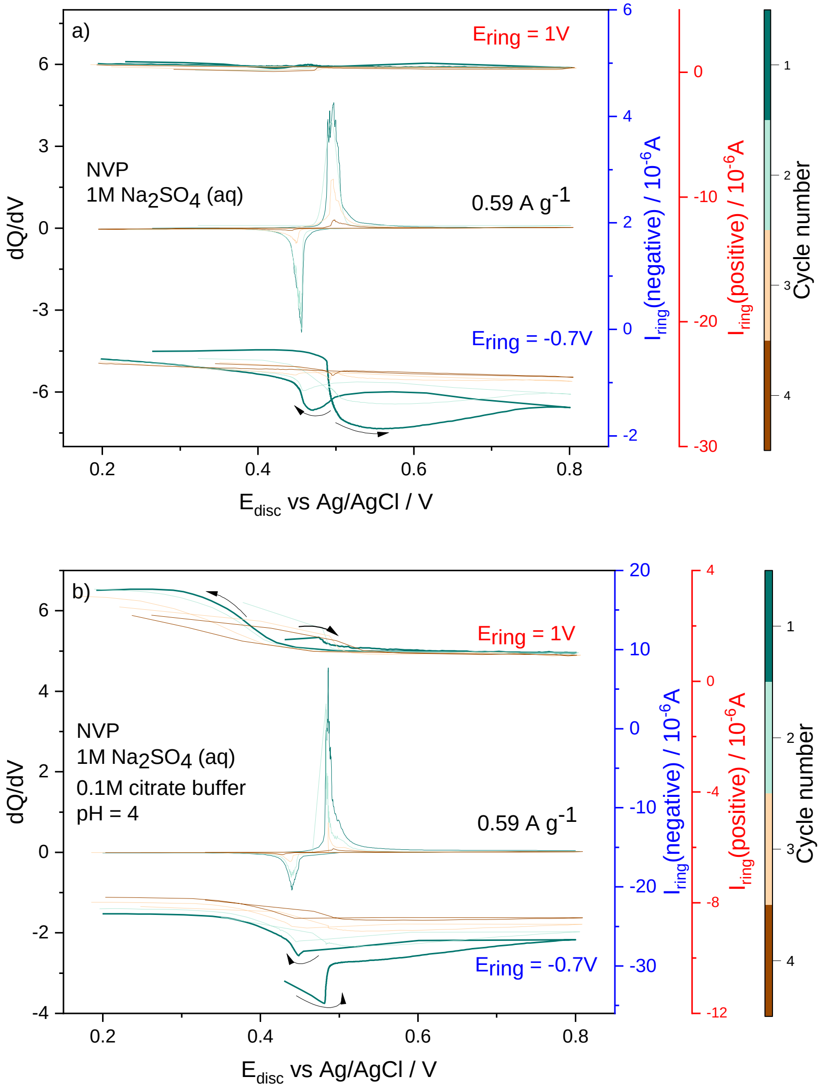

Figure 11. The galvanostatic measurements for NVP on RRDE set-up recorded in a) unbuffered and b) buffered (pH = 4) electrolytes recorded at 5C rate. Data is presented in a form of dQ/dE (middle, left y-axis) together with chronoamperograms of both, negatively (bottom) and positively (top) polarized Pt rings (I_{ring}, right y-axes).

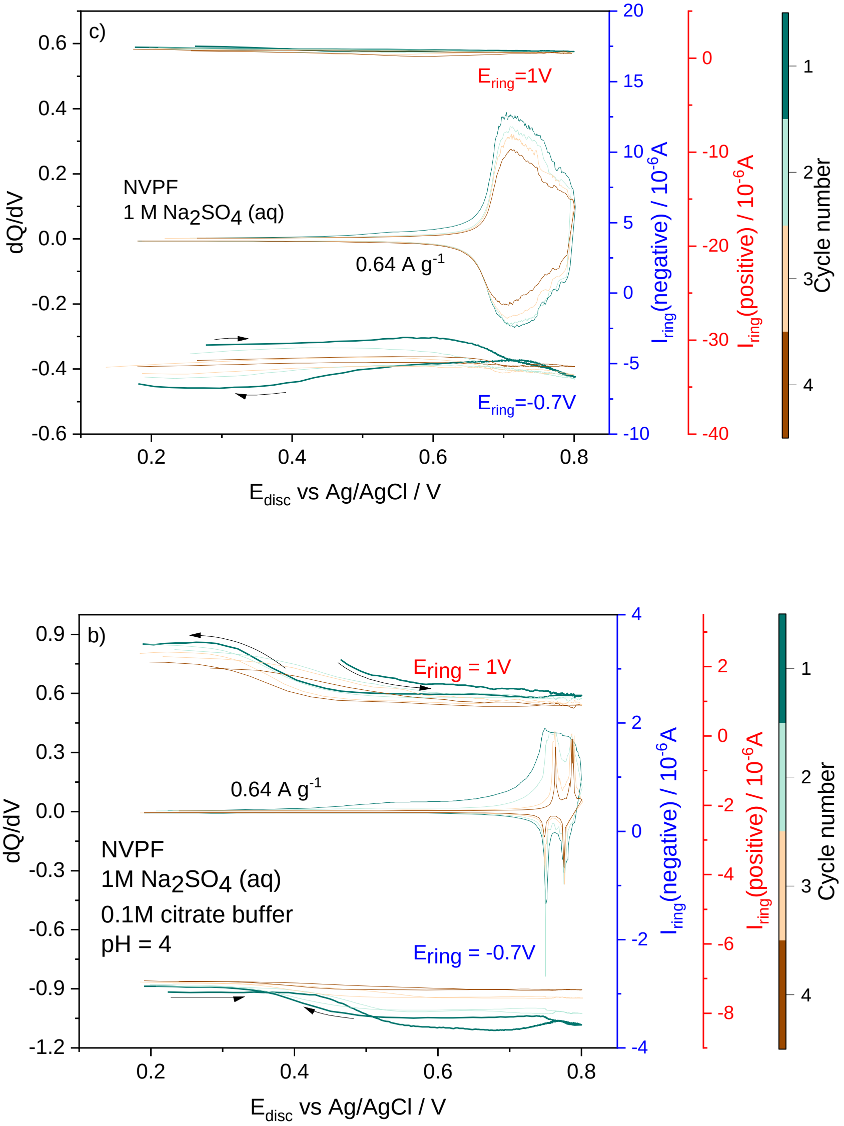

Figure 28. The galvanostatic measurements for NVPF in RRDE set-up recorded in a) unbuffered and b) buffered electrolytes recorded at 5C rate. Data is presented in a form of dQ/dE (middle, left y-axis) together with chronoamperograms of both, negatively (bottom) and positively (top) polarized Pt rings (I_{ring}, right y-axes).

As a result, in the galvanostatic mode, the ring electrode receives a more consistent influx of electrochemically active degradation products, resulting in a steadier current. This scenario complicates the study and quantification of the degradation process *in situ* or *operando* conditions, as a background current/noise becomes a significant contributor. The fluctuations in the current on the ring electrode become less pronounced, making it more challenging to distinguish and attribute the changes solely to specific degradation mechanisms. Hence, for investigations focused on the study of electrochemical degradation and its mechanisms, the potentiodynamic mode appears more suitable due to its ability to accelerate specific degradation processes within a defined potential window, thereby generating more distinguishable and informative signals for analysis.

Indeed, the results obtained through the RRDE technique strongly imply that under pH 4 conditions, there is not only enhanced chemical dissolution of the active material but also a significant contribution from electrochemically-induced generation of soluble $V^{(IV)}$ species. These $V^{(IV)}$ species are subsequently oxidized according to Reaction 25 on the ring electrode. The chemical dissolution study conducted in citric acid media without electrochemical cycling further supports these findings. The absence of accelerated dissolution without electrochemical processes indicates that the observed degradation is not purely driven by chemical factors, but rather by a combination of chemical and electrochemical mechanisms.

The presence and stability of $V^{(IV)}$ species can be explained from a thermodynamic perspective using the Pourbaix diagram presented in Fig. 2. This diagram suggests that under lower pH conditions, $V^{(IV)}$ can be more stable compared to $V^{(V)}$. An alternative explanation could involve the co-insertion of protons during the charging process into the NASICON structure. This co-insertion can potentially destabilize the structure, leading to the release of reduced vanadium species into the electrolyte during discharge. This mechanism is in line with previous studies that have highlighted the role of pH and proton co-insertion in influencing the degradation of materials [149]. In this study, this behavior is observed in the RRDE CV experiment for NVPF in acidic media (Fig. 26 b)), where two distinct peaks can be observed on a positively polarized ring, despite the absence of any electrochemical activity on the disc.

Overall, the findings suggest that $Na_3V_2(PO_4)_2F_3$ holds greater promise as a positive electrode material in comparison to $Na_3V_2(PO_4)_3$ for aqueous systems, as it offers not only higher operating potential but superior chemical stability. The implication is that a properly designed electrolyte with controlled proton and water activity, possibly employing 'water-in-salt' or hybrid electrolyte strategies, could genuinely enable the effective utilization of this material in water-based electrochemical devices. Different coatings, which limit the electrode/water interactions at the interface could also hold a promise.

3.4. Mitigation of degradation of aqueous Na-ion battery electrodes

This work, as well as existing literature, has demonstrated that various inorganic coatings can indeed improve material stability and performance by mitigating unwanted parasitic reactions [117,120,138,150,151]. Techniques such as atomic layer deposition (ALD) enable control over the thickness of coatings, thereby limiting the influence of their low intrinsic conductivity [152]. Moreover, different conductive polymeric coatings have been employed in the past to protect active materials. To the best of current knowledge, none have been applied in aqueous Na-ion battery negative electrodes.

Previously, in this work, it has been shown that parasitic reactions occurring at low potentials on the surface of the electrode are the main culprit for the degradation of $NaTi_2(PO_4)_3$. In this study, different surface coatings were employed to enhance the stability of NTP in 1 M Na_2SO_4(aq.) electrolytes. Electrodeposited Polystyrene Sulfonate (PSS) doped PEDOT (PEDOT(PSS)) and drop-casted Nafion coatings were employed as a means to suppress capacity fade. Al_2O_3, TiO_2, and HfO_2 coatings of two different thicknesses were ALD deposited on the surface of the electrodes as well.

Due to the compatibility of the redox potential of $NaTi_2(PO_4)_3$ (NTP) with electrodeposition, PEDOT was deposited on the material surface using electrochemical methods. There are three different modes of electrochemical deposition: (i) galvanostatic, (ii) potentiostatic, and (iii) potentiodynamic. Among these, the galvanostatic deposition mode was chosen in this work for its simplicity, deposited film quality, and reproducibility.

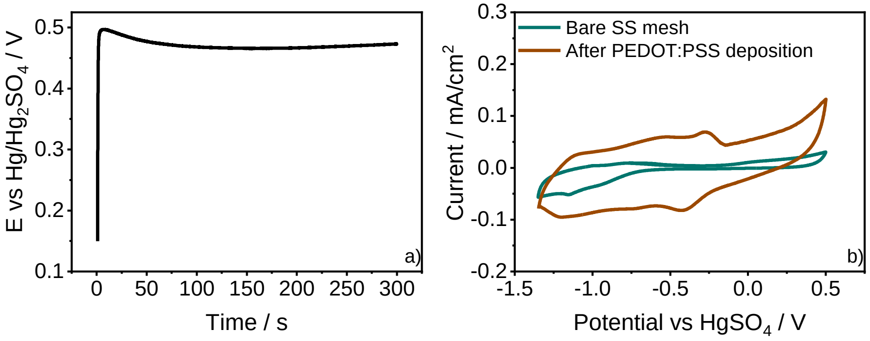

Figure 12. a) galvanostatic deposition of the PEDOT(PSS) on the stainless-steel surface with 0.2 mA cm^{-2} from the solution containing 0.1M NaPSS and 0.01M EDOT and b) CV of electrodeposited PEDOT(PSS) (brown), together with bare SS mesh (green) at 10 mV s^{-1}.

After applying the desired current (0.2 mA cm^{-2}), the oxidative polymerization proceeds at 0.5 V vs Hg/$HgSO_4$. This potential dropped to c.a. 0.45 V as the reaction progressed, consistent with the literature data. After electrodeposition, the presence of PEDOT(PSS) layer was evaluated by two CV scans recorded at 10 mV s^{-1}. The layer exhibited a certain capacity for the reversible insertion and de-insertion of Na^+/H^+ ions across the entire potential range, as shown in Fig. 29 b).

The coating thickness was controlled by varying the electrodeposition time from 2 to 10 min, yielding the total polymerization charge from ~0.032 to 0.16 C. Through this work, it is assumed that the polymer deposition on the surface of electrodes is identical to the deposition on the clean electronic conductors, i.e. it produces a uniform layer.

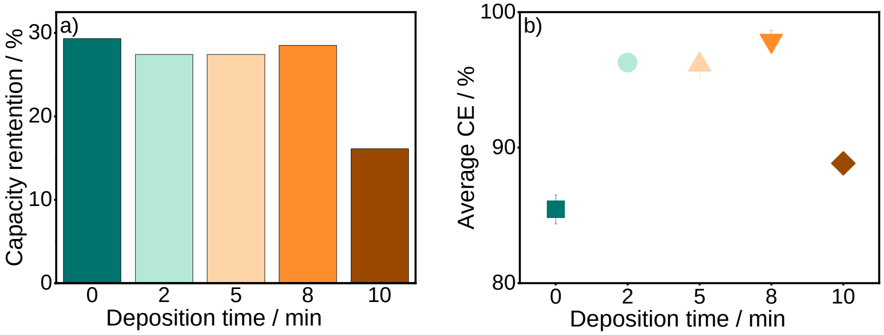

Figure 13. a) capacity retention after 100 GCD cycles and b) average Coulombic efficiency for NTP with different amounts of electrodeposited PEDOT(PSS) on the surface recorded at 1C rate in 1M Na_2SO_4 electrolyte.

After the deposition of the PEDOT(PSS) layer, the electrodes were rinsed with deionized water, and GCD cycling was performed at a 1C rate (133 mA g^{-1}). The primary focus of this was to evaluate its effects on the influence of side reactions, therefore, recorded CE and capacity retention are of special interest. The results presented in Fig. 30 show that the additional polymer layer on the electrodes appears to have no effect, as capacity retention seems to be identical for the first four samples, around 30% after 100 cycles. However, when the electrodeposition time is increased to 10 min, capacity retention drops significantly, to only about 15%. On the other hand, efficiencies show a slightly different, yet interesting trend. Typically, as shown in previous sections, there is a 10-15% CE loss for the GCD cycling of NTP at 1C, attributed to parasitic reactions. The introduction of the polymer layer seems to partially suppress these processes, with CEs for the three samples with deposition times of 2, 5, and 8 min being above 95%. However, additional polymer deposition of 10 min lowers the CE to 88%. It has been experimentally demonstrated that under certain conditions, porous PEDOT(PSS) can indeed catalyze the ORR reaction, although the reaction mechanism remains unclear [153]. Oxygen-mediated self-discharge was identified as one of the main culprits of low efficiency and capacity fade under ambient conditions for NTP. In this case, PEDOT(PSS) provides an additional surface for the oxygen reduction reaction to occur, and in doing so, reduced N3TP no longer participates in the reaction, leading to increased efficiency. However, this process still elevates the pH of the electrolyte, resulting in identical capacity fade. A larger amount of polymer appears to catalyze the reaction even further, leading to an even greater capacity loss.

Nafion is a perfluorosulfonated ionomer that has found applications in organic SIBs as a separator membrane or electrolyte[131,132]. In this study, it was deposited onto the surface of NTP to mitigate the side reactions occurring on the surface and reduce the capacity fade of the electrode. The acidic nature of the polymer should also provide a local buffer and prevent material degradation through elevated pH.

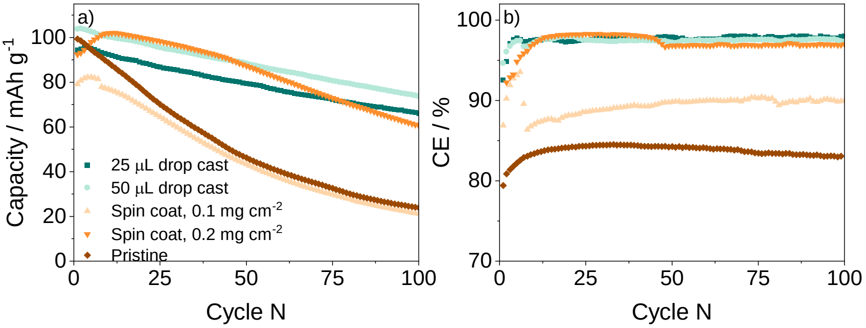

Figure 14. GCD measurements of pristine and Nafion-coated NTP electrodes. a) discharge capacity and b) coulombic efficiency, recorded in 1M Na_2SO_4 electrolyte at 1C rate

Initially, Nafion was deposited on the surfaces of mesh-transferred electrodes using a simple drop-casting method. However, this method has limitations, including an inability to control film quality and volume. Low volumes could not be deposited effectively as they did not spread evenly without mechanical intervention, resulting in an uneven distribution of material. Higher volumes led to overly thick polymer layers that would peel off during the drying process. Therefore, only 25 µL and 50 µL solutions were used for this process, resulting in coatings of c.a. 1 and 2 mg cm^{-2}, respectively. To achieve even thinner coatings, a spin-coater was employed. The depositions were carried out under varying conditions, resulting in two different thicknesses of coatings, with c.a. 0.1 and 0.2 mg cm^{-2} coating.

The results, presented in Fig. 31 alongside the measurements on the pristine electrode, clearly show the positive effects of the Nafion coatings on the electrodes. The initial capacity of the materials was relatively similar, around 100 mAh g^{-1}, which is typical for electrodes prepared in this manner. The pristine sample exhibited the expected behavior, with an efficiency of around 80 – 85% and rapid capacity fade. In contrast, virtually all the polymer-coated samples performed better, and their performance seemed to improve with thicker coatings. Both drop-casted samples (i.e. ones with the thickest coatings) appeared to completely eliminate parasitic reactions, with a coulombic efficiency approaching 100%. As a result, capacity retention was significantly improved, reaching around 80% after 100 cycles, compared to 20% for the pristine electrode.

NTP electrodes were also coated with Al_2O_3, TiO_2, and HfO_2 by ALD. Two different thicknesses of coatings were chosen, approximately 20 and 70 nm. The growth rate per ALD cycle differed by precursor used and was 0.13 nm, 0.12 nm, and 0.05 nm for Al_2O_3, TiO_2, and HfO_2, respectively. Initially, a general electrochemical characterization was performed. As previously discussed, one of the major challenges with inorganic coatings is their low electronic conductivity which can limit charge-transfer kinetics. Initial characterization was done by CV in a bottom-mounted cell in an aqueous 1 M Na_2SO_4 electrolyte. At first glance, all the studied materials, regardless of the coating, show a similar response. All of them display reversible peaks around -0.8 V vs Ag/AgCl, attributed to (de)insertion of two Na ions in NTP structure due to the activity of $Ti^{(III)}/Ti^{(IV)}$ redox pair (Fig. 32). Only the peak current for hafnia-coated sample seems to be reduced. However, the coatings seem to have a negligible effect on redox kinetics.

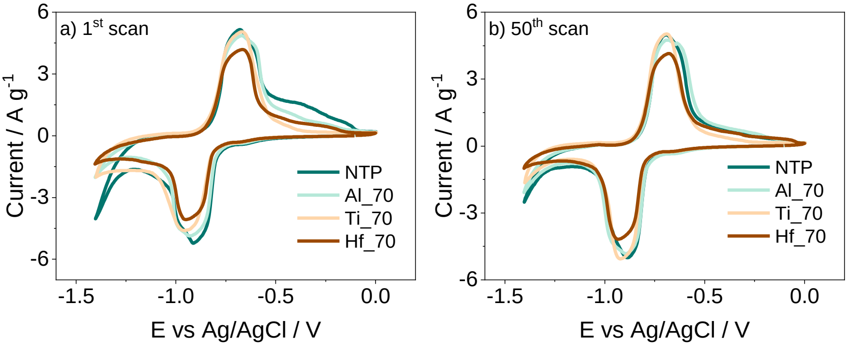

Figure 15. Cyclic voltammetry on pristine and ALD-coated NTP electrodes. a) 1st and b) 50th cycles recorded in aqueous 1 M Na_2SO_4 electrolyte at 5 mV s^{-1}. The sample name displays the coating material (Al, Ti, and Hf for Al_2O_3, TiO_2 and HfO_2, respectively), as well as the coating thickness (70 nm in this case).

A more pronounced difference in cycling voltammograms lies outside the potential range of the main redox reaction ($Ti^{(IV)}/Ti^{(III)}$), specifically below -1.2 V vs Ag/AgCl. As the potential approaches the edge of the stability window of the electrolyte, an increase in negative current is expected, due to the onset of HER. The highest currents, indicating the lowest HER overpotential, are recorded for pristine NTP samples, suggesting that this surface offers the most favorable conditions for HER. ALD coatings seem to mitigate this parasitic reaction overall, with hafnia showing the lowest recorded current. The observed effect is most likely the sum of two distinct factors: unfavorable surface for HER on the oxides and reduction of the porous surface area following the coating. After 50 cycles, HER currents seem to diminish in all studied samples, and the most significant drop is observed for uncoated NTP, however, it is still higher than the ones recorded for the coated samples. Interestingly, even after 50 cycles, the hafnia-coated electrode electrochemical response seems identical to the freshly prepared sample. The drop in currents can be attributed to two different factors (i) the production of insoluble titanium species on the surfaces, limiting the extent of HER, and (ii) the gradual increase in pH at the surface of the electrode, causing the reduction of the reaction potential.

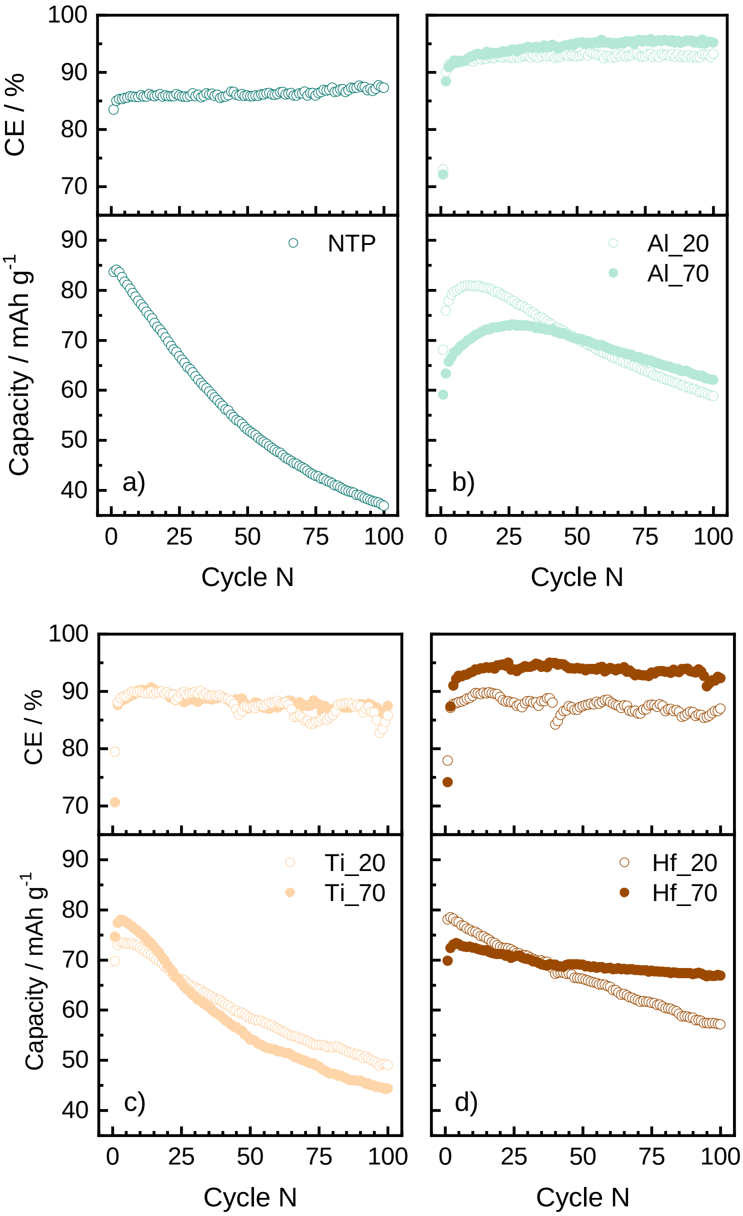

Figure 16. Results of GCD measurements of a) pristine and b) Al_2O_3, c) TiO_2, and d) HfO_2 coated NTP samples recorded in aqueous 1 M Na_2SO_4 at 1C rate.

Effects of coating on long-term electrochemical stability were evaluated by GCD cycling. The results are presented in Fig. 33. For a given measurement, one can notice that pristine samples perform the worst, with capacity retention of just 44% after 100 cycles and CE below 90%. This type of behavior was observed in previous studies as well. The presence of Al_2O_3 on the surface seems to inhibit some of these parasitic processes, as capacity retention rises to 72% and 84%, with the CE of 92% and 95% for 20 nm and 70 nm coating thicknesses, respectively. It is worth noting that there is a slight increase in recorded capacities during the first few cycles. TiO_2 coatings seem to offer protection compared to pristine NTP, however, they perform worse than alumina. There is a similar rise in capacity during the first few cycles and recorded efficiencies are very similar to uncoated samples. Interestingly, in terms of capacity retention, the thinner coatings outperform the thicker ones, retaining 67% of initial discharge capacity vs 57%. HfO_2 coating offers a superior protection, as the electrode, coated with a 70 nm layer retains 91% of initial capacity after 100 cycles with CE of around 95%. 20 nm HfO_2 coating seems to be insufficient to prevent the parasitic reactions, as efficiency is around 90% with notable capacity fade. There is also a slight drop in recorded capacities for all the coated samples compared to the pristine one (4-12%), suggesting that while there is some charge-transfer/ion-insertion blocking due to the presence of insulating layers, it is negligible.

For further characterization, the stability of the coatings was evaluated after cycling. For this purpose, SEM images were recorded on all of the samples before and after 100 GCD cycles (Fig. 34). Freshly synthesized NTP shows cube-shaped particles with size ranging between 50 and 100 nm. After 100 cycles the particles look almost identical, with the only difference being smaller size, as well as few defects. These results look similar to the ones reported in the literature after exposure of NTP to alkaline media [24]. The deposition of the 20 nm Al_2O_3 layer led to the formation of significantly larger sphere-shaped particles. However, after GCD cycling, the particles are barely distinguishable from the pristine NTP. This suggests that alumina coating got dissolved in the media due to increased pH as a result of parasitic reactions. As a result, improvements observed in capacity retention and CE cannot be attributed to the quality of the coating. They are most likely due to the pH buffering associated with the reaction of Al_2O_3 with the hydroxide ions. Electrode material exposure to the electrolyte after the dissolution of alumina could also be responsible for the initial increase in capacity during the first 10-15 cycles recorded during GCD measurements.

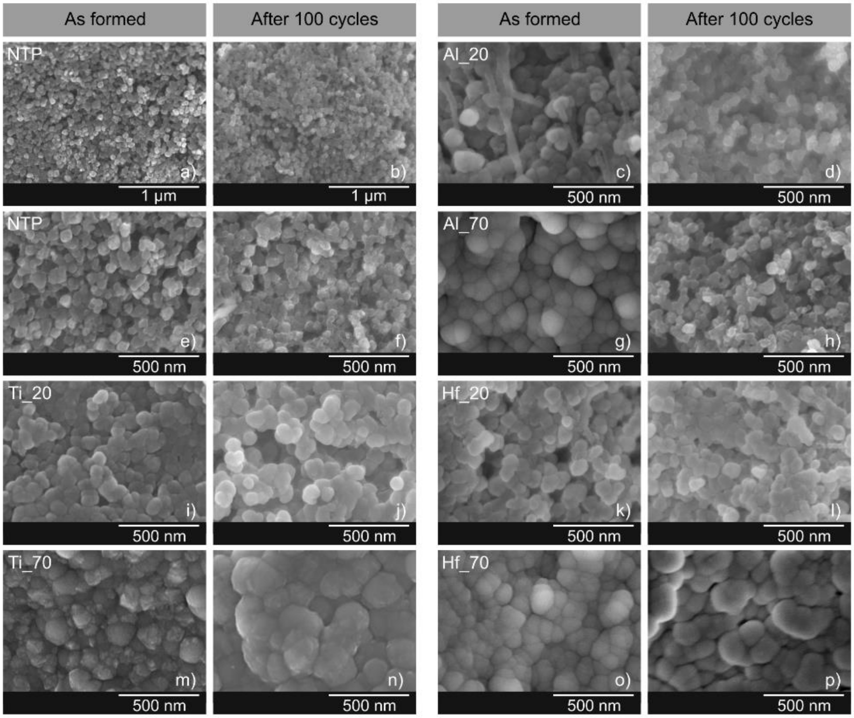

Figure 34. SEM images of the pristine NTP (a), (b), (e), (f) and Al_2O_3–, TiO_2, HfO_2-coated NTP electrodes: Al_20 (c), (d), Al_70 (g), (h), Ti_20 (i), (j), Ti_70 (m), (n), Hf_20 (k), (l) and Hf_70 (o), (p) electrodes before (a), (e), (i), (m), (c), (g), (k), (o) and after 100 GCD cycles in 1 M Na2SO4 (aq.) at 1C rate.

The electrode surface after deposition of 20 nm TiO_2 coating looks almost identical to the alumina counterpart. However, as the thickness of the coating increases to 70 nm, particles become less spherical and some sharper edges can also be observed. Also, unlike alumina, after GCD cycling, morphology remains practically intact. The capacity retention of the titania coated NTP is worse than that of alumina-coated NTP, suggesting limited active material protection regardless of the resilience of the coating itself. Recorded CE of c.a. 90% also implies that TiO_2 does not suppress the bulk of parasitic reactions that could occur during the operation. Another thing to consider is the electrochemical activity of TiO_2 itself, accompanied by a possible proton insertion:

$$\mathrm{Ti^{(IV)}O_2 + xH_2O + xe^- \leftrightarrow Ti^{(IV)}_{1-x}Ti^{(III)}O_{2-x}(OH)_x + xOH^-} \quad (28)$$

This reaction should be responsible not only for the reduced efficiency but also for the production of hydroxide ions, leading to an additional increase in pH. This pH spike could also explain the fact that a thicker ALD coating of TiO_2 leads to lower capacity retention.

To test the possibility of the Reaction (28), 70 nm thick TiO_2 layer was deposited on the surface of the graphite rod under the same conditions as for NTP electrodes. Fig. 35 represents the CV measurements of this rod, contrasted with uncoated graphite. The result shows some electrochemical activity of TiO_2 coating in the studied potential range.

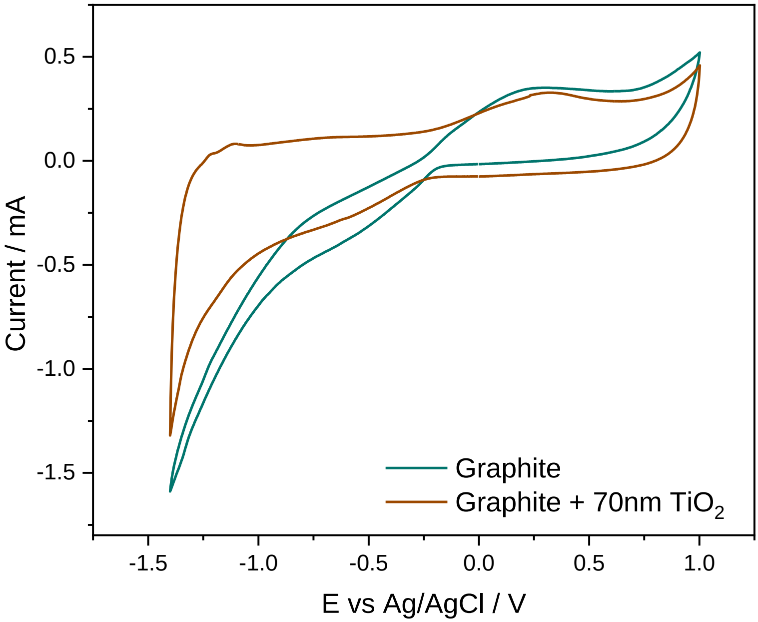

Figure 35. Cyclic voltammograms of bare (green) and TiO_2-coated (brown) graphite electrodes in aqueous 1 M Na_2SO_4 electrolyte at 5 mV s^{-1}.

The initial surface morphology of the HfO_2-coated electrode looks very similar to the one recorded for Al_2O_3 and TiO_2 (Fig. 34). However, in contrast with the other two samples, both hafnia coatings remain unchanged after the GCD cycling, suggesting the superior stability of the coating. In terms of the electrochemical performance of the material itself, recorded capacity retention and CE suggest that 20 nm coating is still insufficient to suppress parasitic reactions and mitigate the degradation. On the other hand, 70 nm hafnia coating outperformed all the other studied samples.

Additional characterization of the coatings was done by employing electrochemical impedance spectroscopy (EIS). The spectra were recorded after the 1st, 2nd, 5th, 10th, 50th, and 100th cycles during the GCD measurements at 1C rate. The results are presented in Fig. 36. The equivalent circuit displayed is the sum of two Randles circuits. The circuit is the simplest and the most commonly used for fitting the electrochemical processes in the ion insertion materials. The Warburg element in this case is deemed to correspond to the semi-infinite ion solid-state diffusion in NTP. Capacitors were replaced with constant phase elements (CPE) to account for the non-ideal behavior of the system. This seems unnecessary for pristine electrode samples, but the introduction of coatings show some deviation from ideality. The low-frequency region is associated with the charge transfer on the electrolyte/electrode interface, and the mid-frequency region represents the behavior of the layer associated with the coating and electrode degradation products.

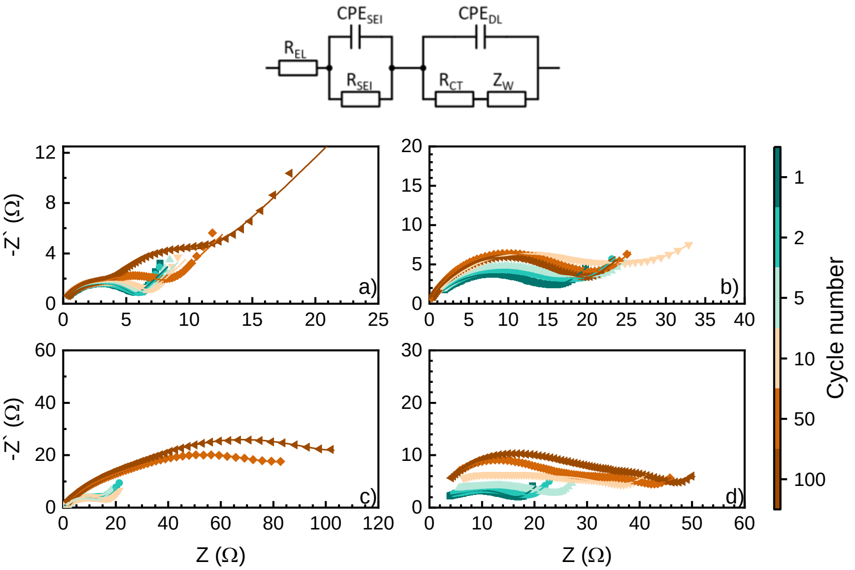

Figure 36. EIS spectra of a) pristine, b) Al_70, c) Ti_70 and d) Hf_70 electrodes during GCD cycling in 1M Na_2SO_4(aq.) at 1C rate. The spectra were fitted to the equivalent circuit presented above.

For the uncoated sample, a gradual increase of the low-frequency semicircle is observed, which can be attributed to the increase in charge-transfer resistance (R_{CT}) due to the degradation of the active material. The simultaneous growth of the mid-frequency semicircle also implies that degradation products tend to accumulate on the surface of an electrode, hindering the diffusion of Na^+ ions during GCD cycling. With the Al_2O_3 coating, we can see a similar increase of charge-transfer resistance up to the 10th cycle, and subsequent drop, probably due to the dissolution of the coating (Fig. 36). This result is in good agreement with the ones observed with SEM imaging and discharge capacities. Despite that, electrode degradation products seem to accumulate on the surface nevertheless, leading to the relatively stable R_{SEI}.

TiO_2 coated sample is again quite interesting, as it shows the highest R_{CT} increase during the cycling. As discussed above, the titania layer stays relatively intact with cycling, as well as displays certain electrochemical activity, which could result in swelling, as well as a pH increase. As a result, NTP dissolution accelerates, leading to the fast build-up of the degradation products on the surface, resulting in a drastic increase in charge-transfer resistance.

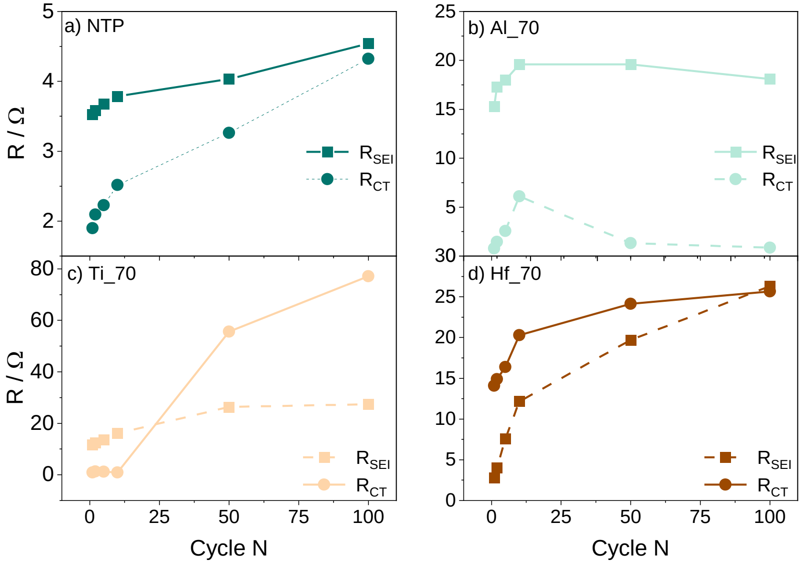

Figure 17. Variation of R_{CT} and R_{SEI} values calculated from the EIS measurements for (a) pristine, (b) Al_2O_3, (c) TiO_2, and (d) HfO_2 coated NTP electrodes.

EIS results for HfO_2 coating stand out from the others. At first, one can clearly see higher initial charge-transfer resistance (Fig. 37 d)). Also, this resistance stays relatively stable during the measurement, suggesting the preservation of an active material. On the other hand, there is a pronounced increase in R_{SEI}. This could be attributed to the more compact and chemically inert nature of the hafnia coating: it provides stability and significant protection to the active material. However, even a small amount of degradation products appears sufficient to block the charge transfer. It needs to be pointed out that the recorded R_{CT} value for 70 nm HfO_2 coating does not significantly exceed the ones measured for the other coatings.

EIS, as well as GCD results suggest that among the studied inorganic coatings, hafnia is the only one that is stable under the GCD conditions, as well as providing the protection of the active material. However, it also partially hinders the charge transfer, as indicated by lower peak currents during CV, lower initial capacity during GCD measurements, and higher R_{CT} recorded with EIS during initial cycles. Therefore, careful design and selection of appropriate ALD parameters are of the essence.

Overall, the results suggest that protective coatings of different origins, can enable the use of NASICON-structured materials as electrodes in aqueous Na-ion batteries. Currently, significant efforts are directed towards the development of ALD-based methods for conformal inorganic coatings, as they hold great promise due to their precision. Nevertheless, organic materials, such as conductive polymers, can also provide a significant benefit.

4. Conclusions

1. Various parasitic reactions such as hydrogen evolution and oxygen reduction occurring at the operating potential and competing with Na-ion (de)insertion are the cause of low Coulombic efficiency and capacity loss of $\mathbf{NaTi_2(PO_4)_3}$ as an electrode material in aqueous electrolytes. Specifically, chemical oxygen reduction catalyzed by $Ti^{(III)}$ in a reduced state of $\mathbf{Na_3Ti_2(PO_4)_3}$ is identified as the main contributor. This reaction leads to the local increase in pH and the subsequent degradation of the active material. Electrolyte buffering is one of the solutions to mitigate the pH increase. However, it shows a lot of issues such as promoting hydrogen evolution on the negative electrode, oxygen evolution on the positive electrode, and being of finite capacity in a closed system.

2. Electrochemically-induced $Mn^{(II)}$ dissolution is the main cause of material degradation and capacity loss during the operation of $\mathbf{Na_3MnTi(PO_4)_3}$, $\mathbf{Na_3MnPO_4CO_3}$, and $\mathbf{Na_4Mn_3(PO_4)_2P_2O_7}$ in aqueous electrolytes. *In situ* experiments using the Rotating Ring-Disc Electrode technique show that the formation of $Mn^{(III)}$ during charging and its strong Jahn-Teller distortion tends to destabilize the structure of Mn-based materials and promote Mn dissolution during electrochemical cycling. Only the presence of titanium seems to slightly suppress this effect. However, $Mn^{(II)}$ dissolution and its aqueous stability are still observed. *Ex situ* quantitative analysis using scanning electron microscopy and energy dispersive X-ray spectroscopy indicates that most of the manganese still remains in the framework structure but is either electrochemically inactive or inaccessible. Overall, the studied materials show a very limited potential to be applied as positive electrodes in low concentration aqueous electrolytes.

3. $\mathbf{Na_3V_2(PO_4)_3}$ shows decent capacity retention when cycled in a highly concentrated aqueous but rapid capacity loss in low concentration aqueous electrolytes. Vanadium dissolution is shown to be the main reason for the degradation. Most of it is chemically-induced as the majority of vanadium dissolves from the electrode by immersion in the electrolyte. The introduction of fluoride ions into phosphate framework structure seems to stabilize in as $\mathbf{Na_3V_2(PO_4)_2F_3}$ shows significantly better chemical stability. However, it still suffers from vanadium electrochemically-induced dissolution during cycling with practically all

vanadium dissolving from the structure into the electrolyte during 100 cycles. Double redox titrimetry and i*n situ* experiments using the rotating ring-disc electrode technique show $V^{(V)}$ to be the main dissolution product. Lowering the electrolyte pH seems to promote additional dissolution of $V^{(IV)}$ species during the discharge phase, accelerating the dissolution even further. Overall, with the stabilizing electrolyte additives or electrode coating, **$Na_3V_2(PO_4)_2F_3$** has the potential to be utilized as a positive electrode in aqueous Na-ion batteries.

4. Conformal electrode polymeric or ceramic coatings have the potential to mitigate the degradation of **$NaTi_2(PO_4)_3$** in aqueous electrolytes. The electrochemically deposited **poly(3,4-ethylenedioxythiophene) polystyrene sulfonate** layer seems to provide alternative sites for electrochemical oxygen reduction reaction, which consumes local O_2, improves the Coulombic efficiency, but still increases the pH. On the other hand, acidic polymers such as **Nafion** seem to provide sufficient mechanical protection and local buffering which leads to high Coulombic efficiency and significantly improved capacity retention. Ceramic coatings such as atomic layer deposited **Al_2O_3**, **TiO_2**, and **HfO_2** are another viable option**.** However, the results show that Al_2O_3 is itself not sufficiently stable in higher pH and dissolves during extended cycling in aqueous electrolytes. TiO_2 seems to show some electrochemical activity itself leading to local pH increase and accelerated **$NaTi_2(PO_4)_3$** degradation during cycling. Only HfO_2 emerged as a superior coating material which is sufficiently electrochemically inert and stable to protect **$NaTi_2(PO_4)_3$** from degradation during extended cycling.

Santrauka

1 - Įvadas

Energijos poreikiui nuolatos augant bei siekiant sumažinti žmonijos priklausomybę nuo iškastinio kuro, vis daugiau dėmesio skiriama atsinaujinantiems ištekliams, tokiems kaip vėjo ar saulės energija. Per pastarąjį dešimtmetį energijos gamyba panaudojant šiuos šaltinius labai atpigo, todėl saulės bei vėjo energetika tampa vis konkurencingesnė, tačiau norint visapusiškai išnaudoti šias technologijas yra reikalingos energijos kaupimo sistemos. Vienas efektyviausių energijos saugojimo būdų - elektrocheminės baterijos. Įkraunamų baterijų istorijasiekia daugiau nei du šimtmečius. Priklausomai nuo paskirties yra naudojamos rūgštinės švino, nikelio-geležies, nikelio-metalo hidrido ar ličio jonų baterijos. Pastarosios yra itin plačiai naudojamos dėl patrauklių eksploatacinių savybių, tačiau norint jas pritaikyti stacionariam energijos saugojimui pramoniniu mąstu susiduriama su iššūkiais, susijusiais su elektrodų medžiagų trūkumu ir organinių elektrolitų degumu. Dėl šių priežasčių imta ieškoti alternatyvių technologijų. Vandeninės Na jonų baterijos laikomos perspektyvia alternatyva, kadangi jose naudojamos prieinamos medžiagos ir nedegūs vandeniniai elektrolitai. Nors toks krūvį nešančių jonų ir elektrolito pakeitimas išsprendžia minėtas problemas, tačiau turi ir savo trūkumų. Visų pirma, didesnis jonų spindulys riboja natrio interkaliacijos galimybes. Be to, dėl didelio tirpiklio poliškumo kyla problemų, susijusių su metalų junginių tirpimu, o dėl riboto vandens elektrocheminio stabilumo lango dažnai sunku išvengti šalutinių vandenilio ir deguonies skyrimosi reakcijų. Todėl naujų medžiagų paieška bei kūrimas yra labai svarbus uždavinys. Tarp įvairių junginių klasių, NASICON struktūros fosfatai laikomi perspektyviomis Na jonų elektrodų medžiagomis, tačiau, norint atskleisti šių medžiagų potencialą, reikia suprasti ir išspręsti kai kurias problemas. Pagrindinis šios disertacijos tikslas buvo ištirti ir padidinti elektrodo/elektrolito sandūros stabilumą vandeninėse Na jonų baterijose.

Pagrindinis šio **darbo tikslas** - ištirti vandeninių natrio jonų baterijų elektrochemines sandūras, suprasti jų degradacijos procesus bei pasiūlyti degradacijos mažinimo būdus.

Darbo naujumas: šiame darbe pirmą kartą atlikti išsamūs *ex situ* ir *in situ* elektrocheminiai tyrimai, siekiant suprasti NASICON struktūros fosfatų bei kelių struktūriškai giminingų karkasinių junginių degradacijos procesų mechanizmus vandeniniuose elektrolituose.

Darbo uždaviniai:

- Ištirti ir suprasti NASICON struktūros **$NaTi_2(PO_4)_3$**, kaip vandeninių Na jonų baterijų neigiamo elektrodo medžiagos, elektrochemines degradacijos procesus, taikant įvairius struktūrinius, morfologinius, spektroskopinius ir elektrocheminius tyrimo metodus

- Ištirti ir suprasti NASICON struktūros fosfatinių ir jiems struktūriškai giminingų karkasinių mangano junginių **$Na_3MnTi(PO_4)_3$, $Na_3MnPO_4CO_3$** bei **$Na_4Mn_3(PO_4)_2P_2O_7$**, kaip vandeninių Na jonų baterijų teigiamų elektrodų medžiagų, elektrochemines degradacijos procesus, taikant įvairius struktūrinius, morfologinius, spektroskopinius ir elektrocheminius tyrimo metodus

- Ištirti ir suprasti NASICON struktūros fosfatinių ir struktūriškai giminingų karkasinių vanadžio junginių **$Na_3V_2(PO_4)_3$** ir **$Na_3V_2(PO_4)_2F_3$**, kaip vandeninių Na jonų baterijų teigiamų elektrodų medžiagų, elektrocheminio irimo procesus, taikant įvairius struktūrinius, morfologinius, spektroskopinius ir elektrocheminius tyrimo metodus

- Ištirti ir pritaikyti atominio sluoksnio nusodinimo metodu suformuotas bei laidžių polimerų dangas **$NaTi_2(PO_4)_3$** elektrodų apsaugai nuo degradacijos vandeniniuose elektrolituose

Ginamieji teiginiai:

- Cheminė deguonies redukcijos reakcija, kurią katalizuoja $Ti^{(III)}$, esantis įkrautame **$Na_3Ti_2(PO_4)_3$**, yra pagrindinė šalutinė reakcija, lemianti savaiminį išsikrovimą bei lokalų elektrolito šarmėjimą, kurie yra svarbiausios **$NaTi_2(PO_4)_3$**, kaip neigiamo vandeninių Na jonų baterijų elektrodo, degradacijos ir talpos mažėjimo priežastys.

- Nustatyta, kad elektrochemiškai sukeltas mangano tirpimas ir Mn(II) termodinaminis stabilumas beveik neutralioje vandeninėje terpėje yra pagrindiniai šalutiniai procesai, lemiantys **$Na_3MnTi(PO_4)_3$**, **$Na_3MnPO_4CO_3$** ir **$Na_4Mn_3(PO_4)_2P_2O_7$** talpos mažėjimą mažos koncentracijos vandeniniuose elektrolituose. *In-situ* degradacijos tyrimai rodo, kad stiprus Jahn-Teller efektas, kurį sukelia $Mn^{(III)}$, esantis šių karkasinių junginių įkrautoje būsenoje, yra labiausiai tikėtina priežastis, lemianti jų struktūrinį nestabilumą. Vis dėlto, greitas mangano tirpimas veikiausiai vyksta tik paviršiuje, todėl didžioji dalis medžiagos lieka nepaveikta, tačiau tampa elektrochemiškai nepasiekiama. Titano įvedimas stabilizuoja karkaso struktūrą ir lėtina jo elektrochemiškai sukeliamą degradaciją.

- Cheminis vanadžio tirpimas ir $V^{(V)}$ stabilumas mažos koncentracijos beveik neutraliuose vandeniniuose elektrolituose yra pagrindinė $\mathbf{Na_3V_2(PO_4)_3}$ degradacijos priežastis. Elektrocheminis įkrovimas/iškrovimas tik pagreitina šį procesą. Nustatyta, kad fluorido jonai $\mathbf{Na_3V_2(PO_4)_2F_3}$ struktūroje gerokai padidina junginio atsparumą cheminiam tirpimui, tačiau neapsaugo nuo elektrocheminės degradacijos, kadangi abiejose medžiagose ilgainiui beveik visas vanadis yra išplaunamas iš fosfatinio karkaso.

- Apsauginės keraminės arba polimerinės dangos yra veiksmingas ir lengvai pritaikomas $\mathbf{NaTi_2(PO_4)_3}$ apsaugos nuo degradacijos mažos koncentracijos vandeniniuose elektrolituose būdas. Atominio sluoksnio nusodinimo būdu suformuotos Al_2O_3 ar TiO_2 dangos yra nestabilios arba pačios dalyvauja šalutinėse reakcijose ir nepakankamai apsaugo elektrodo medžiagą, tuo tarpu HfO_2 sluoksniai yra pakankamai chemiškai inertiški ir užtikrina veiksmingą apsaugą. *In-situ* suformuota **poli(3,4-etilenedioksiatiofeno)** polimerinė danga tik pakeičia elektrocheminės deguonies redukcijos reakcijos lokalizaciją, tačiau yra nepakankamai tvirta, kad apsaugotų medžiagą nuo lokalaus pašarmėjimo poveikio. **Nafion** danga užtikrina palyginti gerą apsaugą, kurią, veikiausiai, lemia mechaninis tvirtumas bei rūgštinė polimero prigimtis, veikianti kaip lokalus buferis.

2 – Metodika

Šiame darbe naudotos elektrodų aktyviosios medžiagos buvo susintetintos skirtingais būdais, pasirinktais dėl paprastumo ir rezultatų atsikartojamumo. Po sintezės visos medžiagos buvo sumaltos rutuliniame malūne (350 aps min^{-1}, 2 val.). Siekiant užtikrinti elektroninį laidumą, sumalti milteliai buvo padengti anglimi, pirolizuojant anglies pirmtaką (gliukozę arba citrinos rūgštį). Duomenys apie naudotus sintezės metodus, anglies pirmtakus ir vidutinę aktyviosios medžiagos masę, tenkančią 1 cm^2 paruošto elektrodo, apibendrinti 1 lentelėje.

Pirmiausia milteliai buvo charakterizuoti rentgeno spindulių dirfakcijos (XRD) metodu (Bruker D2 Phaser arba Rigaku Miniflex II). Dalelių morfologijai tirti naudota skenuojanti elektroninė mikroskopija (SEM) (Hitachi SU 70). Anglies kiekis dengtose medžiagose nustatytas naudojant termogravimetrinę analizę (TGA) (PerkinElmer STA600). Elektrodų paviršiaus charakterizavimui naudotas mažos skiriamosios gebos stalinis SEM mikroskopas (Hitachi TM-6000). Rentgeno fotoelektronų spektroskopijos (XPS) matavimai atlikti "Kratos Axis Supra" spektrometru.

Elektrodai buvo paruošti sumaišant 70 % aktyviosios medžiagos su 20 % anglies ir 10 % polimerinio rišiklio (PVDF). Iš pradžių veiklioji medžiaga ir anglis buvo sumaišytos rutuliniame malūne (150 aps min^{-1}, 1 val.). Po to buvo pridėta tirpiklio (NMP), rišiklio ir viskas sumaišyta (350 aps min^{-1}, 2 val.). Paruošta suspensija buvo užtepta ant aliuminio folijos 300 µm storio sluoksniu ir išdžiovinta (120 °C, 3 val.). Elektrodai elektrocheminiams matavimams buvo suformuoti perkeliant gautą kompozitą ant nerūdijančio plieno (SS) tinklelio. Atliekant degradacijos tyrimus, dalis aktyvios elektrodo medžiagos (20 % masės) buvo pakeista HfO_2, kuris naudotas kaip vidinis standartas.

Sukamo diskinio elektrodo su žiedu (RRDE) eksperimentuose ta pati suspensija buvo užtepta ant stikliškosios anglies disko elektrodo ir išdžiovinta per naktį kambario sąlygomis.

1 lentelė. Elektrodų paruošimo suvestinė

Aktyvioji medžiaga	**Sintezės būdas**	**Anglies pirmtakas**	**Akt. medžiagos masė / elektrodo ploto vnt. (mg cm^{-2})**
NTP	Hidroterminė	Gliukozė	2.1 ± 0.3
NVP	Kietafazė	Citrinų r.	2.2 ± 0.7
NVPF	Zolių-gelių	Citrinų r.	2.6 ± 0.4
NMTP	Kietafazė	Gliukozė	2.3 ± 0.7
NMPP	Kietafazė	Gliukozė	2.6 ± 0.3
NMCP	Hidroterminė	-	1.8 ± 0.2
RRDE	-	-	4 ± 1

Pradinis medžiagų elektrocheminis charakterizavimas buvo atliekamas ciklinės voltamperometrijos metodu (PGSTAT-302, "Metrohm", "Autolab"), naudojant ant SS tinklelio perkeltus elektrodus ir specialiai pagamintas celes, kuriose darbinis elektrodas įmontuojamas apačioje. Grafito strypas ir

Ag/AgCl (Metrohm, Autolab) naudoti kaip pagalbinis ir palyginamasis elektrodai, atitinkamai. Glavanostatinio įkrovimo/iškrovimo (GCD) matavimai atlikti naudojant ciklinio testavimo stendą Neware CT-4008-5V10 mA. Jei nenurodyta kitaip, matavimai atlikti naudojant 1 mol dm^{-3} Na_2SO_4 elektrolitą.

Neigiamų elektrodų savaiminio išsikrovimo eksperimentai buvo atliekami įkraunant elektrodą ir po to stebint atviros grandinės potencialo kitimą įvairiomis sąlygomis. Savaiminis išsikrovimas taip pat buvo tiriamas skenuojančiuoju elektrocheminiu mikroskopu naudojant 25 µm skersmens platinos zondą, poliarizuotą ties -0.5 V (Ag/AgCl). Matavimai atlikti konkurenciniame režime, kuomet deguonies redukcijos reakcija vyksta ir ant darbinio elektrodo, ir ant Pt zondo.

Vanadžio ir mangano junginių, kaip teigiamų elektrodų medžiagų, degradacija buvo tiriama naudojant RRDE (Metrohm, Autolab) įrenginį, esant 1200 aps min^{-1} sukimosi greičiui. Ant disko susidarančių reakcijos produktų surinkimo ant žiedo efektyvumas eksperimentiškai įvertintas panaudojant $[Fe(CN)_6]^{4-}/[Fe(CN)_6]^{3-}$ redokso porą. Gauta 23.4 % vertė.

Aiškinantis mangano oksidų nusėdimą ant platinos žiedo RRDE eksperimentuose papildomai atlikti kvarco kristalo mikrogravimetrijos tyrimai (QCM922, Seiko) su 6 MHz kvarco kristalais (Intellemetrics). Kvarco elektrodo masės kitimas registruotas 0.1 mol dm^{-3} $MnSO_4$ tirpale, uždavus 1.2 V (Ag/AgCl) potencialą. Matavimo jautrumas buvo 12.27 ng Hz^{-1} cm^{-2}.

NTP elektrodų apsauginių dangų kokybė ir poveikis buvo vertinami elektrocheminės impedanso spektroskopijos (EIS) metodu. Matavimai buvo atliekami 1 Hz - 10 kHz dažnių diapazone su 10 mV įtampos amplitude esant -0.8 V (Ag/AgCl), kas atitinka NTP išsikrovimo potencialą.

3 – Rezultatai

3.1 – Šalutinių reakcijų įtaka $NaTi_2(PO_4)_3$

$NaTi_2(PO_4)_3$ dėl žemo $Ti^{(IV)}/Ti^{(III)}$ poros oksidacijos-redukcijos potencialo (-0.6 V (SHE)) yra labai tinkama medžiaga grįžtamam natrio kaupimui Na jonų baterijose. Viena vertus, tai gali padidinti bendrąją celės įtampą, kita vertus, iškyla problemos dėl galimų šalutinių reakcijų. Vandeninėse baterijose šalutinės neigiamo elektrodo reakcijos dažniausiai yra susijusios su elektrolitu (vandenilio skyrimosi reakcija - HER) ir ištirpusiu deguonimi (deguonies redukcijos reakcija - ORR). Įkrauta medžiaga, $Na_3Ti_2(PO_4)_3$ (N3TP), taip pat gali savaime išsikrauti reaguodama su vandeniu arba deguonimi. Visos šios reakcijos prisideda prie elektrolito pH didėjimo, kuris sukelia aktyvios medžiagos tirpimą. Padidinus elektrolito pH galima šiek tiek sumažinti šių reakcijų įtaką, tačiau NTP atveju toks būdas netinka dėl medžiagos nestabilumo šarminėje terpėje. Ieškant problemos sprendimo, buvo ištirtas pH stabilizavimo buferių pagalba poveikis. Gauti rezultatai parodė, kad nors buferių naudojimas gali sustabdyti medžiagos tirpimą, jis taip pat pagreitina HER, ką parodo sumažėjęs kuloninis našumas. Ši reakcija ilgainiui turėtų išeikvoti elektrolito buferinę talpą, todėl mažai tikėtina, kad buferiniai elektrolitai duos ilgalaikį teigiamą poveikį, ypač realiuose prietaisuose, kuriuose elektrolitų kiekis ribotas.

N3TP savaiminis išsikrovimas, kitaip tariant, $Ti^{(III)}$ oksidacija įkrautame neigiamame elektrode gali vykti dviem keliais:

$$Na_3Ti_2(PO_4)_3 + 2H_2O \leftrightarrow NaTi_2(PO_4)_3 + 2Na^+ + 2OH^- + H_2 \quad (1)$$

$$Na_3Ti_2(PO_4)_3 + O_2 + 2H_2O \leftrightarrow NaTi_2(PO_4)_3 + 4Na^+ + 4OH^- \quad (2)$$

Savaiminio išsikrovimo tyrimai, atlikti įvairiomis sąlygomis, bei skenuojančios elektrocheminės mikroskopijos matavimai vienareikšmiškai rodo, kad aplinkos atmosferoje dominuoja deguonies redukcijos skatinamas savaiminis išsikrovimas. Jo trukmė - maždaug 10 valandų. Tai reiškia, kad net ir esant santykinai greitam 1C galvanostatinio įkrovimo/iškrovimo greičiui, ši reakcija reikšmingai prisideda prie kuloninio našumo mažėjimo.

3.2 – Karkasinių Mn fosfatų kaip teigiamų elektrodų medžiagų stabilumas vandeniniuose elektrolituose

Mangano junginiai yra labai patrauklūs kaip teigiamų elektrodų medžiagos dėl aukšto teigiamo darbinio potencialo, redokso būsenų įvairovės ir didelio paplitimo. Tačiau ankstesni tyrimai parodė, kad šių medžiagų talpa mažėja dėl aktyviosios medžiagos tirpimo, ypač vandeninėje terpėje. Šios degradacijos mechanizmas vis dar nėra suprastas, be to, didelę įtaką turi eksploatavimo sąlygos.

Šiame darbe įvairiais metodais buvo tiriamas trijų skirtingų karkasinių mangano junginių ($Na_3MnTi(PO_4)_3$, $Na_4Mn_3(PO_4)_2P_2O_7$, $Na_3MnPO_4CO_3$) degradacija praskiestuose vandeniniuose elektrolituose. Pirminiai rezultatai parodė, kad ciklavimo metu iš aktyvios elektrodo medžiagos pasišalina didelis kiekis $Mn^{(II)}$. Nustatyta, kad ištirpęs Mn pakartotinai nusėda ant elektrodo paviršiaus elektrochemiškai aktyvių MnO_x junginių pavidalu, ir tai prisideda prie tariamo elektrodo krūvio talpos išlaikymo.

Siekiant išsiaiškinti skilimo mechanizmą *in-situ* buvo naudojamas besisukančio disko elektrodo su žiedu (RRDE) metodas. Nustatyta, kad perteklinis medžiagos įkrovimas, kuris yra pagrindinė junginių su manganu degradacijos priežastis ličio jonų baterijose, praskiestuose vandeniniuose elektrolituose vaidina nereikšmingą vaidmenį. *In-situ* atlikto tyrimo rezultatai rodo, kad įkrovimo proceso metu dėl $Mn^{(III)}$ susidarymo pasireiškia stiprus Jahn-Teller efektas, lemiantis mangano tirpimą $Mn^{(II)}$ formoje. Titano buvimas gardelėje slopina šį procesą, tačiau $Mn^{(II)}$ tirpimas stebimas ir elektrodo iškrovimo metu. Be to, atlikus degradavusių elektrodų analizę paaiškėjo, kad, nepaisant žymaus $Mn^{(II)}$ kiekio pasišalinimo iš gardelės, didelė dalis mangano lieka elektrode, tačiau tampa elektrochemiškai nepasiekiama. Apibendrinant galima teigi, kad tirti Mn junginiai yra netinkami naudoti kaip Na jonų teigiamų elektrodų medžiagos praskiestuose vandeniniuose elektrolituose.

3.3 – Karkasinių V fosfatų kaip teigiamų elektrodų medžiagų stabilumas vandeniniuose elektrolituose

Kita perspektyvi teigiamų elektrodų medžiagų klasė - vanadžio junginiai. Po mangano vanadis pasižymi vienu aukščiausių darbinių potencialų tarp lengvai prieinamų metalų. Tačiau ir šioms medžiagoms būdingas vanadžio tirpimas. Šiame darbe buvo tiriamas dviejų vanadžio junginių - $Na_3V_2(PO_4)_3$ (NVP) ir $Na_3V_2(PO_4)_2F_3$ (NVPF) stabilumas.

Elektrocheminis charakteriziavimas ir degradavusių elektrodų bei panaudotų elektrolitų analizė parodė, kad aktyvios medžiagos tirpimas iš tiesų yra pagrindinis degradaciją lemiantis veiksnys. Atlikus ciklinės voltamperometrijos (CV) arba galvanostatinio įkrovimo ir iškrovimo (GCD) matavimus paaiškėjo, kad praktiškai visas vanadis ištirpo. Parodyta, kad $Na_3V_2(PO_4)_3$ ištirpsta praskiestuose vandeniniuose elektrolituose net ir be jokio elektrocheminio poveikio, todėl jis yra netinkamas naudoti vandeninėse baterijose. Fluorido jonų įvedimas į gardelę padidina elektrodo darbinį potencialą bei stabilizuoja medžiagą elektrolite.

Degradacijos mechanizmai buvo tiriami *in-situ* taikant RRDE metodą skirtingo pH buferiuotuose tirpaluose (pH 4 ir 7). Nustatyta, kad neutraliuose tirpaluose abi medžiagos įkrovimo metu tirpsta, susidarant tirpiems $V^{(V)}$ junginiams. Mažesnio pH elektrolite papildomai stebimas tirpių $V^{(IV)}$ formų susidarymas iškrovimo metu, kas paspartina medžiagos degradaciją. Be to, rūgštesnėje terpėje, ypač NVPF atveju, prisideda protonų kointerkaliacija aktyviojoje medžiagoje. Tai destabilizuoja gardelę ir galiausiai lemia redukuotų vanadžio formų ($V^{(III)}$ ir $V^{(IV)}$) perėjimą į tirpalą iškrovimo metu.

Apibendrinant galima teigti, kad $Na_3V_2(PO_4)_2F_3$, palyginti su $Na_3V_2(PO_4)_3$, yra perspektyvesnė teigiama elektrodų medžiaga vandeninėms sistemoms, nes ji pasižymi ne tik aukštesniu teigiamu darbiniu potencialu, bet ir didesniu cheminiu stabilumu. Tačiau, norint išnaudoti šio junginio elektrocheminį potencialą, būtina rasti priemonių tirpimui slopinti.

*3.4 – **Polimerinės apsauginės $NaTi_2(PO_4)_3$ dangos***

Ieškant būdų sumažinti $NaTi_2(PO_4)_3$ krūvio talpos mažėjimą, kurį sukelia šios medžiagos tirpimas padidėjus tirpalo pH, buvo ištirtos kai kurios laidžios polimerinės ir atominio sluoksnio nusodinimo (ALD) būdu suformuotos apsauginės dangos.

Laidžios polimerinės dangos gali būti veiksminga priemonė sušvelninti nepageidaujamas šalutines reakcijas NTP elektrodų paviršiuje. Nustatyta, kad elektrochemiškai nusodintas PEDOT(PSS) sluoksnis pakeičia deguonies redukcijos reakcijos lokalizaciją ir taip pagerina NTP įkrovimo/iškrovimo kuloninį našumą, tačiau neapsaugo aktyviosios medžiagos nuo ORR sukeliamo pH padidėjimo ir degradacijos. Dangos storio didinimas problemos neišsprendžia, kadangi dar labiau skatina ORR. Tuo tarpu Nafion dangos eliminuoja nepageidaujamas šalutines reakcijas ir užtikrina puikią apsaugą, kuri leido pasiekti aukštą CE (apie 100 %) ir geresnį krūvio talpos išlaikymą (80 % po 100 GCD ciklų, palyginti su 20 % elektrodų be apsauginės dangos atveju).

3.5 – ALD būdu suformuotos apsauginės $NaTi_2(PO_4)_3$ dangos

Kitas būdas sumažinti NTP krūvio talpos mažėjimą - neorganinės dangos. Siekiant pagerinti neigiamų elektrodų veikimą buvo ištirtos ALD būdu suformuotos TiO_2, Al_2O_3 ir HfO_2 skirtingo storio (20 ir 70 nm) dangos. Jos buvo nusodintos ant jau suformuotų elektrodų paviršiaus. Visi bandiniai pasižymėjo geresniu krūvio talpos išlaikymu bei kuloniniu našumu palyginti su nedengtais NTP elektrodais. Vis dėlto, nepaisant geresnių rezultatų, Al_2O_3 danga praktiškai pilnai ištirpo po 100 GCD ciklų. Taigi, jos apsauginis poveikis, veikiausiai sietinas su pH buferiavimu tirpimo metu. Tą patvirtina ir analogiški dėsningumai, t.y. krūvio talpos didėjimas pradiniuose cikluose, stebėtas ir fosfatiniuose buferiniuose tirpaluose.

TiO_2 buvo stabilesnis, kadangi po 100 GCD ciklų danga buvo praktiškai nepažeista, tačiau prastas krūvio talpos išlaikymas, ypač storesnės dangos atveju, bei žemas kuloninis našumas parodė šalutinių reakcijų įtaką. Stebimi dėsningumai paaiškinti elektrocheminiu pačios TiO_2 dangos aktyvumu, kuomet redukuojantis $Ti^{(IV)}$ į $Ti^{(III)}$ vyksta protonų įterpimas, dėl ko lokaliai padidėja pH, NTP tirpsta ir mažėja talpa. Šią prielaidą patvirtina ir tai, kad storesnės TiO_2 dangos atveju krūvio talpa mažėjo sparčiau.

Geriausiu cheminiu stabilumu bei apsauginėmis savybėms pasižymėjo HfO_2. Gauti rezultatai rodo, kad 20 nm storio danga yra per plona NTP stabilumui užtikrinti, tačiau 70 nm storio oksido sluoksniu padengtas bandinys pasižymėjo didesniu CE (95 %) ir puikiu talpos išlaikymu (91% po 100 ciklų). Tačiau, kaip parodė elektrocheminės impedanso spektroskopijos matavimai, HfO_2 lemia krūvio pernešimo varžos NTP elektroduose padidėjimą, todėl labai svarbu optimizuoti apsauginės dangos storį.

Atlikti tyrimai rodo, kad polimerinės bei neorganinės dangos gali būti pritaikytos NTP kaip neigiamo elektrodo medžiagai vandeninėse Na jonų baterijose apsaugoti. Pastartuoju metu daug dėmesio skiriama ALD metodams vystyti, kadangi jie laikomi labai perspektyviais dėl savo tikslumo, tačiau organinės medžiagos, pvz., laidūs polimerai, taip pat gali turėti privalumų.

4 – Išvados

1. **$NaTi_2(PO_4)_3$** elektrodų krūvio talpos mažėjimą bei žemą kuloninį našumą vandeniniuose elektrolituose lemia įvairios šalutinės reakcijos, vykstančios įkrovimo/iškrovimo potencialų srityje ir konkuruojančios su Na jonų (de)interkaliacija. Didžiausią įtaką turi cheminė deguonies redukcijos reakcija, kurią katalizuoja $Ti^{(III)}$, esantis redukuotoje NTP formoje **- $Na_3Ti_2(PO_4)_3$.** Ši reakcija lemia lokalų pH padidėjimą ir su tuo susijusį aktyviosios medžiagos tirpimą. Elektrolito pH galima stabilizuoti naudojat buferius, tačiau tai paspartina vandenilio skyrimąsi ant neigiamo elektrodo, deguonies skyrimąsi ant teigiamo elektrodo, be to, uždaroje sistemoje buferinė talpa yra ribota.

2. Pagrindinė **$Na_3MnTi(PO_4)_3$**, **$Na_3MnPO_4CO_3$** ir **$Na_4Mn_3(PO_4)_2P_2O_7$** junginių degradacijos ir krūvio talpos mažėjimo vandeniniuose elektrolituose priežastis yra elektrochemiškai sukeltas $Mn^{(II)}$ tirpimas. Sukamo diskinio elektrodo su žiedu metodu *in-situ* atlikti tyrimai rodo, kad $Mn^{(III)}$ susidarymas įkrovimo metu yra lydimas stipraus Jahn-Teller efekto , kuris destabilizuoja junginių struktūrą ir skatina mangano tirpimą elektrocheminio ciklavimo metu. Šį Mn efektą šiek tiek slopina titano buvimas gardelėje, tačiau pilnai mangano tirpimo vandenyje stabiliu $Mn^{(II)}$ pavidalu nesustabdo. *Ex situ* kiekybinė analizė, atlita naudojant SEM/EDX metodus, rodo, kad didžioji dalis mangano lieka karkaso struktūroje, tačiau tampa elektrochemiškai neaktyvi arba nepasiekiama. Dėl šių priežasčių ištirti junginiai nėra perspektyvūs kaip teigiamų elektrodų medžiagos mažos koncentracijos vandeniniuose elektrolituose.

3. **$Na_3V_2(PO_4)_3$** pasižymi geru krūvio talpos išlaikymu labai koncentruotuose vandeniniuose elektrolituose, tačiau mažos

koncentracijos tirpaluose sparčiai degraduoja. Nustatyta, kad pagrindinė degradacijos priežastis yra vanadžio tirpimas. Didžiąja dalimi tai yra cheminis tirpimas, kadangi elektrodas tirpsta vien įmerkus jį į elektrolitą. Fluorido jonų įvedimas dalinai stabilizuoja struktūrą. **$Na_3V_2(PO_4)_2F_3$** yra žymiai atsparesnis cheminio tirpimo atžvilgiu, tačiau per 100 įkrovimo/iškrovimo ciklų praktiškai visas vanadis pereina į elektrolitą. Dviguba redokso titrimetrija ir *in-situ* eksperimentai, atlikti sukamo diskinio elektrodo su žiedu metodu, rodo, kad pagrindinis tirpimo produktas yra $V^{(V)}$. Elektrolito pH sumažinimas paskatina vanadžio tirpimą $V^{(IV)}$ formoje iškrovimo metu, kas dar pagreitina elekrodo degradaciją. Norint panaudoti **$Na_3V_2(PO_4)_2F_3$** kaip teigiamą elektrodą vandeninėse Na-jonų baterijose reikalingi stabilizuojantys elektrolito priedai arba apsauginės elektrodo dangos.

4. Konforminės polimerinės arba keraminės dangos gali sumažinti **$NaTi_2(PO_4)_3$** elektrodų degradaciją vandeniniuose elektrolituose. Elektrochemiškai nusodintas **PEDOT(PSS)** sluoksnis suteikia alternatyvų paviršių elektrocheminei deguonies redukcijos reakcijai, kurios metu sunaudojamas vietinis O_2, kuloninis našumas padidėja, tačiau pH vis tiek išauga. Kita vertus, rūgštūs polimerai, tokie kaip **Nafiona**s, užtikrina pakankamą mechaninę apsaugą ir lokalų buferiavimą. Tai žymiai padidina **$NaTi_2(PO_4)_3$** įkrovimo/iškrovimo kuloninį našumą bei krūvio talpos išlaikymą. Ištyrus keramines atominio sluoksniu nusodinimo metodu suformuotas **Al_2O_3**, **TiO_2** ir **HfO_2** dangas nustatyta, kad Al_2O_3 nėra pakankamai stabilus aukštesniame pH ir ilgainiui ištirpsta vandeniniuose elektrolituose įkrovimo/iškrovimo ciklavimo metu; TiO_2 pasižymi elektrocheminiu aktyvumu, dėl kurio padidėja lokalus pH ir pagreitėja **$NaTi_2(PO_4)_3$** degradacija. Tuo tarpu HfO_2 danga yra pakankamai elektrochemiškai inertiška ir chemiškai stabili, kad apsaugotų **$NaTi_2(PO_4)_3$** nuo degradacijos ilgesnio ciklavimo metu.

Acknowledgments

I am grateful for all the people who have directly or indirectly assisted with the completion of this study:

My supervisor Linas Vilčiauskas for providing an opportunity to conduct this research and offering much-needed assistance at every stage, from the design of experiments to interpreting results. Since picking me up from the airport almost five years ago, you have helped me with any problem I might have encountered here.

My academic consultant Jurga Juodkazytė for not only sharing her endless knowledge of the field but also patiently answering questions that I should have already known.

The rest of the research team: Jurgis Pilipavičius, Laurynas Staišiūnas Milda Petrulevičienė, Skirmantė Tutlienė, for their assistance throughout the years and for being great teammates.

Special thanks to Gintarė and Nadežda for being great groupmates and friends, despite being perpetually late for lunches. Without them, I might have also committed a tax fraud or two.

Aldona Balčiūnaitė, Aleksei Žarkov, Saulius Daugėla, Tomas Šalkus, Inga Morkvėnaitė-Vilkončienė, and Antanas Zinovičius for assisting with the experimental research for this work.

Aleksandra Prichodko, for patiently and promptly answering the endless questions regarding any formality that I might have found confusing.

And finally, my family and friends, who provided much-needed support despite the long distance.

List of publications covered in this thesis:

1. Plečkaitytė, G., Petrulevičienė, M., Staišiūnas, L., **Tediashvili, D**., Pilipavičius, J., Juodkazytė, J., Vilčiauskas, L. Understanding and mitigation of $NaTi_2(PO_4)_3$degradation in aqueous Na-ion batteries. *Journal of Materials Chemistry A, 9*(21), 12670–12683. (2021). DOI: https://doi.org/10.1039/D1TA01215K

2. **Tediashvili, D**., Geče, G., Pilipavičius, J., Daugela, S., Šalkus, T., Juodkazytė, J., Vilčiauskas, L. Synthesis, characterization, and degradation study of Mn-based phosphate frameworks ($Na_3MnTi(PO_4)_3$, $Na_3MnPO_4CO_3$, $Na_4Mn_3(PO_4)_2P_2O_7$) as aqueous Na-ion battery positive electrodes. *Electrochim Acta* **417**, (2022). DOI: https://doi.org/10.1016/j.electacta.2022.140294

3. **Tediashvili, D**., Pilipavičius, J., Juodkazytė, J., Vilčiauskas, L. On the degradation of vanadium-based phosphate framework electrode materials in aqueous environments. *Journal of Electrochemical Society* **170**, 120529 (2023). DOI: 10.1149/1945-7111/ad13fa

4. Staišiūnas, L., Pilipavičius, J., **Tediashvili, D**., Juodkazytė, J. & Vilčiauskas, L. Engineering of Conformal Electrode Coatings by Atomic Layer Deposition for Aqueous Na-ion Battery Electrodes. *Journal of Electrochemical Society* **170**, 050533 (2023). DOI: 10.1149/1945-7111/acd4ee

List of conference contributions:

1. **D. Tediashvili**, L. Vilčiauskas. Rotating ring-disc electrode study of Manganese and Vanadium based material operation and degradation as aqueous Na-ion battery cathodes. Chemistry and Chemical Technologies, September 24, 2021, Vilnius, Lithuania (Poster presentation).

2. **D. Tediashvili**, L. Vilčiauskas**.** Chemical and electrochemical stability of Vanadium-based cathodes for aqueous Na-ion batteries. Chemistry

and Chemical Technologies, March 10, 2023, Vilnius, Lithuania (Poster presentation)

3. **D. Tediashvili**, L. Vilčiauskas. Degradation study of Vanadium-based materials for aqueous Na-ion battery cathodes. Functional inorganic materials, October 6-8, 2022. Vilnius, Lithuania. (Oral presentation)

4. **D. Tediashvili**, L. Vilčiauskas. Rotating ring-disc electrode study of Mn-based material operation and degradation as aqueous Na-ion battery cathodes, 72nd annual International Society of Electrochemistry meeting, August 29 – September 3, 2021. JeJu, South Korea. (Poster presentation, Online)

5. **D. Tediashvili**, L. Vilčiauskas. Rotating ring-disc electrode study of vanadium-based materials for aqueous Na-ion batteries. 73rd annual International Society of Electrochemistry meeting. Xiamen, Fujian, China. (Poster presentation, Online)

6. **D. Tediashvili**, L. Vilčiauskas. A RRDE study of Mn-based cathode material degradation in aqueous Na-ion battery, Open Readings – 64th International Conference for students of physics and natural sciences, March 16-19, 2021, Vilnius, Lithuania. (Poster presentation)

7. **D. Tediashvili**, L. Vilčiauskas. Characterization of Mn-based phosphate frameworks as aqueous Na-ion battery cathodes. Open Readings – 65th International Conference for students of physics and natural sciences, March 15-18, 2022, Vilnius, Lithuania (Poster presentation)

8. **D. Tediashvili**, L. Vilčiauskas. Study of chemical and electrochemical degradation of Vanadium-based phosphate frameworks as aqueous Na-ion battery cathodes. Open Readings – 66th International Conference for students of physics and natural sciences, April 18-21, 2023, Vilnius, Lithuania (Poster presentation)

Curriculum Vitae

Name and surname	Davit Tedishvili
Date of birth	22.11.1995
Email	Davit.tediashvili@chgf.vu.lt

Education

2019-2024	PhD studies in Chemistry, Vilnius University, Vilnius, Lithuania
2017-2019	Master of Science (Specialization – Analytical Chemistry with a focus on Electrochemistry). Joint degree from Abo Akademi University (Turku, Finland) and University of Tartu (Tartu, Estonia)
2013-2017	Bachelor of Science, Chemistry, Agricultural University of Georgia, Tbilisi, Georgia
2001-2013	Public school, Tbilisi, Georgia

Working experience:

Feb. 2024 – May 2024	Senior Engineer, Center for Physical Science and Technology, Vilnius, Lithuania
Nov. 2019 – May 2023	Junior researcher. Center for Physical Science and Technology, Vilnius, Lithuania

Internships/trainings:

Jun. 2018 – Aug. 2018	Summer internship at physical measurement laboratory, Tartu Observatory, Tartu, Estonia
Jan. 2017 – Aug. 2017	Non-aqueous electrochemistry laboratory, Institute of Inorganic Chemistry and Electrochemistry (Tbilisi, Georgia),

References

1. Grey, C. P. & Tarascon, J. M. Sustainability and in situ monitoring in battery development. *Nature Materials* vol. 16 45–56 (2016).
2. Hedegaard, K. & Meibom, P. Wind power impacts and electricity storage - A time scale perspective. *Renew Energy* **37**, 318–324 (2012).
3. Lu, L., Yang, H. & Burnett, J. *Investigation on wind power potential on Hong Kong islands-an analysis of wind power and wind turbine characteristics*. *Renewable Energy* vol. 27 www.elsevier.com/locate/renene (2002).
4. Yang, Z. *et al.* Electrochemical energy storage for green grid. *Chem Rev* **111**, 3577–3613 (2011).
5. Pu, X. *et al.* Recent Progress in Rechargeable Sodium-Ion Batteries: toward High-Power Applications. *Small* vol. 15 (2019).
6. Tarascon, J. M. & Armand, M. Issues and challenges facing rechargeable lithium batteries. *Nature* (2001) doi:10.1038/35104644.
7. Maleki, H., Deng, G., Anani, A. & Howard, J. Thermal Stability Studies of Li-Ion Cells and Components. *J Electrochem Soc* **146**, 3224–3229 (1999).
8. Liu, J. Addressing the grand challenges in energy storage. *Advanced Functional Materials* vol. 23 924–928 (2013).
9. Orsini, F. *et al. In situ SEM study of the interfaces in plastic lithium cells*. *Journal of Power Sources* vol. 81 www.elsevier.comrlocaterjpowsour.
10. Berg, S. Battery failure analysis and characterization of failure types. *Process Safety Progress* **41**, 419–422 (2022).
11. Wen, J., Yu, Y. & Chen, C. A review on lithium-ion batteries safety issues: Existing problems and possible solutions. *Materials Express* vol. 2 197–212 (2012).
12. Pan, Q., Gong, D. & Tang, Y. Recent progress and perspective on electrolytes for sodium/potassium-based devices. *Energy Storage Materials* vol. 31 328–343 (2020).
13. You, Y., Sang, Z. & Liu, J. Recent developments on aqueous sodium-ion batteries. *Materials Technology* **31**, 501–509 (2016).
14. Wang, Y., Yi, J. & Xia, Y. Recent progress in aqueous lithium-ion batteries. *Advanced Energy Materials* vol. 2 830–840 (2012).
15. Liu, J., Bai, H., Guo, J., Su, C. & Liu, X. Electrochemical performance evaluations of spinel LiAl0.15Mn1.85O4 cathode materials prepared

by a solution combustion technique for lithium-ion batteries. *Int J Electrochem Sci* **13**, 6373–6387 (2018).

16. Wang, Y., Lou, J., Wu, W., Wang, C. & Xia, Y. Hybrid Aqueous Energy Storage Cells Using Activated Carbon and Lithium-Ion Intercalated Compounds. *J Electrochem Soc* **154**, A228 (2007).
17. Wu, E. J., Tepesch, P. D. & Ceder[2], G. *Size and charge ee ects on the structural stability of $LiMO_2$ (M = transition metal) compounds*. *Aydinol and Ceder* vol. 77 (1998).
18. Li, Z., Young, D., Xiang, K., Carter, W. C. & Chiang, Y. M. Towards high power high energy aqueous sodium-ion batteries: The $NaTi_2(PO_4)_3/Na_{0.44}MnO_2$ system. *Adv Energy Mater* **3**, 290–294 (2013).
19. Sauvage, F., Laffont, L., Tarascon, J. M. & Baudrin, E. Study of the insertion/deinsertion mechanism of sodium into $Na_{0.44}MnO_2$. *Inorg Chem* **46**, 3289–3294 (2007).
20. Goodenough, J. B., Hong, Y.-P. & Kafalas, J. A. FAST Na^+ - Ion Transport In Skeleton Structures. *Mater Res Bull* **11**, 203–220 (1976).
21. Anantharamulu, N. *et al.* A wide-ranging review on Nasicon type materials. *Journal of Materials Science* vol. 46 2821–2837 (2011).
22. Rajagopalan, R. *et al.* Understanding crystal structures, ion diffusion mechanisms and sodium storage behaviors of NASICON materials. *Energy Storage Materials* vol. 34 171–193 (2021).
23. Chen, S. *et al.* Challenges and Perspectives for NASICON-Type Electrode Materials for Advanced Sodium-Ion Batteries. *Advanced Materials* vol. 29 (2017).
24. Mohamed, A. I. & Whitacre, J. F. Capacity Fade of $NaTi_2(PO_4)_3$ in Aqueous Electrolyte Solutions: Relating pH Increases to Long Term Stability. *Electrochim Acta* (2017) doi:10.1016/j.electacta.2017.03.106.
25. Wu, W., Shabhag, S., Chang, J., Rutt, A. & Whitacre, J. F. Relating Electrolyte Concentration to Performance and Stability for $NaTi_2(PO_4)_3/Na_{0.44}$ MnO_2 Aqueous Sodium-Ion Batteries . *J Electrochem Soc* **162**, A803–A808 (2015).
26. Wolde-Rufael, Y. Energy demand and economic growth: The African experience. *J Policy Model* **27**, 891–903 (2005).
27. Winter, M. & Brodd, R. J. What are batteries, fuel cells, and supercapacitors? *Chem Rev* **104**, 4245–4269 (2004).
28. Lach, J., Wróbel, K., Wróbel, J., Podsadni, P. & Czerwiński, A. Applications of carbon in lead-acid batteries: a review. *Journal of Solid State Electrochemistry* vol. 23 693–705 (2019).

29. Chakkaravarthy, C., Periasamy, P., Jegannathan, S. & Vasu, K. I. *The nickel/Iron battery*. *Journal of Power Sources* vol. 35 (1991).
30. Chang, S., Young, K. H. & Lien, Y. L. Reviews of European patents on Nickel/Metal hydride batteries. *Batteries* vol. 3 (2017).
31. Dutta, A., Mitra, S., Basak, M. & Banerjee, T. A comprehensive review on batteries and supercapacitors: Development and challenges since their inception. *Energy Storage* vol. 5 (2023).
32. Linden, David. & Reddy, T. B. *Handbook of batteries*. (McGraw-Hill, 2002).
33. Treptow, R. S. The Lead-Acid Battery: Its Voltage in Theory and in Practice. *In the Classroom 334 Journal of Chemical Education* • vol. 79 https://pubs.acs.org/doi/10.1021/ed079p334 (2002).
34. Mizushima, K., Jones, P. C., Wiseman, P. J. & Goodenough, J. B. Li_xCoO_2 *(0<x~l):* A New Cathode Material For Batteries of High Energy Density. *Mat. Res. Bull* vol. 15 (1980).
35. Blomgren, G. E. The Development and Future of Lithium Ion Batteries. *J Electrochem Soc* **164**, A5019–A5025 (2017).
36. Wang, X., Yasukawa, E. & Mori, S. Inhibition of anodic corrosion of aluminum cathode current collector on recharging in lithium imide electrolytes. *Electrochim Acta* (2000) doi:10.1016/S0013-4686(99)00429-6.
37. Ls, E. & Er, E. Corrosion of aluminum at high voltages in non-aqueous electrolytes containing perfluoroalkylsulfonyl imides; new lithium salts for lithium-ion cells. *Journal of Power Sources* vol. 68 (1997).
38. Nitta, N., Wu, F., Lee, J. T. & Yushin, G. Li-ion battery materials: Present and future. *Materials Today* vol. 18 252–264 (2015).
39. Tarascon, J.-M. & Armand, M. Issues and challenges facing rechargeable lithium batteries. www.nature.com (2001).
40. Kim, H. *et al.* Aqueous rechargeable Li and Na ion batteries. *Chemical Reviews* vol. 114 11788–11827 (2014).
41. Doughty, D. H., Butler, P. C., Akhil, A. A., Clark, N. H. & Boyes, J. D. *Batteries for Large-Scale Stationary Electrical Energy Storage*.
42. Chen, S., Zhang, M., Zou, P., Sun, B. & Tao, S. Historical development and novel concepts on electrolytes for aqueous rechargeable batteries. *Energy and Environmental Science* (2022) doi:10.1039/d2ee00004k.
43. Roth, E. P. & Orendorff, J. C. How Electrolytes Influence Battery Safety. doi:DOI 10.1149/2.F04122if.

44. Zhang, H., Liu, X., Li, H., Hasa, I. & Passerini, S. Challenges and Strategies for High-Energy Aqueous Electrolyte Rechargeable Batteries. *Angewandte Chemie - International Edition* **60**, 598–616 (2021).
45. Alias, N. & Mohamad, A. A. Advances of aqueous rechargeable lithium-ion battery: A review. *Journal of Power Sources* vol. 274 237–251 (2015).
46. Liu, J., Xu, C., Chen, Z., Ni, S. & Shen, Z. X. Progress in aqueous rechargeable batteries. *Green Energy and Environment* **3**, 20–41 (2018).
47. Li, W., Dahn, J. R. & Wainwright, D. S. Rechargeable lithium batteries with aqueous electrolytes. *Science (1979)* (1994) doi:10.1126/science.264.5162.1115.
48. Vikström, H., Davidsson, S. & Höök, M. Lithium availability and future production outlooks. *Appl Energy* **110**, 252–266 (2013).
49. Ellis, B. L., Makahnouk, W. R. M., Makimura, Y., Toghill, K. & Nazar, L. F. A multifunctional 3.5V iron-based phosphate cathode for rechargeable batteries. *Nat Mater* **6**, 749–753 (2007).
50. El Kharbachi, A. *et al.* Exploits, advances and challenges benefiting beyond Li-ion battery technologies. *J Alloys Compd* **817**, (2020).
51. Larcher, D. & Tarascon, J. M. Towards greener and more sustainable batteries for electrical energy storage. *Nature Chemistry* vol. 7 19–29 (2015).
52. Palomares, V. *et al.* Na-ion batteries, recent advances and present challenges to become low cost energy storage systems. *Energy Environ Sci* **5**, 5884–5901 (2012).
53. Ferrara, C. *et al.* High-performance $Na_{0.44}MnO_2$ slabs for sodium-ion batteries obtained through urea-based solution combustion synthesis. *Batteries* **4**, (2018).
54. Barpanda, P., Lander, L., Nishimura, S. I. & Yamada, A. Polyanionic Insertion Materials for Sodium-Ion Batteries. *Adv Energy Mater* **8**, 1–26 (2018).
55. Li, J. & Ma, Z.-F. Past and Present of $LiFePO_4$: From Fundamental Research to Industrial Applications. *Chem* **5**, 3–6 (2019).
56. Padhi, A. K. & Goodenough, J. B. Phospho-olivines as Positive-Electrode Materials for Rechargeable Lithium Batteries. *J. Electroanal. Chem* vol. 144 (1997).
57. Padhi, A. K., Nanjundaswamy, K. S., Masquelier, C. & Goodenough, J. B. Mapping of Transition Metal Redox Energies in Phosphates with

NASICON Structure by Lithium Intercalation. *J Electrochem Soc* **144**, 2581–2586 (1997).

58. Padhi, A. K., Manivannan, V. & Goodenough, J. B. Tuning the Position of the Redox Couples in Materials with NASICON Structure by Anionic Substitution.

59. Chen, S. *et al.* Challenges and Perspectives for NASICON-Type Electrode Materials for Advanced Sodium-Ion Batteries. *Advanced Materials* vol. 29 (2017).

60. Wu, W., Mohamed, A. & Whitacre, J. F. Microwave Synthesized NaTi 2 (PO 4) 3 as an Aqueous Sodium-Ion Negative Electrode . *J Electrochem Soc* **160**, A497–A504 (2013).

61. Gopalakrishnan, J. & Kasthuri Rangan, K. Vanadium phosphate ($V_2(PO_4)_3$): a novel NASICON-type vanadium phosphate synthesized by oxidative deintercalation of sodium from sodium vanadium phosphate ($Na_3V_2(PO_4)_3$). *J. Solid State Chem* vol. 4 https://pubs.acs.org/doi/abs/10.1021/cm00022a001 (1992).

62. Song, W. *et al.* First exploration of Na-ion migration pathways in the NASICON structure $Na_3V_2(PO_4)_3$. *J Mater Chem A Mater* **2**, 5358–5362 (2014).

63. Mason, C. W. & Lange, F. Aqueous ion battery systems using sodium vanadium phosphate stabilized by titanium substitution. *ECS Electrochemistry Letters* **4**, A79–A82 (2015).

64. Shivashankaraiah, R. B., Manjunatha, H., Mahesh, K. C., Suresh, G. S. & Venkatesha, T. V. Electrochemical Characterization of $LiTi_2(PO_4)_3$ as Anode Material for Aqueous Rechargeable Lithium Batteries . *J Electrochem Soc* **159**, A1074–A1082 (2012).

65. Xu, T. *et al.* Nanostructured $LiTi_2(PO_4)_3$ anode with superior lithium and sodium storage capability aqueous electrolytes. *J Power Sources* **481**, (2021).

66. Gryaznov, D., Stauffer, S. K., Kotomin, E. A. & Vilčiauskas, L. Hybrid density functional theoretical study of NASICON-type $Na_xTi_2(PO_4)_3$ (x=1-4). *Physical Chemistry Chemical Physics* **22**, 11861–11870 (2020).

67. Gutierrez, A., Kim, S., Fister, T. T. & Johnson, C. S. Microwave-Assisted Synthesis of $NaCoPO_4$ Red-Phase and Initial Characterization as High Voltage Cathode for Sodium-Ion Batteries. *ACS Applied Materials and Interfaces* vol. 9 4391–4396 (2017).

68. Kim, H., Park, C. S., Choi, J. W. & Jung, Y. Defect-Controlled Formation of Triclinic $Na_2CoP_2O_7$ for 4 V Sodium-Ion Batteries . *Angewandte Chemie* **128**, 6774–6778 (2016).
69. Barpanda, P. *et al.* A layer-structured $Na_2CoP_2O_7$ pyrophosphate cathode for sodium-ion batteries. *RSC Adv* **3**, 3857–3860 (2013).
70. Ali, G. *et al.* Polythiophene-Wrapped Olivine $NaFePO_4$ as a Cathode for Na-Ion Batteries. *ACS Appl Mater Interfaces* **8**, 15422–15429 (2016).
71. Qiu, S. *et al.* NASICON-type $Na_3Fe_2(PO_4)_3$ as a low-cost and high-rate anode material for aqueous sodium-ion batteries. *Nano Energy* **64**, (2019).
72. Honma, T., Togashi, T., Ito, N. & Komatsu, T. Fabrication of $Na_2FeP_2O_7$ glass-ceramics for sodium ion battery.
73. Thackeray, M. M. *et al.* The quest for manganese-rich electrodes for lithium batteries: Strategic design and electrochemical behavior. *Sustain Energy Fuels* **2**, 1375–1397 (2018).
74. Wang, N. *et al.* A review of zinc-based battery from alkaline to acid. *Materials Today Advances* vol. 11 (2021).
75. Lu, Y., Wang, L., Cheng, J. & Goodenough, J. B. Prussian blue: A new framework of electrode materials for sodium batteries. *Chemical Communications* **48**, 6544–6546 (2012).
76. Pasta, M. *et al.* Full open-framework batteries for stationary energy storage. *Nat Commun* **5**, (2014).
77. Masquelier, C. & Croguennec, L. Polyanionic (phosphates, silicates, sulfates) frameworks as electrode materials for rechargeable Li (or Na) batteries. *Chemical Reviews* vol. 113 6552–6591 (2013).
78. Priyanka, V., Savithiri, G., Subadevi, R. & Sivakumar, M. An emerging electrochemically active maricite $NaMnPO_4$ as cathode material at elevated temperature for sodium-ion batteries. *Applied Nanoscience (Switzerland)* **10**, 3945–3951 (2020).
79. Gao, H., Li, Y., Park, K. & Goodenough, J. B. Sodium extraction from NASICON-structured $Na_3MnTi(PO_4)_3$ through $Mn^{(III)}/Mn^{(II)}$ and $Mn^{(IV)}/Mn^{(III)}$ redox couples. *Chemistry of Materials* **28**, 6553–6559 (2016).
80. Snarskis, G., Pilipavičius, J., Gryaznov, D., Mikoliū Naitė, L. & Vilčiauskas, L. Peculiarities of Phase Formation in Mn-Based Na SuperIonic Conductor (NaSICon) Systems: The Case of $Na_{1+2x}MnxTi_{2-x}(PO_4)_3$ ($0.0 \leq x \leq 1.5$). *Chemistry of Materials* **33**, 8394–8403 (2021).

81. Zarrabeitia, M. *et al.* Unraveling the role of Ti in the stability of positive layered oxide electrodes for rechargeable Na-ion batteries. *J Mater Chem A Mater* **7**, 14169–14179 (2019).
82. Song, W. *et al.* Aqueous Sodium-Ion Battery using a $Na_3V_2(PO_4)_3$ Electrode. *ChemElectroChem* **1**, (2014).
83. Jian, Z. *et al.* Superior electrochemical performance and storage mechanism of $Na_3V_2(PO_4)_3$ cathode for room-temperature sodium-ion batteries. *Adv Energy Mater* **3**, 156–160 (2013).
84. Zhu, L., Wang, H., Sun, D., Tang, Y. & Wang, H.-Y. A Comprehensive Review on the Fabrication, Modification and Applications of $Na_3V_2(PO_4)_2F_3$ Cathode. *J Mater Chem A Mater* (2020) doi:10.1039/d0ta07872g.
85. He, M. *et al.* High power NVPF/HC-based sodium-ion batteries. *J Power Sources* **588**, (2023).
86. Hadouchi, M. *et al.* Fast sodium intercalation in $Na_{3.41}FeV(PO_4)_3$: A novel sodium-deficient NASICON cathode for sodium-ion batteries. *Energy Storage Mater* **35**, 192–202 (2021).
87. Zhan, C., Wu, T., Lu, J. & Amine, K. Dissolution, migration, and deposition of transition metal ions in Li-ion batteries exemplified by Mn-based cathodes-A critical review. *Energy and Environmental Science* vol. 11 243–257 (2018).
88. Liu, T. *et al.* Correlation between manganese dissolution and dynamic phase stability in spinel-based lithium-ion battery. *Nat Commun* **10**, (2019).
89. Saulnier, M., Auclair, A., Liang, G. & Schougaard, S. B. Manganese dissolution in lithium-ion positive electrode materials. *Solid State Ion* **294**, 1–5 (2016).
90. Tesfamhret, Y., Liu, H., Chai, Z., Berg, E. & Younesi, R. On the Manganese Dissolution Process from LiMn2O4 Cathode Materials. *ChemElectroChem* **8**, 1516–1523 (2021).
91. Asl, H. Y. & Manthiram, A. Proton-Induced Disproportionation of Jahn − Teller-Active Transition-Metal Ions in Oxides Due to Electronically Driven Lattice Instability. (2020) doi:10.1021/jacs.0c10044.
92. Clarke, C. J., Browning, G. J. & Donne, S. W. An RDE and RRDE study into the electrodeposition of manganese dioxide. **51**, 5773–5784 (2006).

93. Allen, J. P. & Grey, C. P. Determining the oxidation states of dissolved transition metals in battery electrolytes from solution NMR spectra. *Chemical Communications* **59**, (2023).

94. Zech, C. *et al.* Quantitative manganese dissolution investigation in lithium-ion batteries by means of X-ray spectrometry techniques. *J Anal At Spectrom* **36**, (2021).

95. Hanf, L., Henschel, J., Diehl, M., Winter, M. & Nowak, S. Mn^{2+} or Mn^{3+}? Investigating transition metal dissolution of manganese species in lithium ion battery electrolytes by capillary electrophoresis. *Electrophoresis* **41**, 697–704 (2020).

96. Nikman, S., Zhao, D., Gonzalez-perez, V., Hoster, H. H. & Mertens, S. F. L. Electrochimica Acta Surface or bulk ? Real-time manganese dissolution detection in a lithium-ion cathode. *Electrochim Acta* **386**, 138373 (2021).

97. Wang, J., Islam, M. M. & Donne, S. W. In-situ detection of LiMn2O4 dissolution during electrochemical cycling by. *Electrochim Acta* **386**, (2021).

98. Bensalah, N. & De Luna, Y. Recent Progress in Layered Manganese and Vanadium Oxide Cathodes for Zn-Ion Batteries. *Energy Technology* vol. 9 (2021).

99. Zhang, D. *et al.* Two Birds with One Stone: Boosting Zinc-Ion Insertion/Extraction Kinetics and Suppressing Vanadium Dissolution of V_2O_5via La^{3+} Incorporation Enable Advanced Zinc-Ion Batteries. *ACS Appl Mater Interfaces* **13**, 38416–38424 (2021).

100. Wu, Y., Song, T. Y. & Chen, L. N. A review on recent developments of vanadium-based cathode for rechargeable zinc-ion batteries. *Tungsten* vol. 3 289–304 (2021).

101. Zhang, L. *et al.* Suppressing cathode dissolution via guest engineering for durable aqueous zinc-ion batteries. *J Mater Chem A Mater* **9**, 7631–7639 (2021).

102. Yue, J. *et al.* Interface Concentrated-Confinement Suppressing Cathode Dissolution in Water-in-Salt Electrolyte. *Adv Energy Mater* **10**, (2020).

103. Xing, Z. *et al.* Highly reversible zinc-ion battery enabled by suppressing vanadium dissolution through inorganic Zn^{2+} conductor electrolyte. *Nano Energy* **90**, (2021).

104. Zhang, L. *et al.* An In Situ Artificial Cathode Electrolyte Interphase Strategy for Suppressing Cathode Dissolution in Aqueous Zinc Ion Batteries. *Small Methods* **5**, (2021).

105. Zhang, H., Tan, X., Li, H., Passerini, S. & Huang, W. Assessment and progress of polyanionic cathodes in aqueous sodium batteries. *Energy and Environmental Science* vol. 14 (2021).
106. Yang, W. *et al.* Unravelling capacity fading mechanisms in sodium vanadyl phosphate for aqueous sodium-ion batteries. *J Colloid Interface Sci* **627**, (2022).
107. Xing, L. *et al.* Theoretical investigations on oxidative stability of solvents and oxidative decomposition mechanism of ethylene carbonate for lithium ion battery use. *Journal of Physical Chemistry B* **113**, (2009).
108. Martins, V. L. & Torresi, R. M. Water-in-salt electrolytes for high voltage aqueous electrochemical energy storage devices. *Curr Opin Electrochem* **21**, 62–68 (2020).
109. Jiang, L. *et al.* High-Voltage Aqueous Na-Ion Battery Enabled by Inert-Cation-Assisted Water-in-Salt Electrolyte. *Advanced Materials* **32**, 1–10 (2020).
110. Droguet, L., Grimaud, A., Fontaine, O. & Tarascon, J. M. Water-in-Salt Electrolyte (WiSE) for Aqueous Batteries: A Long Way to Practicality. *Adv Energy Mater* **10**, (2020).
111. Soundharrajan, V. *et al.* The dominant role of Mn^{2+} additive on the electrochemical reaction in $ZnMn_2O_4$ cathode for aqueous zinc-ion batteries. *Energy Storage Mater* **28**, 407–417 (2020).
112. Li, W., Li, S., Geng, T., Peng, F. & Liang, Y. Research Progress on Manganese Dissolution and Deposition Mechanism of Cathode Materials for Manganese-based Lithium Ion Batteries. *Kuei Suan Jen Hsueh Pao/Journal of the Chinese Ceramic Society* vol. 48 (2020).
113. Liu, Y., Qin, Z., Yang, X. & Sun, X. A Long-Life Manganese Oxide Cathode Material for Aqueous Zinc Batteries with a Negatively Charged Porous Host to Promote the Back-Deposition of Dissolved Mn2+. *Adv Funct Mater* **32**, (2022).
114. Wu, W., Yan, J., Wise, A., Rutt, A. & Whitacre, J. F. Using Intimate Carbon to Enhance the Performance of $NaTi_2(PO_4)_3$ Anode Materials: Carbon Nanotubes vs Graphite . *J Electrochem Soc* **161**, A561–A567 (2014).
115. Wu, F. *et al.* Multifunctional $ALPO_4$ coating for improving electrochemical properties of low-cost $Li[Li_{0.2}Fe_{0.1}Ni_{0.15}Mn_{0.55}]O_2$ cathode materials for lithium-ion batteries. *ACS Appl Mater Interfaces* **7**, 3773–3781 (2015).

116. Niemelä, J. P., Marin, G. & Karppinen, M. Titanium dioxide thin films by atomic layer deposition: A review. *Semiconductor Science and Technology* vol. 32 (2017).

117. Riyanto, E. *et al.* A review of atomic layer deposition for high lithium-ion battery performance. *Journal of Materials Research and Technology* vol. 15 5466–5481 (2021).

118. Hu, Y., Lu, J. & Feng, H. Surface modification and functionalization of powder materials by atomic layer deposition: a review. *RSC Advances* vol. 11 11918–11942 (2021).

119. Staišiūnas, L., Pilipavičius, J., Tediashvili, D., Juodkazytė, J. & Vilčiauskas, L. Engineering of Conformal Electrode Coatings by Atomic Layer Deposition for Aqueous Na-ion Battery Electrodes. *J Electrochem Soc* **170**, 050533 (2023).

120. Meng, X. Atomic-scale surface modifications and novel electrode designs for high-performance sodium-ion batteries via atomic layer deposition. *Journal of Materials Chemistry A* vol. 5 (2017).

121. Kvarnström, C. György Inzelt, Conducting polymers. A new era in electrochemistry. *Journal of Solid State Electrochemistry* **14**, (2010).

122. Murad, A. R., Iraqi, A., Aziz, S. B., Abdullah, S. N. & Brza, M. A. Conducting polymers for optoelectronic devices and organic solar cells: A review. *Polymers* vol. 12 (2020).

123. Pavel, I. A., Lakard, S. & Lakard, B. Flexible Sensors Based on Conductive Polymers. *Chemosensors* vol. 10 (2022).

124. Snook, G. A., Kao, P. & Best, A. S. Conducting-polymer-based supercapacitor devices and electrodes. *Journal of Power Sources* vol. 196 (2011).

125. Wang, Y., Ding, Y., Guo, X. & Yu, G. Conductive polymers for stretchable supercapacitors. *Nano Research* vol. 12 (2019).

126. Tran, V. Van, Lee, S., Lee, D. & Le, T. H. Recent Developments and Implementations of Conductive Polymer-Based Flexible Devices in Sensing Applications. *Polymers* vol. 14 (2022).

127. Lepage, D., Savignac, L., Saulnier, M., Gervais, S. & Schougaard, S. B. Modification of aluminum current collectors with a conductive polymer for application in lithium batteries. *Electrochem commun* **102**, 1–4 (2019).

128. Zeng, Y. *et al.* Achieving Ultrahigh Energy Density and Long Durability in a Flexible Rechargeable Quasi-Solid-State Zn–MnO_2 Battery. *Advanced Materials* **29**, 1–7 (2017).

129. Kamenskii, M. A., Volkov, F. S., Eliseeva, S. N., Holze, R. & Kondratiev, V. V. Comparative Study of PEDOT- and PEDOT:PSS Modified δ-MnO_2 Cathodes for Aqueous Zinc Batteries with Enhanced Properties. *J Electrochem Soc* **170**, 010505 (2023).
130. Lee, Y. *et al.* Unexpectedly high electrochemical performances of a monoclinic $Na_{2.4}V_2(PO_4)_3$/conductive polymer composite for Na-ion batteries. *J Mater Chem A Mater* **6**, 17571–17578 (2018).
131. Cao, C., Wang, H., Liu, W., Liao, X. & Li, L. Nafion membranes as electrolyte and separator for sodium-ion battery. *Int J Hydrogen Energy* **39**, 16110–16115 (2014).
132. Kulova, T. *et al.* Sodium rechargeable batteries with electrolytes based on nafion membranes intercalated by mixtures of organic solvents. *Batteries* **4**, (2018).
133. Bobacka, J., Ivaska, A. & Lewenstam, A. ChemInform Abstract: Potentiometric Ion Sensors. *ChemInform* **39**, (2008).
134. Bobacka, J. Potential stability of all-solid-state ion-selective electrodes using conducting polymers as ion-to-electron transducers. *Anal Chem* **71**, (1999).
135. Hu, L., Qi, W. & Li, Y. Coating strategies for atomic layer deposition. *Nanotechnology Reviews* vol. 6 (2017).
136. Murbach, M., Gerwe, B., Dawson-Elli, N. & Tsui, L. impedance.py: A Python package for electrochemical impedance analysis. *J Open Source Softw* **5**, 2349 (2020).
137. Serras, P. *et al.* Electrochemical Na extraction/insertion of $Na_3V_2O_{2x}(PO_4)_2F_{3-2x}$. *Chemistry of Materials* **25**, 4917–4925 (2013).
138. Plečkaitytė, G. *et al.* Understanding and mitigation of $NaTi_2(PO_4)_3$ degradation in aqueous Na-ion batteries. *J Mater Chem A Mater* **9**, 12670–12683 (2021).
139. Chirkov, Y. G. Gas-Generating Porous Electrodes at Low Overvoltages: Allowance for the Outside-Electrode Limitations. *Russian Journal of Electrochemistry* vol. 36 (2000).
140. Tseung, A. C. C. Gas evolution on porous electrodes*. *JOURNAL OF APPLIED ELECTROCHEMISTRY* vol. 15 (1985).
141. Pilipavičius, J., Traškina, N., Juodkazytė, J. & Vilčiauskas, L. The mechanism of $NaTi_2(PO_4)_3$ aqueous electrochemical degradation revisited. *Electrochim Acta* **465**, 142993 (2023).
142. Leslie, K., Harlow, J., Rathore, D., Tuul, K. & Metzger, M. Correlating Mn Dissolution and Capacity Fade in $LiMn_{0.8}Fe_{0.2}PO_4$/Graphite Cells During Cycling and Storage at

Elevated Temperature. *J Electrochem Soc* (2024) doi:10.1149/1945-7111/ad3b77.

143. Wang, L.-F., Ou, C.-C., Striebel, K. A. & Chen, J.-S. Study of Mn Dissolution from $LiMn_2O_4$ Spinel Electrodes Using Rotating Ring-Disk Collection Experiments. *J Electrochem Soc* **150**, A905 (2003).

144. Kaymaksiz, S., Wachtler, M. & Wohlfahrt-Mehrens, M. Influence of the solid electrolyte interphase on the performance of redox shuttle additives in Li-ion batteries - A rotating ring-disc electrode study. *J Power Sources* **273**, 123–127 (2015).

145. Tran, T. N. T., Jin, S., Cuisinier, M., Adams, B. D. & Ivey, D. G. Reaction mechanisms for electrolytic manganese dioxide in rechargeable aqueous zinc-ion batteries. *Sci Rep* **11**, (2021).

146. Tediashvili, D. *et al.* Synthesis, characterization, and degradation study of Mn-based phosphate frameworks ($Na_3MnTi(PO_4)_3$, $Na_3MnPO_4CO_3$, $Na_4Mn_3(PO_4)_2P_2O_7$) as aqueous Na-ion battery positive electrodes. *Electrochim Acta* **417**, (2022).

147. Qiu, C. *et al.* The function of Mn^{2+} additive in aqueous electrolyte for Zn/δ-MnO_2 battery. *Electrochim Acta* **351**, (2020).

148. Yang, D. *et al.* A Manganese Phosphate Cathode for Long-Life Aqueous Energy Storage. *Adv Funct Mater* **31**, (2021).

149. Jenkins, T., Alarco, J. A., Cowie, B. & Mackinnon, I. D. R. Direct spectroscopic observation of the reversible redox mechanism in $A_3V_2(PO_4)_3$(A=Li,Na) cathode materials for Li-ion batteries. *J Power Sources* **571**, (2023).

150. Yu, F. *et al.* Electrode Engineering by Atomic Layer Deposition for Sodium-Ion Batteries: From Traditional to Advanced Batteries. *Advanced Functional Materials* vol. 30 (2020).

151. Zhao, Y., Zheng, K. & Sun, X. Addressing Interfacial Issues in Liquid-Based and Solid-State Batteries by Atomic and Molecular Layer Deposition. *Joule* vol. 2 (2018).

152. Ma, L. *et al.* Atomic Layer Deposition for Lithium-Based Batteries. *Advanced Materials Interfaces* vol. 3 (2016).

153. Nayak, P. D., Ohayon, D., Wustoni, S. & Inal, S. Tailoring Electropolymerized Poly(3,4-ethylenedioxythiophene) Films for Oxygen Reduction Reaction. *Adv Mater Technol* **2100277**, 1–8 (2021).

NOTES

NOTES

NOTES

Vilnius University Press
9 Saulėtekio Ave., Building III, LT-10222 Vilnius
Email: info@leidykla.vu.lt, www.leidykla.vu.lt
bookshop.vu.lt, journals.vu.lt
Print run 20